

Controlled dosing of femto-litre volume liquids using hollow cantilevers

Cao Xi

Master of Science Thesis

Controlled dosing of femto-litre volume liquids using hollow cantilevers

MASTER OF SCIENCE THESIS

For the degree of Master of Science in Systems and Control at
Delft University of Technology

Cao Xi

November 17, 2016

Faculty of Mechanical, Maritime and Materials Engineering (3mE) ·
Delft University of Technology



Copyright © Delft Center for Systems and Control (DCSC)
All rights reserved.



Table of Contents

Acknowledgements	vii
1 Prior knowledge	1
1-1 Introduction	1
1-2 Atomic Force Microscope (AFM)	1
1-2-1 The Setup	2
1-2-2 Modes of operation	2
1-3 Introduction of AFM-based dispensing	4
1-4 Basic concepts and formulas	6
1-4-1 Surface tension and Laplace pressure	6
1-4-2 Navier–Stokes equation	7
1-4-3 Reynolds number	7
1-4-4 Hagen–Poiseuille law: Analogy to electrical circuits	8
1-4-5 Contact angle	8
1-5 Geometry of the liquid bridge	10
1-5-1 Circular Approximation	10
1-5-2 Young–Laplace equation	11
1-5-3 Energy minimization	12
1-6 Dispensing process of DPN	12
1-7 Conclusion	13
1-8 Goal of the thesis	13
1-9 Organization of the thesis	14

2	Modeling	15
2-1	Introduction	15
2-2	Dosing process	15
2-3	Modeling of the dosing process	16
2-3-1	First principle	16
2-3-2	The dynamic model	17
2-3-3	Young–Laplace equation	18
2-4	Volume and Contact angle Measurement	22
2-4-1	Volume Measurement	22
2-4-2	Contact angle measurement	23
2-5	Property of the dynamic model	24
2-5-1	Profile of the liquid bridge	24
2-5-2	Property of the parameter $c_1 \sqrt[3]{c_2}$	24
2-5-3	Capillary force validation	27
2-6	Conclusion	28
3	Experiments	29
3-1	Introduction	29
3-2	Experiments with nano-litre droplets	29
3-2-1	Experimental set up	29
3-2-2	Volume check	30
3-2-3	Precision tip suspending in the air	30
3-2-4	Precision tip touching the substrate	33
3-2-5	Clipped tip touching the substrate	35
3-2-6	Rupture ratio	37
3-3	Experiments with pico-femto-litre droplets (using hollow cantilevers)	41
3-3-1	Experimental set up	41
3-3-2	Volume Check	44
3-3-3	Dispensing on hydrophobic surface	45
3-3-4	Dispensing on hydrophilic surface	49
3-4	Conclusion	52
4	Controllers	53
4-1	Introduction	53
4-2	Pre-action before controlling	53
4-2-1	Humidity Control	53
4-2-2	System Identification	54
4-3	PID controller	55
4-4	Feedback Linearization and Iterative Learning Control	61
4-4-1	Feedback Linearization	61
4-4-2	Iterative Learning Control (ILC)	64
4-5	Model reference adaptive control (MRAC)	68
4-6	Conclusion	70

5 Conclusion and Future work	71
A The derivation of the formulas	73
A-1 Young–Laplace equation	73
A-2 Volume of the liquid bridge with tip touching the substrate	76
A-3 Volume of the liquid bridge from the break-up height	76
B Experimental data	77
B-1 Deflection graphs of dispensing on the hydrophobic surface	77
B-2 Captured frames of the dispensing process on the hydrophilic surface	81
Bibliography	85

Abstract

A hollow cantilever is used in place of a conventional cantilever to dispense and aspirate liquids in the femto-litre (10^{-15} L) volume range in an atomic force microscope (AFM) set up. Unlike a conventional AFM cantilever, these cantilevers are made hollow with an on-chip reservoir. Fluid is dispensed through a micro/nanometer scale aperture on the AFM tip. Dispensed (or aspirated) liquid volume is a function of tip contact time, applied pressure in the reservoir, surface energy of the substrate, surface energy of the tip, and surface tension of the liquid. In a conventional AFM, these parameters are usually not taken into consideration, but these factors will influence the dispense (aspirate) process of the hollow cantilever. To control the dispensing and aspiration process of a hollow cantilever, the influence of various factors needs to be analyzed and a dynamic model should be developed.

In the present thesis, initial experimental results on the dispensing process and an analytical dynamic model describing the process are reported. The model is based on the relation between the Laplace pressure and volume of the liquid bridge connecting the cantilever tip and the substrate. The model developed could describe the dispensing process with variance accounted for (VAF) larger than 90%. Based on the model, four different controllers are designed : series PID controller, parallel PI controller, combination of feedback linearization and iterative learning control and model reference controller. It was found the combination of feedback linearization and iterative learning control can control the system to dispense desired liquid much fast without any overshoot, and model reference controller can control the system without using system identification.

Acknowledgements

This master thesis is written as part of the requirement to obtain a Master degree in the department of DCSC at Delft University of Technology. As I have a strong interest in Physics, I tried to combine Physics and Controls in my project. After discussing with Dr. Murali Ghatkesar at the department of Precision and Microsystems Engineering (PME), I realized that there was a need for developing a physical model for the dosing process at femto-litre volumes and controlling the same. This kind of control system is new to the atomic force microscope. The combination of physics and control grabbed my attention and I choose to do this project. In this thesis, my efforts were three fold: developing a physical model for the dosing process, performing experiments to verify the developed model and designing an appropriate control system for the dosing process.

This thesis could not be carried out without the help of many people, therefore, in the first place, I would like to express my gratitude to my graduation committee: prof.dr.ir. J. Hellendoorn, the chair of the committee, Dr.Murali Ghatkesar, without his help, I could not have got this interesting project and carry out the experiments to verify my idea, and Dr.Simone Baldi & Hassan HosseinNia have provided me lot of guidance in designing the controllers. At the same time, the master thesis of Ir.Rick de Gruiter, the graduated master student in the Precision and Microsystems department, gave me a lot of inspiration.

Also, I would like to thank Bart Linssen, the master student in Eindhoven University of Technology, for his helpful suggestions during the project.

Delft, University of Technology
November 17, 2016

Cao Xi

Chapter 1

Prior knowledge

1-1 Introduction

Nanotechnology has been first introduced by Richard Feynman in 1959. In his lecture 'There is plenty of room at the bottom' he describes the possibility of direct manipulation and observation of individual atoms. In 1990s, the interest in nanotechnology greatly increased [1], and nowadays, a lot of branches of nanotechnology have arisen: handling liquids at nanoscale is one of them, with applications in microbiology and chemistry industries [2].

This thesis focuses on how to dose liquid on different substrates. The word, 'dosing' used in this thesis is referred to as delivering a predefined volume of liquid to a specific location. There are various ways to deliver liquid in different order of volume. For dosing liquid in the range from liters to milliliters, breaker glasses and syringes are usually used [2]. Micro pipette is used to dose liquid in the order of microliter. It works by applying mechanical pressure on a piston to create or eliminate vacuum to aspirate or dispense pre-determined volume of liquid [3]. At smaller scale in the range of femtolitre (10^{-18} m^3), syringe pumps with precision motor are used [4]. To dispense liquid from femtolitre to zeptolitre (10^{-24} m^3), electrospray techniques are used. The principle of this technique is to use electric field with high potential to generate charged droplet [5]. The disadvantage of this technique is that it is not able to aspirate liquid [4]. For controlled dosing liquid in the range from femtolitre to zeptolitre, atomic force microscope (AFM) based technique can be used [4]. An example of the AFM based device is hollow cantilever. The goal of the thesis is to control the dosing process of hollow cantilever. In this chapter, the necessary concepts to design the controller are introduced.

1-2 Atomic Force Microscope (AFM)

To understand what is hollow cantilever and its principle, it is necessary to have basic knowledge about AFM. Because hollow cantilever is developed from AFM. So in this section the composition of AFM and its two working modes are introduced.

1-2-1 The Setup

The schematic of AMF is shown in Figure 1-1. There are two main parts of an AFM, piezoelectric transducer and force transducer.

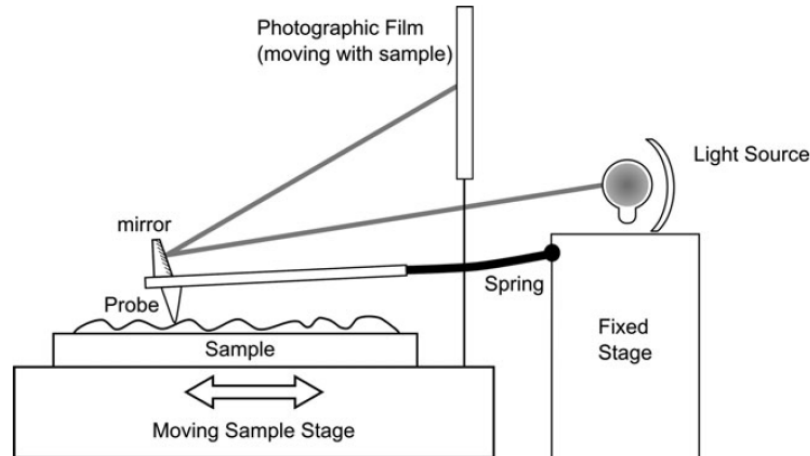


Figure 1-1: Schematic of AFM setup [6].

The piezoelectric transducer uses piezoelectric material, which convert electric potential into mechanical motion. Because a single piezoelectric device have the ability to move in the order of 0.2 nm per applied volt, it is used to control movement of AFM [6].

The force transducer is used to measure the force between an AFM surface and a substrate. Typically, the force transducer in an AFM is a cantilever with integrated tip, and an optical lever [6].

The combination of the piezoelectric transducer and force transducer is shown in Figure 1-2. It uses piezoelectric material to make vertical small distance movement, and use laser and photodetector to measure the displacement of the cantilever, which can show the force between the probe and surface.

1-2-2 Modes of operation

The basis of AFM as a microscopic technique is that it measures the topography of the sample. The datasets generated by AFM are not conventional images, as produced by optical microscopy, but rather a map of height measurements. In order to make these height measurements, a variety of modes have developed, which can be divided into those modes which measure the static deflection of the AFM cantilever (contact mode) [6], and those that measure the dynamic oscillation of the cantilever (dynamic mode) [7].

Contact mode

Contact mode is the first mode developed for AFM. In order to understand the way AFM works, it is necessary to use so-called force-distance curves. A cartoon of a simple force

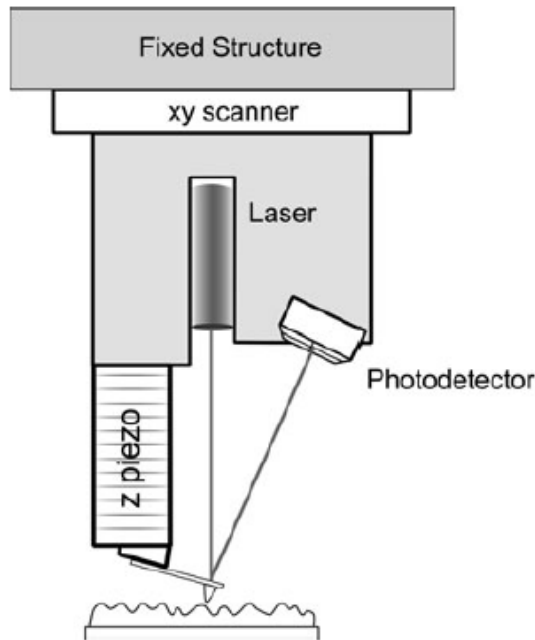


Figure 1-2: Tip-scanning AFM with optical lever sensors [6].

distance curve is shown in Figure 1-3. When the tip is far from the sample surface, the cantilever is considered to have zero deflection; as the tip approach the surface, it normally feels first an attractive force which is combined by van der Waals force, electrostatic force and chemical force. As the instrument continues to push the cantilever towards the surface, the interaction moves into the 'repulsive' regime, i.e. the tip is now applying a force to the sample, and the sample applies an opposite force to tip, which is caused by Coulombic interaction. In this regime, a combination of cantilever bending and sample compression will be occurring according to the relative compliances of the sample surface and AFM probe. If the direction of movement is reversed, the interaction passes again into the attractive regime, and the tip stays on the surface until instability occurs once more, and the tip snaps off the surface. It is within the repulsive regime that contact-mode imaging usually occurs. In other words, in contact-mode AFM, the tip of the probe is always touching the sample [6].

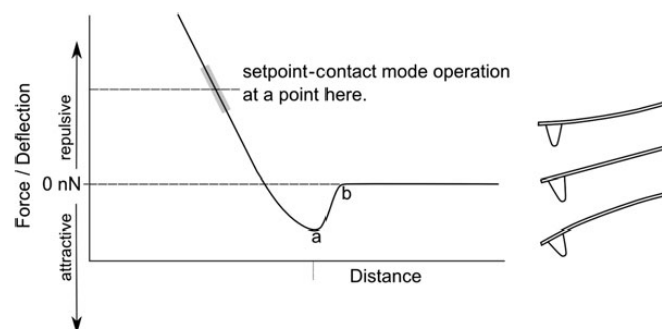


Figure 1-3: Illustration of AFM stage [6].

Dynamic Mode

The cantilever of AFM can be excited to vibrate at its resonant frequency. Under the influence of tip-sample forces the resonant frequency of the cantilever will change and serve as measurement parameters. This is called dynamic mode of AFM. The difference between static mode and dynamic mode is the static deflection AFM directly gives the interaction force between tip and sample, as for the dynamic mode, it is found that the resonant frequency, amplitude, and phase of the oscillation change as consequence of the interaction forces [7].

1-3 Introduction of AFM-based dispensing

The AFM has been mentioned above, it uses sharp tip, cantilever and sensors to investigate the features of surface. AFM is not only used for high precision imaging, it also has the ability to dispense and aspirate liquid.

The evolution of various AFM based fluid manipulation systems are classified in Figure 1-4. It started by simple dipping and writing technique called Dip Pen Nanolithography (DPN) technique using commercially available AFM probes. To increase the reproducibility and on-chip liquid storage capability. Nanoscale Dispensing (NADIS), Nanofountain Probe (NFprobe) and Scanning Ion Pipette (SIP) devices were developed.

Dip Pen Nanolithography (DPN)

Deposition of organic molecules by the tip of the scanning probe microscope was first reported in 1995 [8]. It works in the way like writing with a quill. Every time it is dipped, the tip is covered a layer of liquid. When the tip touches the substrate, the molecules start to diffuse from this point-contact to the surface through a water liquid bridge, forming a small spot of monolayer of molecules [9]. The drawback of DPN is obvious, when ink on the DPN surface is exhausted, it needs to re-inked to continue its progress. Furthermore it does not have the capability to aspirate.

Nanoscale Dispensing (NADIS)

For the NADIS, a hollow tip is fabricated as the reservoir of liquid. An aperture (outlet hole) at the tip apex is milled for dispensing. A droplet is placed inside the hollow tip. Once the tip touched the sample surface, a liquid bridge is shaped around the outlet hole. And liquid in the reservoir is transformed from the reservoir to the substrate through the aperture at the tip of apex [10]. There is a reservoir in the NADIS, so it can extend the writing times compared to DPN technique. And similar to DPN, the major limitation of this method is the lack of aspiration capability.

Nano Fountain Probe (NFProbe)

A large reservoir via a hollow cantilever to an outlet hole in the tip is used in this method. In order to maintain the high-resolution writing capabilities, the sharp tip is kept as a point-

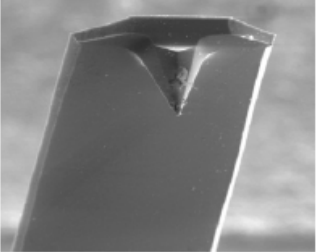
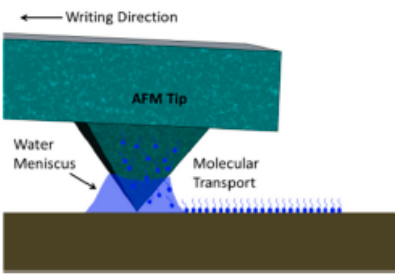
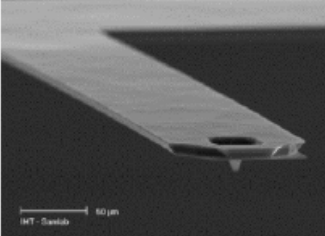
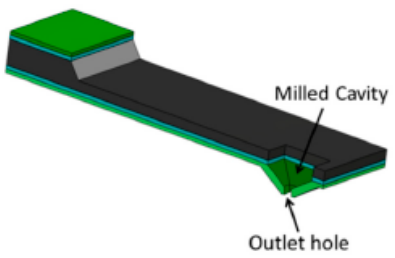
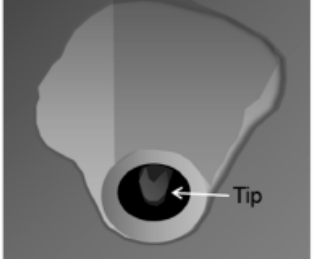
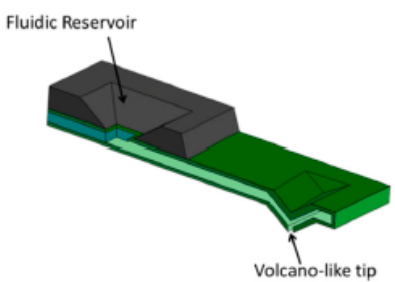
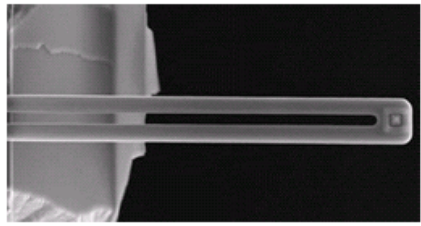
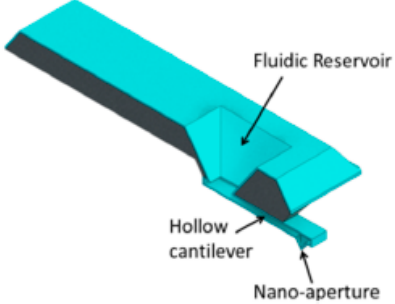
AFM Based Dispensing	Schematic	Working Principle
<p>(a) Dip Pen Nanolithography (DPN)</p> 	 <p>← Writing Direction</p> <p>AFM Tip</p> <p>Water Meniscus</p> <p>Molecular Transport</p>	<p>AFM tip is dip-coated with the ink which is then transferred via water meniscus formed between tip and substrate.</p>
<p>(b) Nanoscale Dispensing (NADIS)</p> 	 <p>Milled Cavity</p> <p>Outlet hole</p>	<p>An aperture outlet hole is milled into the hollow tip apex. The ink is placed as a large droplet into the hollow tip which serves as reservoir.</p>
<p>(c) Nanofountain Probe (NFProbe)</p>  <p>Tip</p>	 <p>Fluidic Reservoir</p> <p>Volcano-like tip</p>	<p>A continuous supply of ink to the tip is achieved by on-chip reservoir and a capillary connection between them. Liquid is dispensed through a volcano-like tip.</p>
<p>(d) Scanning Ion Pipette (SIP)</p> 	 <p>Fluidic Reservoir</p> <p>Hollow cantilever</p> <p>Nano-aperture</p>	<p>On-chip reservoir connected to the tip through a hollow cantilever; continuous supply of ink. Liquid is dispensed through an aperture near the hollow tip.</p>

Figure 1-4: Different types of AFM based nanoscale fluid handling Probes [4].

contact and is surrounded by the on-chip reservoir so the shape of tip is volcano. Liquid is transformed to the substrate through the tip via a water bridge [11].

Scanning Ion Pipette (SIP) (hollow cantilever)

The scanning Ion Pipette (SIP) is also called hollow cantilever. The same as NFProbe, hollow cantilever can continuously printing. Compared to NFProbe, the pyramid tip is made of silicon nitride, which can ensure the hardness and hence the tip shape after multiple dispensing cycles [4].

1-4 Basic concepts and formulas

1-4-1 Surface tension and Laplace pressure

When a liquid molecule wanders from the bulk to the surface of liquid, it will lose half of its cohesive interaction. Change surface area of liquid will change the energy. Surface tension can describe the change of energy. If liquid is distorted by increasing surface area by an amount dA , the work done can be written as:

$$\delta W = \gamma dA \quad (1-1)$$

where γ (N/m) is the surface tension. From the above formula, the surface tension is defined as: the energy must be supplied to increase the surface area by one unit [12].

The general formula connecting geometry information and pressure inside liquid is the Laplace theorem [12]. It is defined as: The increase in hydrostatic pressure Δp (Pa) that occurs upon traversing the boundary between two fluids is equal to the product of the surface tension γ and the curvature of the surface $H = \frac{1}{R} + \frac{1}{R'}$ (1/m):

$$\Delta p = \gamma \left(\frac{1}{R} + \frac{1}{R'} \right) \quad (1-2)$$

where Δp is the pressure difference between the outside of liquid and the inside of liquid. R (m) and R' are the radius of curvature of the surface [12]. $\frac{1}{R}$ and $\frac{1}{R'}$ are called the principle curvatures. The radius of the curvature of a surface can be explained by an example of a pear in Figure 1-5. The curvature at a point M is determined by inserting an arrow defining the direction \vec{N} normal to the surface. Then the pear is cut along two mutually orthogonal planes intersecting each other along \vec{N} . The intersection of these planes with the surface of the pear defines two curves, the radius of curvature of the point M is R and R' .

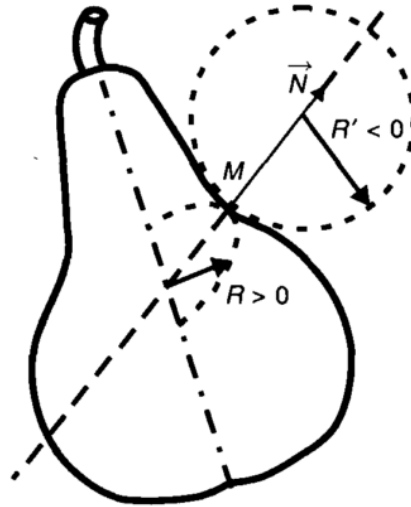


Figure 1-5: Measuring the curvature of a pear at a particular point [12].

1-4-2 Navier–Stokes equation

The Navier-Stokes equation is used to describe motion of viscous fluid. Because flows in microfluidic devices, fluids can be approximated as incompressible [13]. Assume the fluid is laminar. The incompressible Navier–Stokes equation for uniform-viscous Newtonian fluids with no body forces can be written as [14]:

$$\rho \frac{\partial \vec{u}}{\partial t} = -\rho \vec{u} \nabla \vec{u} - \nabla p + \mu \nabla^2 \vec{u} \quad (1-3)$$

(Rate of change of momentum) = (convective force) + (pressure force) + (viscous force)

where \vec{u} is the velocity field (m/s), which is a description of the velocity of the fluid at a given point in space and time, and is denoted by $\vec{u} = \vec{u}(\vec{r}, t)$, where \vec{r} is a position vector specifying a location in space (m) and t is time (s); ρ is the fluid density (kg/m^3); μ is the viscosity ($\text{Pa} \cdot \text{s}$); and p is pressure (Pa). It should be noted that the viscosity is a function of temperature; fluid becomes less viscous as temperature increases.

1-4-3 Reynolds number

To characterize the fluidic behavior in channels as laminar or turbulent flow, the Reynolds number is conventionally defined as the ratio of inertial forces to viscous forces. It is well known that laminar flow occurs at low Reynolds numbers ($\text{Re} < 2300$ for the straight and smooth channels), where viscous forces are dominant. To describe the Reynolds number, we need a characteristic velocity V (m/s) (or the area-averaged velocity U (m/s) and a characteristic length D (m) (or a hydraulic diameter D_H of the channel (m)). The hydraulic diameter is a computed value that depends on the channel's cross-sectional geometry. The Reynolds number is:

$$\text{Re} = \frac{(\text{inertia force})}{(\text{viscous force})} = \frac{\rho V D}{\mu} \approx \frac{\rho U D_H}{\mu} \quad (1-4)$$

Fluid flows in micro-channels are almost always at low Reynolds number ($Re < 1$) due to small hydraulic diameters and relative slow volume flow rate [15].

1-4-4 Hagen–Poiseuille law: Analogy to electrical circuits

In the steady-state of fully developed fluid flow in the channel, its velocity field is unidirectional and laminar and there is no acceleration of fluid. Thus the unsteady and convection terms of Navier–Stokes equation all becomes zero, and it becomes [14]:

$$\nabla p = \mu \nabla^2 \vec{u} \quad (1-5)$$

Make the geometry simple, assume flow is in a circular channel and has a parabolic velocity profile like in Figure 1-6. The Hagen–Poiseuille’s law gives [14]:

$$Q = \frac{\pi R^4}{8\mu} \left(-\frac{dp}{dx}\right) \quad (1-6)$$

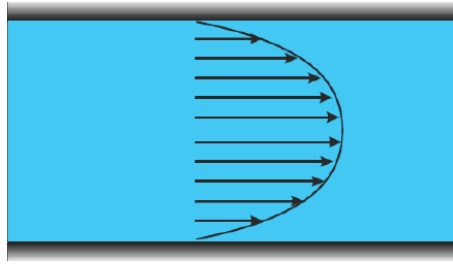


Figure 1-6: Flow in a circular channel and has a parabolic velocity profile [14].

where Q is the volumetric flow rate (m^3/s), R is the radius of the circular channel (m), μ is the viscosity ($\text{Pa} \cdot \text{s}$), $\frac{dp}{dx}$ (Pa/m) is the pressure change in small distance dx . Equation (1-6) gives the flow-pressure relation in pressure-driven channels, and Hagen-Poiseuille’s law can be simplified as [14]:

$$Q = \frac{\Delta p}{R_H} \quad (1-7)$$

where the hydraulic resistance R_H ($\text{Pa} \cdot \text{s}^3/\text{m}$) is defined as [14]:

$$R_H = \frac{8\mu L}{\pi R^4} \quad (1-8)$$

where L is the length of the channel (m).

1-4-5 Contact angle

When liquid droplet lies on solid surface, for different property of the liquid and surface, the shape of droplet will change. The angle between the tangent line of one side of droplet and surface is called the contact angle, which is illustrated in Figure 1-7.

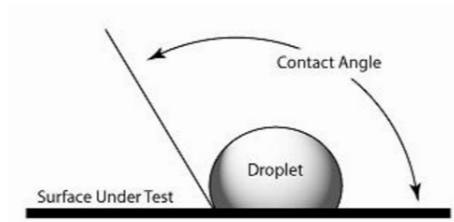


Figure 1-7: Illustration of contact angle [12] .

And the contact angle is determined by the surface tension of the solid air interface γ_{SO} and solid liquid interface γ_{SL} , which is shown in Figure 1-8. The relation is:

$$\gamma \cos \theta_E = \gamma_{SO} - \gamma_{SL} \quad (1-9)$$

where θ_E is the contact angle.

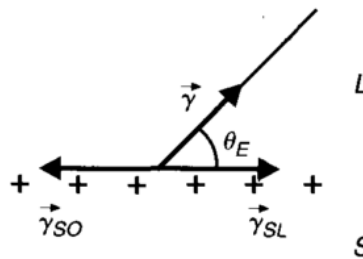


Figure 1-8: Determine of contact angle [12] .

When the contact angle between the droplet and surface is less 90° , the surface is called hydrophilic, otherwise, the surface is hydrophobic [12], which is shown in Figure 1-9. When

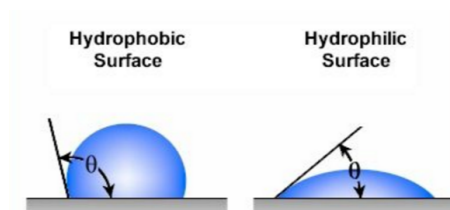


Figure 1-9: Illustration of the hydrophobic surface and hydrophilic surface.

the droplet changes shape by outside force, the contact angle will become complex. The process how the contact angle changes when volume of droplet changes in dynamic situation is shown in Figure 1-10. In the experiment, a hollow needle is used to deposit a small drop on the surface while leaving the needle inside the drop (Figure 1-10(a)). More liquid is slowly pumped into the drop, which makes the drop grow. Firstly, the contact angle increases (Figure 1-10(b)) until it saturates to a certain value (Figure 1-10(c)). At the moment the contact line starts to advance, this angle is the largest possible contact angle called advancing contact angle (ACA). To get the smallest contact angle that is called receding contact angle (RCA),

the opposite should be done, slowly pump liquid out from the sessile drop (Figure 1-10(d,e)). The difference between the ACA and RCA is called contact angle hysteresis [16].

In [16], there is also discussion about when the ACA and RCA happen. The conclusion is that the smaller the initial volume of liquid, the quicker the ACA and RCA happen.

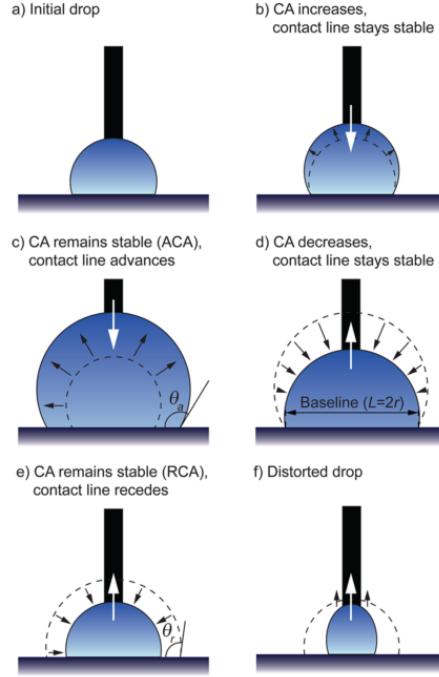


Figure 1-10: (a) Small drop is deposited on a surface. (b) Liquid is pumped into the drop and volume increases while the contact line is not advancing. (c) ACA is reached and the contact line starts to advance. The volume is still increased. (d) Liquid is pumped out of the drop and volume decreases, while the baseline does not recede. The CA decreases, because the RCA has not been reached. (e) The RCA is reached and the drop baseline recedes. The CA does not change during this phase. (f) The drop size reaches the same magnitude as the size of the needle and/or the size of the roughness features on the surface. The drop shape is strongly distorted and often the CA decreases or increases rapidly [16].

1-5 Geometry of the liquid bridge

1-5-1 Circular Approximation

The geometry of the liquid bridge can be treated as part of a circle which is shown in Figure 1-11 [17]. In the figure, b is the radius of tip where the liquid bridge has reached, α is half angle of the pyramid tip and D is the distance between tip and substrate. R and R' are the two different radius of curvature for the liquid bridge, which can be expressed as:

$$R' = \frac{\frac{b}{\tan \alpha} + D}{\sin(\alpha - \theta_1) + \cos \theta_2}, R = b - r(1 - \cos(\alpha - \theta_1)) \quad (1-10)$$

Based on Figure 1-11, the liquid bridge volume V_1 can be obtained by rotating the circular arc with radius R' around the z axis and subtracting the part of the pyramid tip immersed in the liquid bridge:

$$V_1 = \pi \left\{ z_1(R + R')^2 + z_1 R'^2 - \frac{z_1^3}{3} + z_1^2 R' \cos \theta_2 - z_1 R'^2 \cos^2 \theta_2 - 2(R + R')R'^2 \left(\frac{1}{2} \left(\frac{z_1}{R'} - \cos \theta_2 \right) \sqrt{1 - \left(\frac{z_1}{R'} - \cos \theta_2 \right)^2} + \frac{1}{2} \cos \theta_2 \sqrt{1 - \cos^2 \theta_2} + \frac{1}{2} \sin^{-1} \left(\frac{z_1}{R'} - \cos \theta_2 \right) - \sin^{-1}(-\cos \theta_2) \right) \right\} - \frac{b^3}{3 \tan \alpha} \quad (1-11)$$

where θ_1 and θ_2 are the two contact angles, which are shown in Figure 1-11. z_1 is the coordinate of the point 1 in z direction:

$$z_1 = \frac{b}{\tan \alpha} + D$$

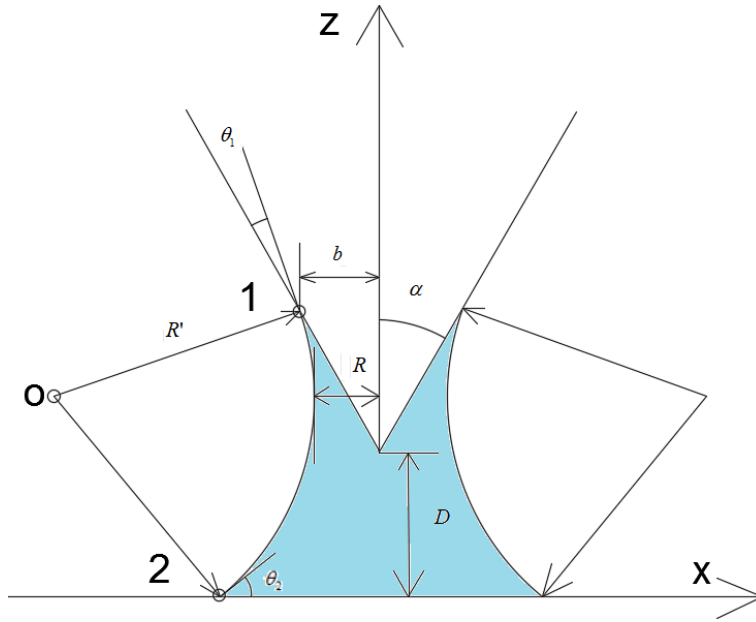


Figure 1-11: Schematic geometry of a capillary interaction between a pyramid tip and the plane when use circular approximation.

1-5-2 Young–Laplace equation

There is difference between the real liquid bridge and the one using the circular approximation [18]. It will increase the accuracy of the geometry of the liquid bridge by solving the Laplace–Young equation in terms of elliptic integrals [19][20]. If the liquid bridge is axisymmetric, its mean curvature (the mean of two principle curvatures) then satisfies the following Young–Laplace equation:

$$2H_{mean} = \frac{d^2 z / dr^2}{[1 + (dz/dr)^2]^{3/2}} + \frac{dz/dr}{r[1 + (dz/dr)^2]^{1/2}} \quad (1-12)$$

where H_{mean} is the mean curvature, z and r are the vertical coordinate and horizontal coordinate which is shown in Figure 1-12.

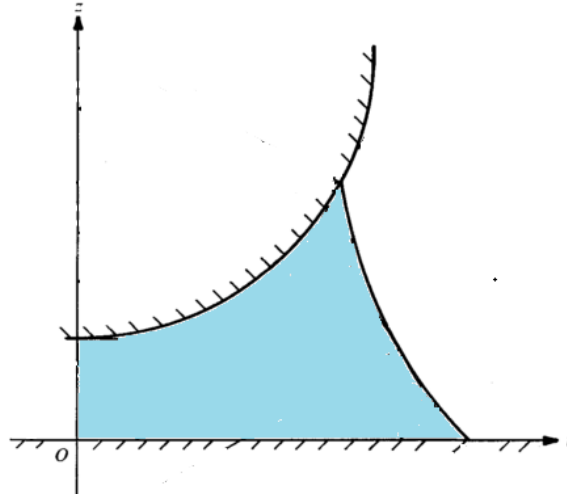


Figure 1-12: The liquid bridge between a sphere and substrate.

1-5-3 Energy minimization

There is a software named "surface evolver" to determine liquid shape by energy minimization [21]. When consider the liquid bridge between a conical tip and a flat substrate. First, an initial shape of the system, including the liquid bridge connecting the tip and the surface, is created by fixing its vertex coordinates. The mesh is then sequentially refined and the vertex coordinates optimize (using a gradient method) until an equilibrium shape made of approximately 30 000 facets is reached, which is shown in Figure 1-13.



Figure 1-13: Shape of the Liquid bridge between a conical tip and a surface: the left one is before optimization and the right is after optimization using "surface evolver" [21].

1-6 Dispensing process of DPN

There is not any existing model describing the dispensing process of hollow cantilever but there is one describing the process of DPN [22]. When do experiment by using DPN to dispense liquid in two different situations, first is just after inking the pen and the other is much of the ink on the pen has been expanded. The result is that the volume of the first

experiment is much larger than the second one. The reason is explained as the change of Laplace pressure ΔP which is shown in Figure 1-14. Because of the volume of the liquid at the base of the tip decreases, the Laplace pressure in it also decreases. Note the Laplace pressure is negative. When assume the geometry of the liquid bridge does not change, so the pressure difference between the liquid at the base and the liquid bridge decrease, then the dispensing rate will decrease.

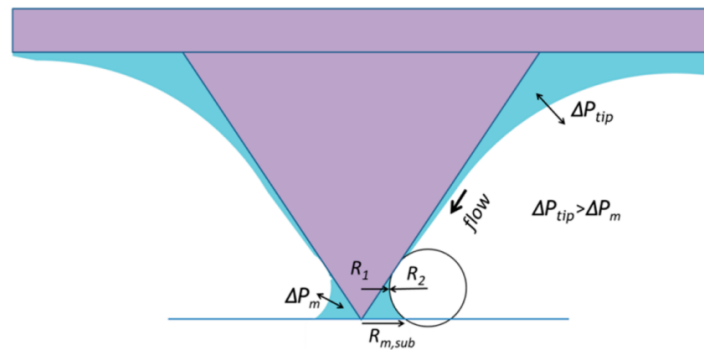


Figure 1-14: The model of dispensing process of DPN [22].

1-7 Conclusion

The goal of the thesis is to design a controller for the dosing process. To design the controller, the dynamic model of the dosing process of hollow cantilever is needed to develop. From the analysis of the dispensing process of DPN, it is known that the Laplace pressure of the liquid bridge will influence its dispensing process. Because the dosing process of hollow cantilever is similar with the dispensing process of DPN, the model is based on the influence of Laplace pressure. To get the Laplace pressure of the liquid bridge, the curvature is needed. There are three different methods to obtain the curvature of the liquid bridge in this chapter: circular approximation, Young–Laplace equation and energy minimization. By comparing these three methods, Young–Laplace method has the benefit of giving the equation to calculate the precise curvature. How to use the Young–Laplace equation to find the relation between the Laplace pressure of the liquid bridge and its volume is the most important problem to be solved to make the model. The detail is introduced in the next chapter.

1-8 Goal of the thesis

The goal of the thesis is two fold:

- Develop and validate a dynamic model that describes the dosing process.
- Design a controller for precise dispensing and aspiration of liquids based on the developed model.

1-9 Organization of the thesis

In this thesis, the dosing process and control method of the hollow cantilever will be introduced in detail. The hollow cantilever is based on AFM. In this chapter, there is an introduction about AFM. At the same time, the necessary principles to model the process are introduced.

In the chapter 2, details about how to make the model are explained. And experiments are designed to valid the model in Chapter 3. It is demonstrated that the model can describe the dosing process with variance accounted for (VAF) larger than 90%.

In the chapter 4, four different controllers are designed, and simulation results are shown. The combination of feedback linearization and iterative learning control can control the process without overshoot in high speed.

In the chapter 5, there is a final conclusion and discussion about the future work to do to verify the model and control the process.

Chapter 2

Modeling

2-1 Introduction

In order to design a controller for the accurate dosing process of the AFM based hollow cantilever, a dynamic model describing the dosing process is necessary. The dynamic model of the dosing process based on pressure is introduced in this chapter, which properly combines Laplace pressure and circuit analogy method.

The rest of the chapter is organized as follows. Section 2-2 explains the dosing process. In the section 2-3, the dynamic model of the dosing process is introduced. In the section 2-4 experimental methods to measure volume and contact angle are explained, which is used to measure volume in real-time. Section 2-4 discusses the property of the dynamic model and validates the model by using capillary force.

2-2 Dosing process

The dosing process is shown in Figure 2-1. In step 1, the hollow cantilever approaches the substrate with the same step size, the *step size* means the distance the hollow cantilever AFM tip moves vertically at a specific time period. In step 2, the tip connects the substrate, and the outside pressure control system provides pressure for a certain period. The period is called contact time. And the liquid connecting tip and substrate is called *liquid bridge*. In the step 3, the tip starts to retract from the substrate at the same step size. After the liquid bridge breaks up, the liquid droplet remains on the substrate in step 4. β (rad) in step 4 is called *contact angle*, which is measured through the liquid, where a liquid-vapor interface meets a solid surface. In the step 2, when provide positive pressure, the three phase boundary of liquid bridge increases, θ_d (rad) is called *advancing contact angle*. When provide negative pressure, the three phase boundary of the liquid bridge decreases, θ_d is called *receding contact angle*. Advancing contact angle and receding contact angle are called dynamic contact angle. The distance between the tip of hollow cantilever and substrate at the instance the liquid bridge

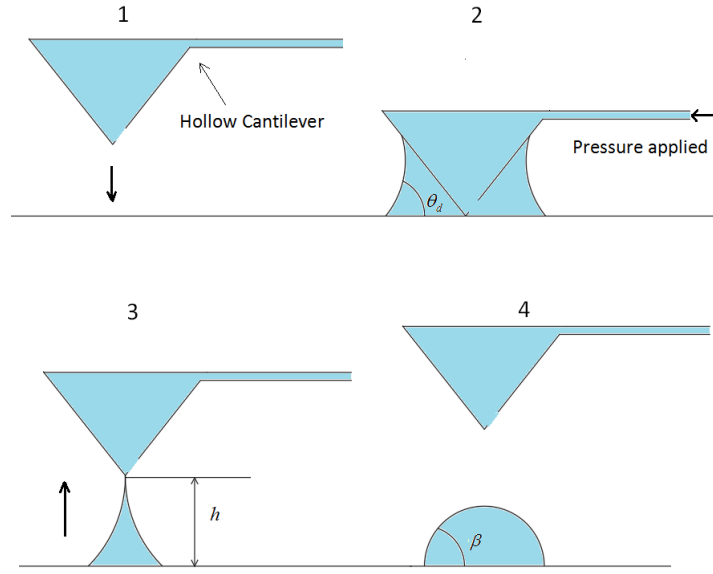


Figure 2-1: Schematic of one dosing process.

breaks h (m) in step 3 is called *break-up height*. The break-up height can be obtained by AFM deflection graph shown in Figure 2-2. The blue line shows the bending of the cantilever when AFM-FP tip approaches the substrate, and red line shows the AFM-FP tip retracting from the substrate. It is seen there is a large difference between the two lines because when the tip retracts there is a liquid bridge connects the AFM-tip and the substrate. Liquid bridge breaking occurs when the red line suddenly coincide with the blue line. The break-up height is calculated by using the break-up position subtracted by the snap in position.

2-3 Modeling of the dosing process

2-3-1 First principle

For uniform-viscous and incompressible Newtonian fluids with no body forces, the flow rate in a channel can be derived according to the electrical circuit analogy method [14]:

$$Q = \frac{\Delta P}{R_H} \quad (2-1)$$

where Q (m^3/s) is the volumetric flow rate, ΔP (Pa) is the pressure difference, R_H ($\text{Pa} \cdot \text{s}/\text{m}^3$) is the hydraulic resistance. In microfluidic networks, the shape of channel is usually rectangular [14]. The hydraulic resistance of a rectangular channel is [23]:

$$R_H = \frac{12\mu L}{wh_l^3 \left(1 - \frac{h_l}{w}\right) \left(\frac{192}{\pi^5} \sum_{n=0}^{\infty} \tanh\left(\frac{(2n+1)\pi w}{2h_l}\right)\right)} \quad (2-2)$$

where L (m) is the length of the rectangular channel, w (m) is the width of the channel, h_l (m) is the height of the channel and μ ($\text{Pa} \cdot \text{s}$) is the viscosity of the liquid.

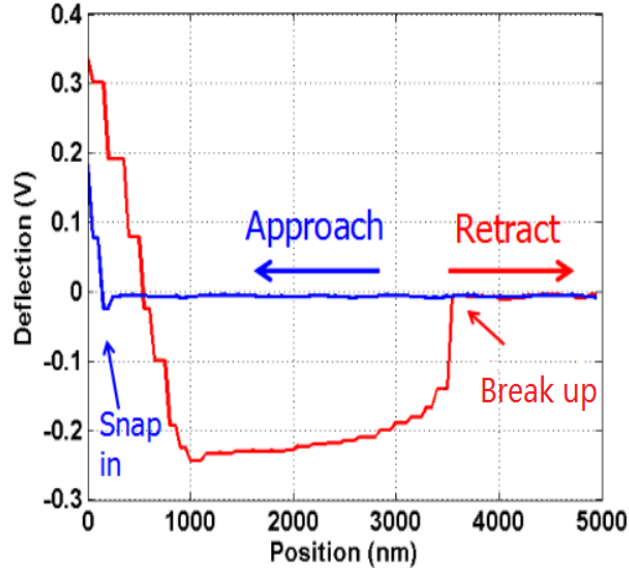


Figure 2-2: The deflection graph of AFM. the substrate (blue line); moving away from the substrate (red line). The deflection is reflected by the voltage of reflection sensor measuring the bending of cantilever.

The pressure of the liquid bridge will be calculated using the Laplace pressure formula. "The Laplace pressure is the pressure difference between the inside and the outside of a curved surface that forms the boundary between a gas region and a liquid region." [24], which can be written as [12]:

$$\Delta P = P_{inside} - P_{outside} = \gamma H \quad (2-3)$$

where P_{inside} (Pa) is the pressure inside the curved surface, $P_{outside}$ is the pressure outside the curved surface, H (1/m) is the curvature of the surface, which is sum of the two principle curvatures and γ (N/m) is the surface tension of the liquid.

2-3-2 The dynamic model

The schematic of the hollow cantilever is shown in Figure 2-3. Let us define the following quantities:

$$\Delta P_p = P_p - P_{atm}, \quad \Delta P_m = P_m - P_{atm} \quad (2-4)$$

where P_p (Pa) is the pressure provided by pressure control system, P_m (Pa) is the pressure in the liquid bridge and P_a (Pa) is the pressure of the atmosphere.

Then the flow rate Q can be expressed by the following differential equation with the hydraulic resistance R_H of the system:

$$\frac{dV}{dt} = Q = \frac{\Delta P_p - \Delta P_m}{R_H} \quad (2-5)$$

where, V (m³) is the volume of the liquid bridge. Because ΔP_p is the system input, what needs to be determined is ΔP_m . In particular, since the output of the system is the volume of the liquid bridge, it is necessary to find a relation between ΔP_m and the volume. The model

would become:

$$\frac{dV}{dt} = \frac{\Delta P_p - \Delta P_m(V)}{R_H} \quad (2-6)$$

The method to obtain the relation between pressure and volume is introduced in the following.

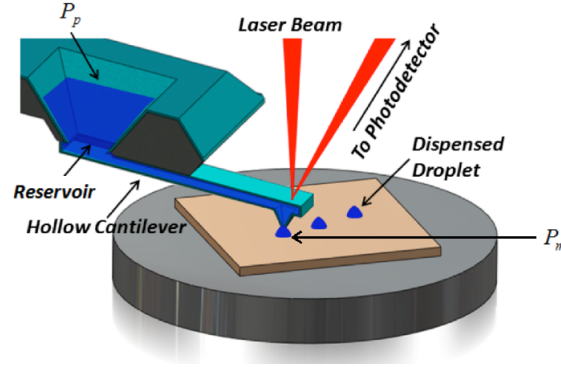


Figure 2-3: The schematic of hollow cantilever. The liquid is modelled as a uniform-viscous and incompressible Newtonian fluid (courtesy of Dr. Hector Hugo Perez Garza).

2-3-3 Young–Laplace equation

The profile of an axisymmetric liquid bridge between two solid surfaces can be described by solving Young–Laplace equation [25]. When the mean curvature is negative, and the liquid bridge is between a spherical tip and plant substrate, the solution is [19, 20]:

$$2H_{mean}R = \frac{1}{D+1-\cos(\psi)} \left(-\cos(\theta_1 + \psi) - \cos(\theta_2) - \frac{1}{k}(E(\phi_2, k) - E(\phi_1, k)) + \frac{1-k^2}{k}(F(\phi_2, k) - F(\phi_1, k)) \right) \quad (2-7)$$

where

$$k = \left(\frac{1}{1+c} \right)^{1/2}$$

$$c = 4H_{mean}^2 R^2 \sin^2(\psi) - 4H_{mean}R \sin(\psi) \sin(\theta_1 + \psi)$$

$$\phi_1 = -(\theta_1 + \psi) + 1/2\pi$$

$$\phi_2 = \theta_2 - 1/2\pi$$

The parameters are shown in Figure 2-4, H_{mean} is the mean curvature of the liquid bridge, which is the mean of two principle curvatures. So we obtain $H = 2H_{mean}$. R is the radius of the sphere, D is the distance between the sphere and plane, F is the elliptic integral of the first kind, E it the elliptic integral of the second kind.

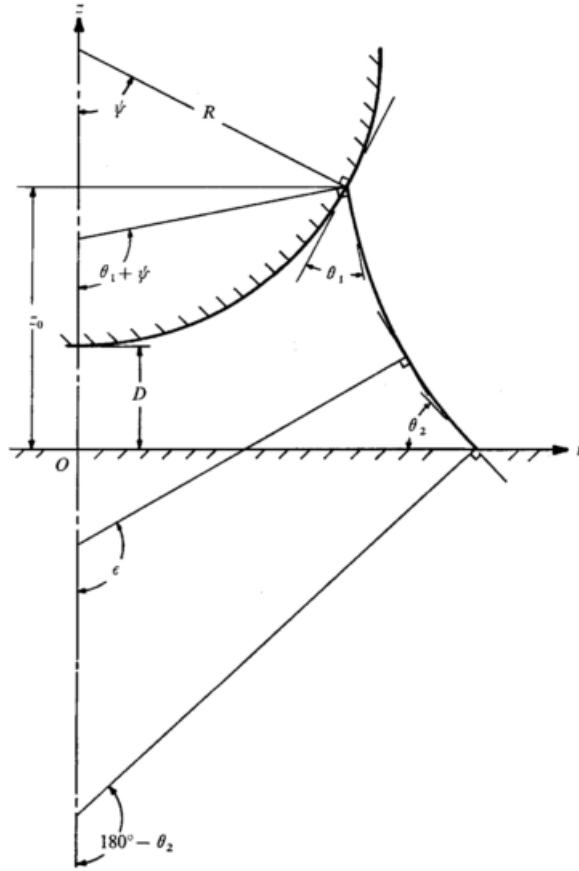


Figure 2-4: The liquid bridge between a sphere and plane [19].

Because the tip of hollow cantilever can be treated a pyramid, (2-7) has to be changed to match the situation shown in Figure 2-5. The new equation is:

$$2H_{mean}R_1 = \frac{1}{d} \left\{ -\cos(\theta_1 + \psi) - \cos(\theta_2) - \frac{1}{k} \left(E(\phi_2, k) - E(\phi_1, k) \right) + \frac{1-k^2}{k} \left(F(\phi_2, k) - F(\phi_1, k) \right) \right\} \quad (2-8)$$

where

$$d = \frac{y_1 + D}{R_1} = \frac{1}{\tan(\frac{\pi}{2} - \psi)} \sin \psi + \frac{D}{R_1}$$

where R_1 is the radius of the circle which is tangent to the edge of the pyramid tip and pass through the point where the liquid bridge connecting with the tip. The other parameters are the same with equation (2-7).

Dynamic contact angle has a complex behavior for different liquids. For most liquids the advancing angle is the same when the radius of droplet increases [26]. The receding angle is more complex than the advancing contact angle. The receding contact angle can change with volume [27]. For small volumes, it is easy for the three phase boundary of the liquid bridge to increase with increase in volume [16]. When considering dispensing process via hollow cantilever (for small volume) the distance between the tip and substrate D is 0, and the angles θ_1 , θ_2 in (2-8) can be treated as constant values. As a result (2-8) becomes an

equation with the only variable $H_{mean}R_1$. So we can define $2H_{mean}R_1$ as:

$$HR_1 = 2H_{mean}R_1 = c_1 \quad (2-9)$$

In this situation c_1 is constant number. As for the aspirating process, because θ_1 and θ_2 may not be constant, c_1 can change for different volume.

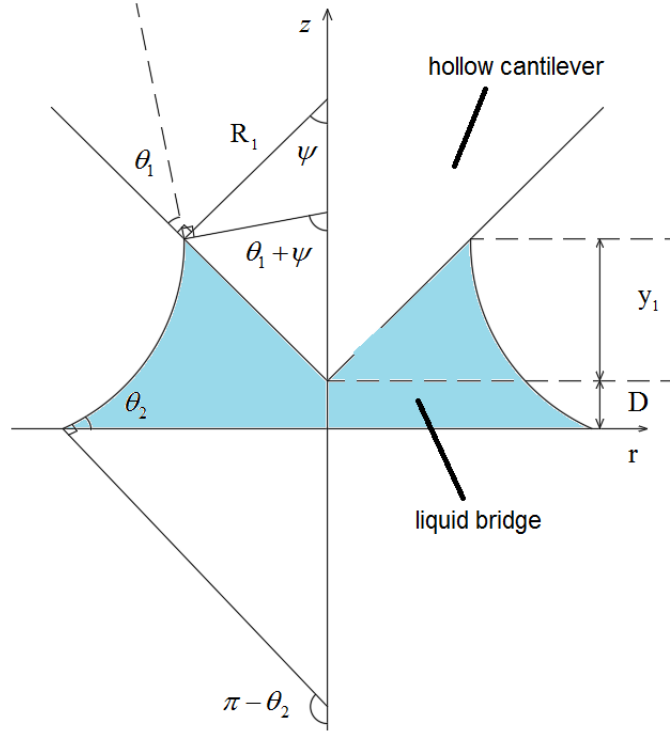


Figure 2-5: The liquid bridge between a pyramid and plane.

If the distance D between the tip and substrate is not zero, c_1 will change when the volume changes. As for large volume of the liquid bridge, there are three situations, which is shown in Figure 2-6. In the situation (a), the distance D is small, but R_1 and y_1 are large. In the situation (b), the distance D is large, while R_1 and y_1 are small. In the situation (c), D , R_1 and y_1 are large. Because $d = \frac{y_1 + D}{R_1}$, in the situation (a), the part $\frac{D}{R_1}$ can be neglected, d can be approximated as the situation when the distance D is zero. In the situation (b), D is much larger than R_1 and y_1 . The relation between HR_1 and the ratio of $\frac{D}{R_1}$ is shown in Figure 2-7 where $\theta_1 = 20^\circ$, $\theta_2 = 20^\circ$ and $\psi = 35^\circ$. We can see when the distance D is becomes larger HR_1 becomes smaller and changes slowly. So in this situation HR_1 can be treated as a small value near zero. In the situation (c), because R_1 , y_1 and D are very large, so when there is small increase of the liquid bridge, just small increase happens in y_1 and D . d can be treated as constant. According to equation (2-8), HR_1 is constant when θ_1 , θ_2 and ψ do not change. So we can conclude when the volume of the liquid bridge is very large and the change of volume is small, even distance D is not zero, c_1 can be treated as constant (not the same in different situations). The volume V of the liquid bridge between the pyramid

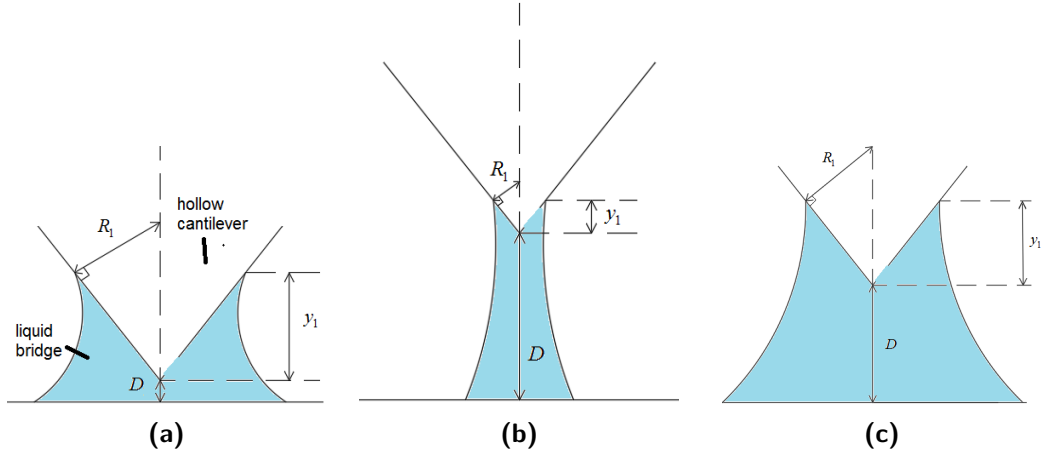


Figure 2-6: Three situations of large liquid bridge when the distance between tip and substrate is not 0.

tip and substrate can be calculated as:

$$V = \int_{\pi-\theta_2}^{\theta_1+\psi} \frac{\pi}{(2c_1)^3} \left(\sin^2(x) - 2\sin(x)(\sin^2(x) + c)^{1/2} + \sin^2(x) + c \right) \left(\sin(x) - \frac{\sin^2(x)}{\sqrt{(\sin^2(x)+c)}} \right) dx R_1^3 - \frac{1}{3} \frac{\sin^4 \psi}{\cos \psi} R_1^3 \quad (2-10)$$

So for constant θ_1 , θ_2 and ψ , the volume is:

$$V = c_2 R_1^3 \quad (2-11)$$

where c_2 is a constant:

$$c_2 = \int_{\pi-\theta_2}^{\theta_1+\psi} \frac{\pi}{(2c_1)^3} \left(\sin^2(x) - 2\sin(x)(\sin^2(x) + c)^{1/2} + \sin^2(x) + c \right) \left(\sin(x) - \frac{\sin^2(x)}{\sqrt{(\sin^2(x)+c)}} \right) dx - \frac{1}{3} \frac{\sin^4 \psi}{\cos \psi} \quad (2-12)$$

According to equation (2-9) and (2-11), the ΔP_m in equation (2-6) can be calculated as:

$$\Delta P_m = \gamma c_1 \sqrt[3]{\frac{c_2}{V}}$$

So the model in equation (2-6) becomes:

$$\frac{dV}{dt} = \frac{\Delta P_p - \gamma c_1 \sqrt[3]{\frac{c_2}{V}}}{R_H} \quad (2-13)$$

When the mean curvature is positive, the model (2-13) can be obtained in the similar way, but c_1 has positive value.

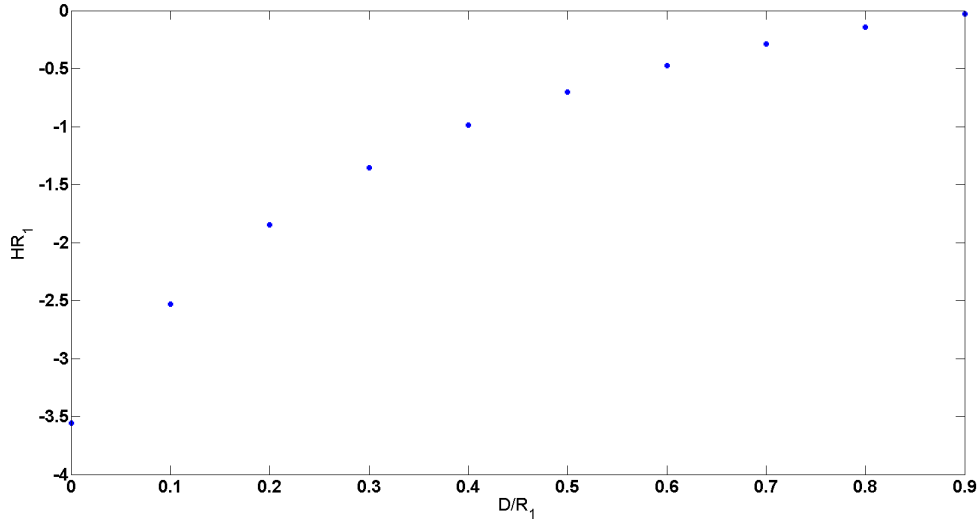


Figure 2-7: The relation between HR_1 and $\frac{D}{R_1}$ when $\theta_1 = 20^\circ$, $\theta_2 = 20^\circ$ and $\psi = 35^\circ$.

2-4 Volume and Contact angle Measurement

2-4-1 Volume Measurement

In (2-10), the method gives the relation between the volume and R_1 . But R_1 cannot be measured. To control the dosing process, the liquid volume has to be measured. The volume can be measured according to the break-up height.

The volume of the liquid V_h is calculated based on the shape of the liquid bridge at the break up instant, as shown in Figure 2-8. The model assumes that the radius r of the liquid bridge is constant. If the contact angle θ (when the liquid bridge breaks) is known, the volume can be calculated as:

$$V_h = \pi \left\{ \frac{2h^3}{\cos^2 \theta} - \frac{h^3}{3} - 2 \frac{h^3}{\cos^3 \theta} \left(\frac{1}{2} \cos \theta \sqrt{1 - \cos^2 \theta} + \frac{1}{2} \sin^{-1}(\cos \theta) \right) \right\} \quad (2-14)$$

To check the volume calculated from the break up height, another way to calculate volume is according to the droplet remains on the substrate, which is defined as V_c (m^3). When the liquid is totally separated from the tip, the shape of the droplet is spherical cap and the model used to calculate the volume of the droplet is shown in Figure 2-9.

If the contact angle β and the base radius of the droplet r_1 are known, the volume V_c can be calculated as:

$$V_c = \frac{\pi h}{6} (3r_1^2 + h_1^2) \quad (2-15)$$

where,

$$h_1 = r_c - h_c$$

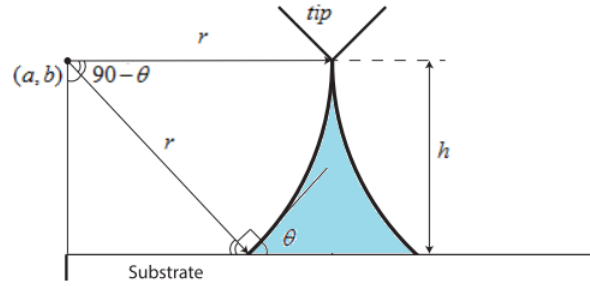


Figure 2-8: A schematic picture of the event just before the liquid bridge breaks from the cantilever tip.

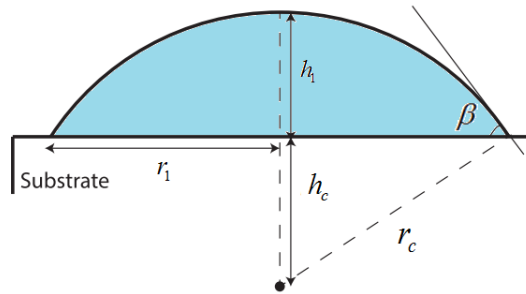


Figure 2-9: A schematic of a droplet on the substrate.

$$r_c = \frac{r_1}{\sin(\beta)}$$

$$h_c = r_1 \tan\left(\frac{\pi}{2} - \beta\right)$$

2-4-2 Contact angle measurement

The contact angle θ is an important parameter to calculate the volume. However, it is hard to measure at the micro-scale; for this reason we measure in the macro-scale before gravity effects the droplet shape.

The device uses a dispensing needle to dispense liquid on the substrate and a camera to capture the image of the liquid bridge. The contact angle θ (Figure 2-8) can be obtained by an image analysis software. The working principle of the software is to approximate the 2-D boundary shape of the liquid bridge with the arc of a circle: the contact angle is obtained by using the approximated circle and the substrate. When the droplet is small enough, gravity can be ignored. This assumption is reasonable if the base radius of droplet r_1 is smaller than the capillary length l_c (m):

$$r_1 < l_c = \sqrt{\frac{\gamma}{\rho g}} \quad (2-16)$$

where ρ (kg/m³) is the density and g (m/s²) is the gravitational constant.

2-5 Property of the dynamic model

2-5-1 Profile of the liquid bridge

Assume R_1 in equation (2-8) as 1, for a pyramid tip with $\psi = 35^\circ$, and change contact angles θ_1 and θ_2 , the shape of the liquid bridge is shown in Figure 2-10 and Figure 2-11. In Figure 2-10, the red line is the edge of the pyramid tip. When θ_1 increases, the liquid bridge is drawn according to the c_1 calculated from equation (2-8). It is seen that the contact angle between the tip and liquid bridge increases as expected. In Figure 2-11, the red line is also the edge of the tip. As θ_2 increases, the contact angle between the substrate and the liquid bridge increases as expected. For both situations, the liquid bridge can perfectly touch the substrate and the side of the tip, which means that the liquid bridge drawn according to the equation (2-8) can match the geometry of the liquid bridge.

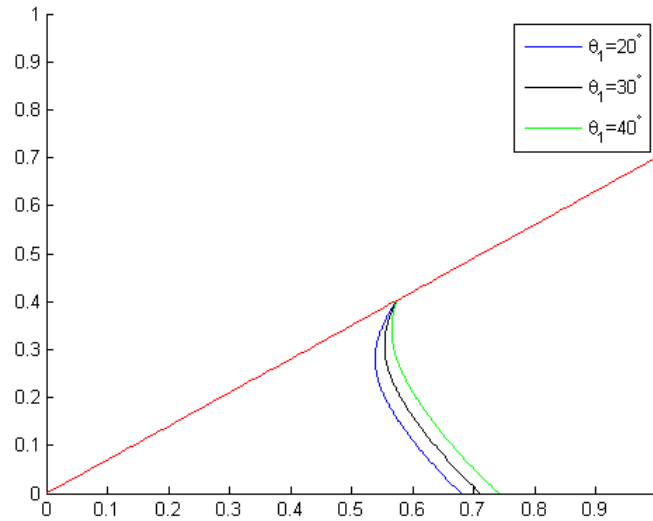


Figure 2-10: The shape for the liquid bridge when contact angle θ_1 changes.

2-5-2 Property of the parameter $c_1 \sqrt[3]{c_2}$.

How the parameters $c_1 \sqrt[3]{c_2}$ in the model (2-13) changes for different contact angles and shape of pyramid tip is discussed here. When the angle ψ is 35° and contact angle θ_2 is 20° , the contact angle θ_1 changes from 20° to 60° , the change of $c_1 \sqrt[3]{c_2}$ in model (2-13) is shown in Figure 2-12. When the contact angle ψ is 35° and contact angle θ_1 is 20° , the angle θ_2 changes from 20° to 60° , the change of $c_1 \sqrt[3]{c_2}$ in model (2-13) is shown in Figure 2-13. When the angle θ_1 is 20° and contact angle θ_2 is 20° , the angle ψ changes from 20° to 60° , the change of $c_1 \sqrt[3]{c_2}$ in model 2-13 is shown in Figure 2-14.

From Figure 2-12 and Figure 2-13 when the contact angle θ_1 becomes larger or the contact angle θ_2 becomes larger, then the absolute value of $c_1 \sqrt[3]{c_2}$ becomes smaller, which means that absolute value of ΔP_m in the model (2-13) becomes smaller. As our expect, when the

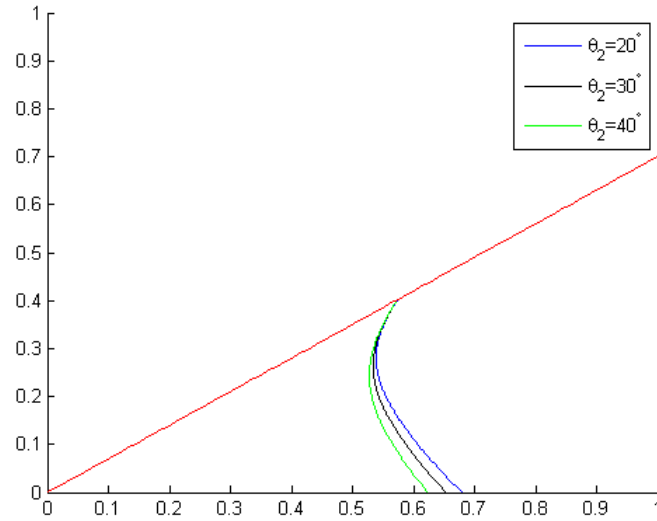


Figure 2-11: The shape for the liquid bridge when contact angle θ_2 changes.

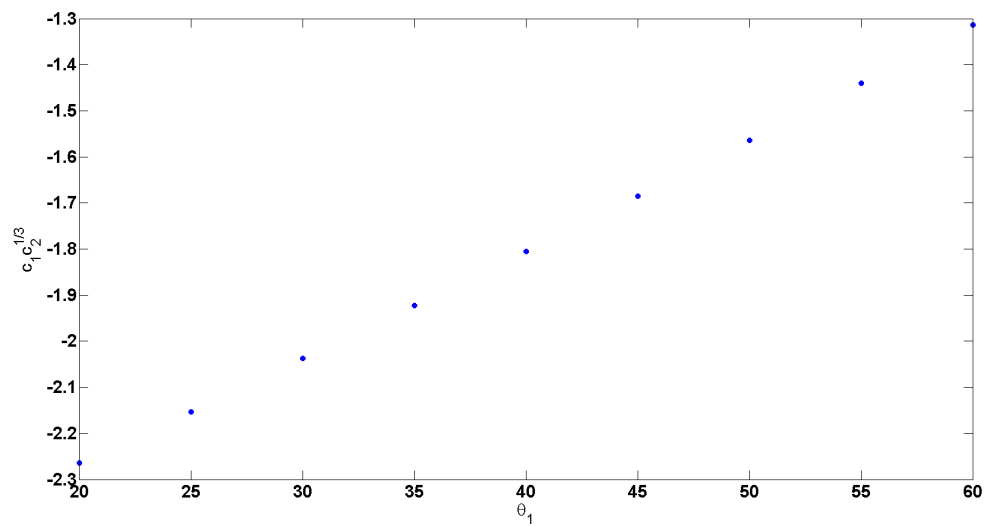


Figure 2-12: Value of $c_1 \sqrt[3]{c_2}$ when θ_1 changes if θ_2 and ψ are constant.

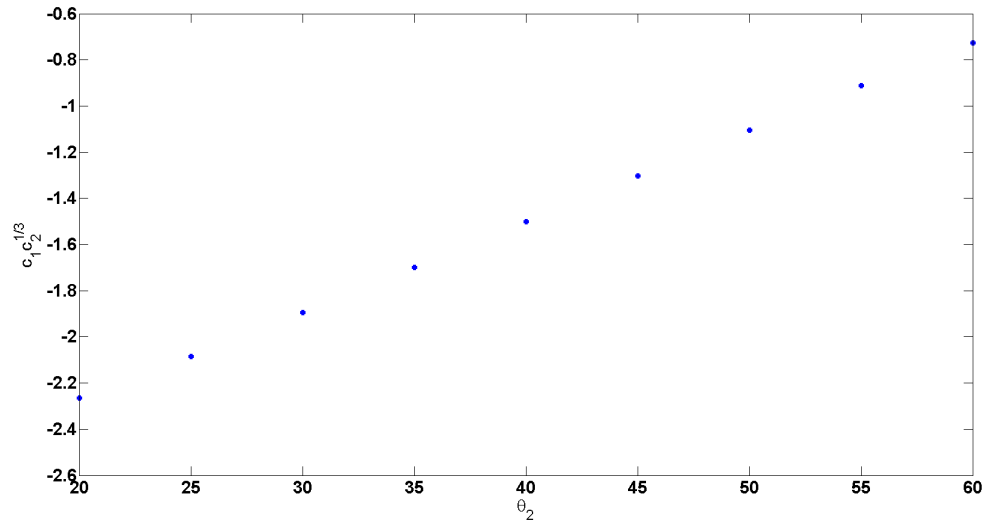


Figure 2-13: Value of $c_1 \sqrt[3]{c_2}$ when θ_2 changes if θ_1 and ψ is constant.

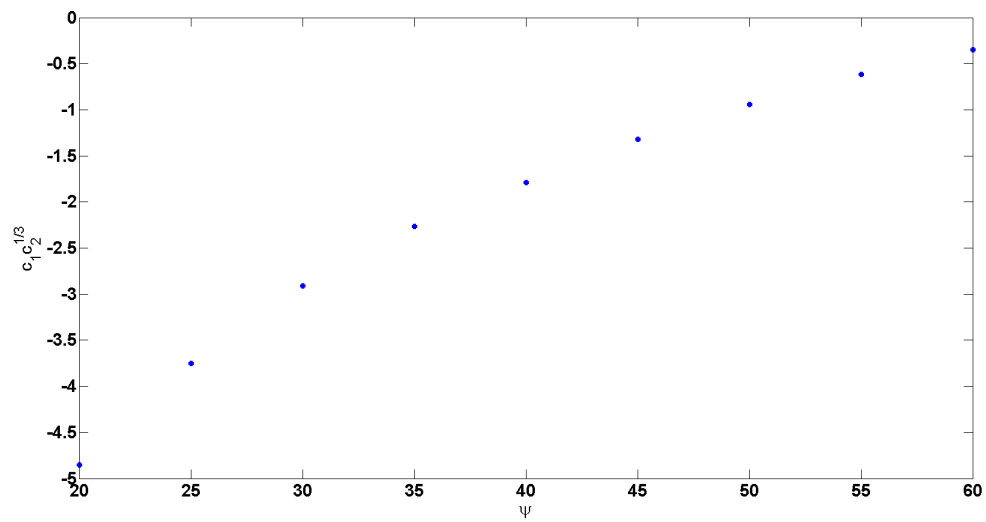


Figure 2-14: Value of $c_1 \sqrt[3]{c_2}$ when ψ changes if θ_1 and θ_2 are constant.

substrate or the tip is more hydrophobic, the drag pressure comes from the liquid bridge becomes smaller. As for the pyramid tip is more sharp, from Figure 2-14, the drag pressure also becomes smaller. It shows that the shape of the tip is also an important factor influencing the dosing process. When pyramid tip is separated from the substrate with distance D , the parameter $c_1 \sqrt[3]{c_2}$ changes with the ratio D/R_1 is shown in Figure 2-15, when angel $\psi = 35^\circ$, $\theta_1 = 20^\circ$ and $\theta_2 = 20^\circ$. From Figure 2-15, the absolute value of $c_1 \sqrt[3]{c_2}$ becomes smaller when the distance between the tip and substrate increases, which means the drag pressure from the liquid bridge becomes smaller during the separation process.

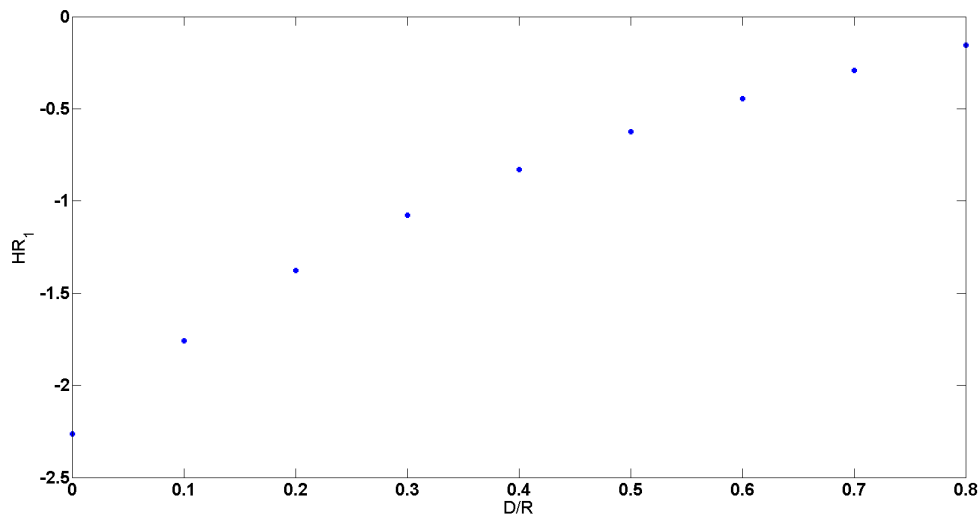


Figure 2-15: $c_1 \sqrt[3]{c_2}$ when the tip retracts from substrate.

2-5-3 Capillary force validation

There is an experiment of the capillary force [21]. The capillary force can be calculated by the surface tension and Laplace pressure. The formula to calculate the capillary force is [28]:

$$F_C = F_T + F_L = 2\pi r_{tip} \gamma \sin(\theta_1 + \phi_1) - \Delta P_m \pi r_{tip}^2 \quad (2-17)$$

F_C is the capillary force, F_T is the force from surface tension and F_L is the force from Laplace pressure. r_{tip} is the radius where the liquid bridge connects with the tip, which is shown in Figure 2-16.

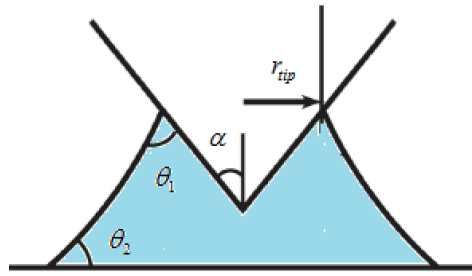


Figure 2-16: The model to calculate capillary force.

In the experiment, α is 38° , the receding angle of the liquid is 15° and advancing angle is 50° . So choose $\theta_2 = 40^\circ$ between the two dynamic angles, choose $\theta_1 = 20^\circ$. The distance between the tip and substrate is 0. By using equation (2-8), equation (2-3) and equation (2-17), the capillary force can be calculated. The capillary force according to our model and the experimental data is shown in Table 2-1. The results are almost the same. This validates our model. And the capillary force from surface evolver can also match the experimental result [21].

Table 2-1: The capillary force from experiment [21] and the model.

length of r_{tip}	capillary force from paper (nN)	capillary force from model(nN)
$r_{tip} = 1\mu m$	about 380	385
$r_{tip} = 0.89\mu m$	about 340	343
$r_{tip} = 0.63\mu m$	about 240	243

2-6 Conclusion

By using Young-Laplace equation and circuit analogy method, the dynamic model for the dosing process was obtained. The profile of the liquid bridge was successfully obtained for various contact angles. When the curvature is negative and the volume of the bridge does not change, it is found that the Laplace pressure inside the liquid bridge decreases for the following situations: 1) when the tip is hydrophobic, 2) when the substrate is hydrophobic, 3) when the tip becomes sharper. For a static situation—when no pressure was applied in the reservoir, the model was validated for the capillary forces, matching with the reported experimental data in the literature.

Chapter 3

Experiments

3-1 Introduction

The model of the dosing process has been developed in the last chapter. In this chapter, experiments are designed to validate the model. In the section 3-2, experiments with nano-litre scale droplets have been made by using precision tip. The dispensing process in the experiments can be recorded by camera, which is intuitive. The experimental results can be predicted by using the Laplace pressure calculated according to the liquid bridge shape. In the section 3-3, experiments by using hollow cantilever have been done. It is demonstrated that the proposed model can describe the dosing process with VAF larger than 90%. VAF is used to assess the quality of a model, which is defined as:

$$VAF = \left(1 - \frac{\frac{1}{N} \sum_{k=1}^N \|y(k) - y_m(k)\|_2^2}{\frac{1}{N} \sum_{k=1}^N \|y(k)\|_2^2}\right) \cdot 100\%$$

where $y(k)$ is the experimental data and $y_m(k)$ is the data from model. VAF values close to 100% indicates that the model is a good representation of the physical process.

3-2 Experiments with nano-litre droplets

3-2-1 Experimental set up

When dose liquid by using hollow cantilever, the process can not be observed directly. To have a better understand of the dosing process, and check the Laplace pressure which is derived form hydrostatic situation can influence the dosing process, experiments have been done by using precision hollow tip, which is shown in Figure 3-1. The inner diameter of the tip is $100 \mu\text{m}$ and the outer diameter of the tip is $240 \mu\text{m}$. The image of the experimental set up is shown in Figure 3-2. The tygon tube connecting the precision tip and pressure control system is fixed in the movable stage, which can move in the horizontal direction. The experiments

are recorded by camera with 30 frames one second. The geometry information of the liquid bridge and droplets remain on the substrate is extracted by using image analysis Matlab code. The geometry information is used to calculate the volume of liquids. Water is used in these experiments. The precision tip is used to dispense liquid when the tip suspends in the air in the section 3-2-3 and touches the substrate in the section 3-2-4. When cut the stainless tube of the precision tip to the yellow glue part. The top of yellow glue can touch the substrate. The shape of the glue is conical, which is similar with the tip of hollow cantilevers, so other experiments are done by using the clipped precision tip.

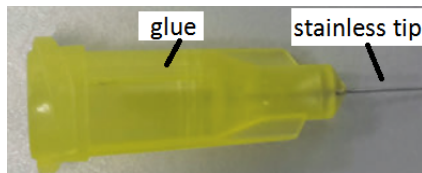


Figure 3-1: Precision tip.

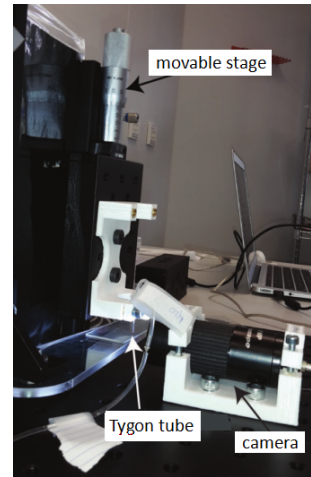


Figure 3-2: The frame of the liquid droplet remains on the substrate.

3-2-2 Volume check

To check the circular approximation method is suitable to calculate the volume by using the break-up height (2-14), use the camera to record the dispensing process of clipped precision tip. Use circular approximation method to calculate the volume by the last frame in the recorded video before the liquid bridge breaks, which is shown in Figure 3-3. And use the volume of spherical cap droplets remain on the substrate as the real volume (2-15), which is shown in Figure 3-4. Seven different experiments have been done, the result is shown in Figure 3-5. It shows that the volume calculated by the circular approximation method is always smaller than the volume calculated by the droplets remain on the substrate. The reason is that in Figure 3-3 the shape of the yellow glue is not conical, the top of it is more flat. So the schematic of the liquid bridge shown in Figure 2-8 used to calculate the volume should be changed to the one shown in Figure 3-6. The green part is the tip, the blue part is the volume calculated according to (2-14). And the yellow part is the extra volume, the shape of it is cylinder.

3-2-3 Precision tip suspending in the air

In this experiments, the precision tip suspends in the air, and is connected with the pressure control system that can provide different pressure. Liquids go out from the aperture of the



Figure 3-3: The last frame before the liquid bridge breaks.

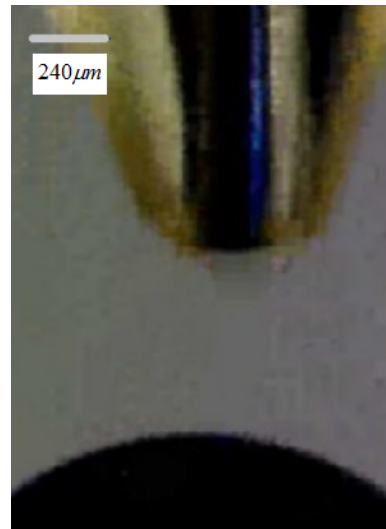


Figure 3-4: The frame of the liquid droplet remains on the substrate.

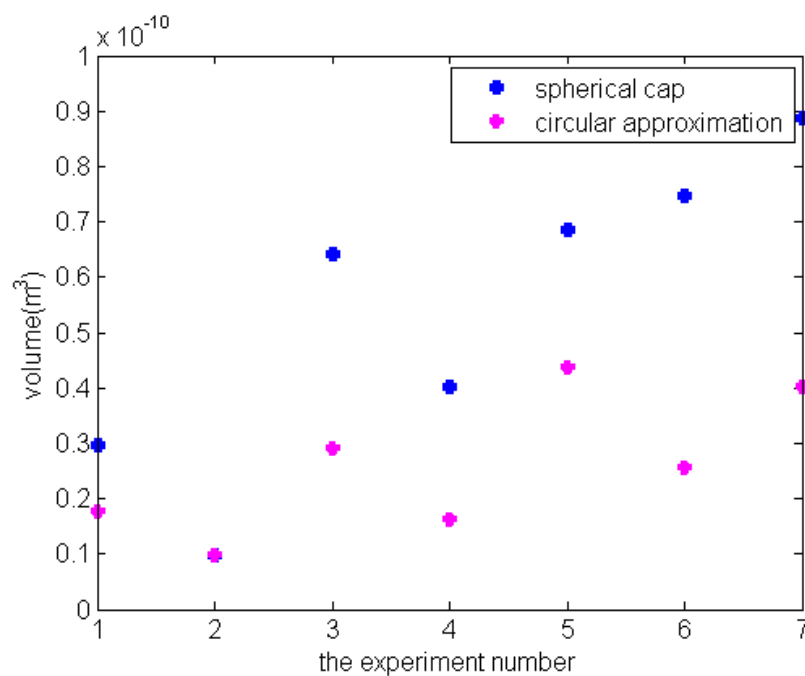


Figure 3-5: Volume comparison by using droplet remains on the substrate and circular approximation.

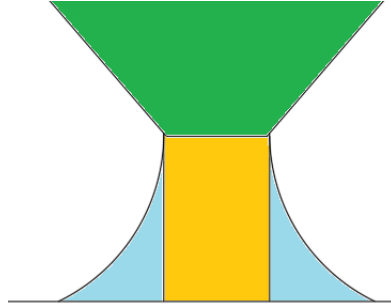


Figure 3-6: Schematic of why the volume calculated from spherical cap remains on the substrate larger than the volume from circular approximation (the green part is the tip, the blue part is the volume calculated according to (2-14) and the yellow part is the extra volume).

tip, the shape of the liquid can be treated as spherical cap with constant base diameter, which is shown in Figure 3-7. The equation to calculate spherical cap volume is:

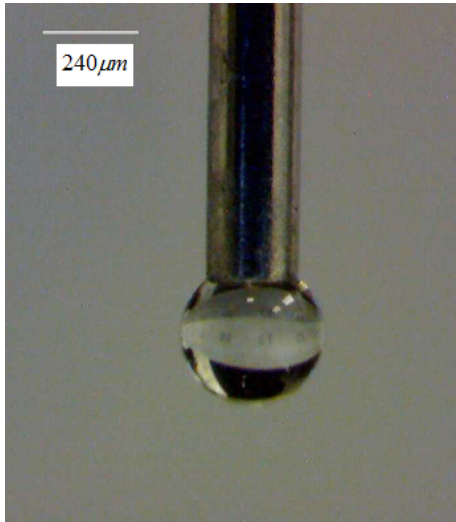


Figure 3-7: The liquid hanging at the precision tip.

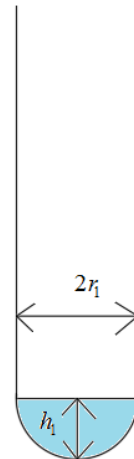


Figure 3-8: The parameters of the volume function when droplet hangs at the precision tip.

$$V = \frac{1}{6}\pi h_1[3(r_1)^2 + h_1^2] \quad (3-1)$$

where h_1 is the height of the spherical cap and r_1 is the base diameter which is shown in Figure 3-8.

The radius of the spherical cap r_c is:

$$r_c = \frac{h_1^2 + r_1^2}{2h_1} \quad (3-2)$$

And from Laplace pressure equation, the pressure of the spherical cap is:

$$\Delta P_m = \gamma \frac{2}{r_c} \quad (3-3)$$

For different volume, the corresponding height can be calculated and the base diameter is a constant. Then the radius r_c can be easily obtained. The Laplace pressure for different volume can be calculated. According to (2-6), the Laplace pressure ΔP_m will influence the volume of the liquid spherical cap hanging at the precision tip when provide external pressure ΔP_p for different time. In the experiments, the inner diameter of the tip is about $100 \mu\text{m}$, the outside diameter of the tip is about $240 \mu\text{m}$. Provide $2 \times 10^3 \text{ Pa}$, $3 \times 10^3 \text{ Pa}$ and $4 \times 10^3 \text{ Pa}$ from 0.3s to 0.8s. The experimental results are shown in Figure 3-9, 3-10 and 3-11. The blue dots are the experimental data calculated by the frames captured. The red dots are the result calculated by using the model considering the Laplace pressure. And the black dots are the result neglecting Laplace pressure, assuming it is linear relation between provided pressure and flow rate. The green line is the Laplace pressure. From the figures, it shows that the model considering the Laplace pressure can match the data very well. The difference between the model without the Laplace pressure and experimental data becomes smaller for increased provided pressure. It can be explained that the Laplace pressure is smaller compared to the provided pressure, which has less influence. The hydraulic resistance used in the simulation result is $0.6 \times 10^{14} \text{ Pa} \cdot \text{s}/\text{m}^3$, which is calculated from the experiments when the precision tip touches the substrate.

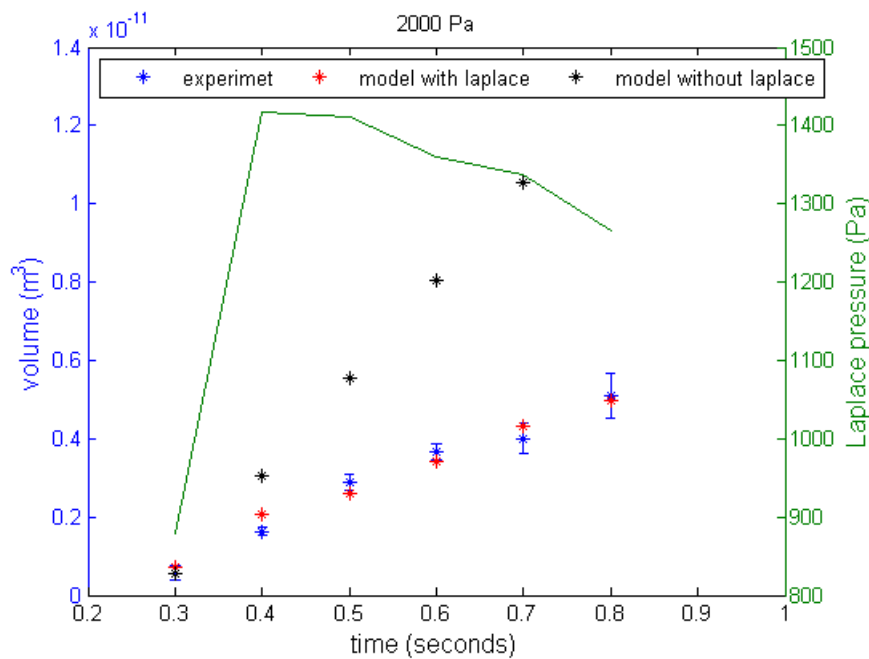


Figure 3-9: Provide 2000 Pa when the liquid hanging at the aperture of precision tip (green line is the Laplace pressure).

3-2-4 Precision tip touching the substrate

When the precision tip touches the substrate, because the tip is not pyramid, the model (2-13) can not be applied. But from the experiments, the liquid bridge can be treated as spherical cap with constant contact angle which is shown in Figure 3-12.

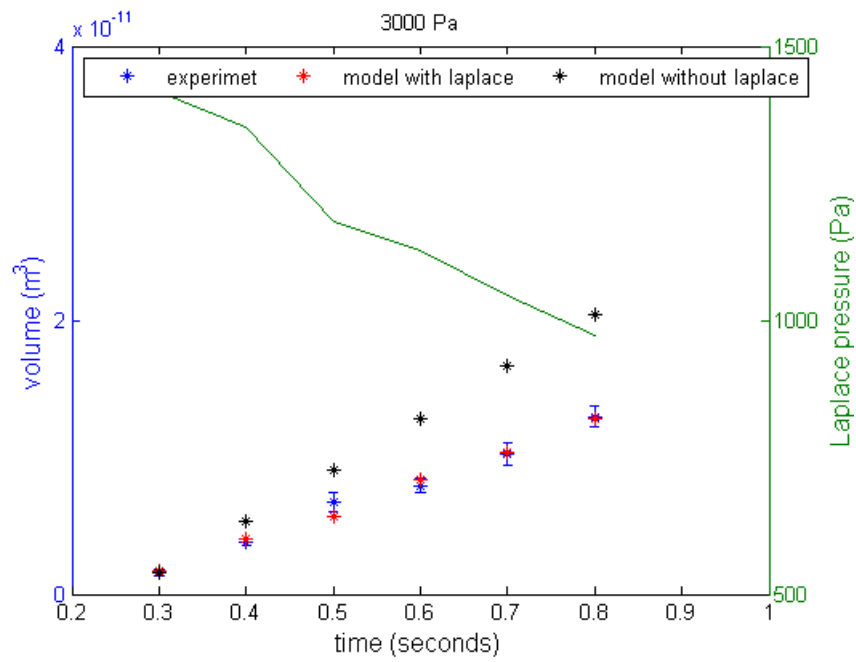


Figure 3-10: Provide 3000 Pa when the liquid hanging at the aperture of precision tip (green line is the Laplace pressure).

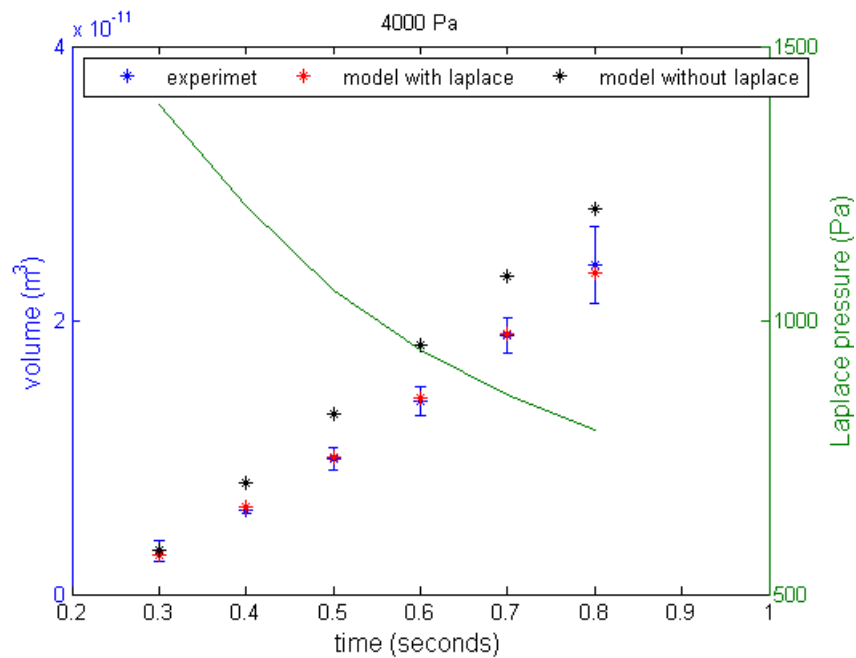


Figure 3-11: Provide 4000 Pa when the liquid hanging at the aperture of precision tip (green line is the Laplace pressure).

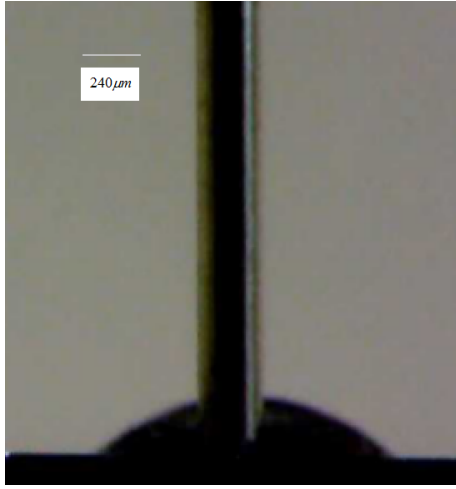


Figure 3-12: The shape of the liquid when precision tip touches with the substrate.

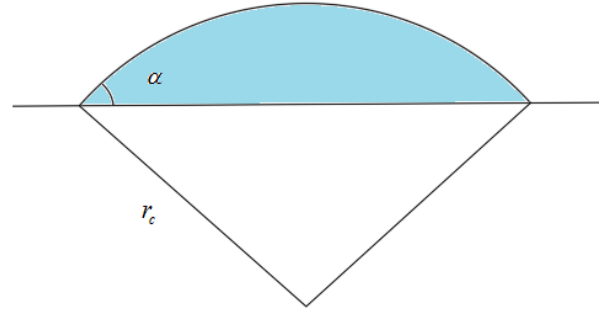


Figure 3-13: The parameters of the volume function when precision tip touches the substrate.

For the spherical cap with constant contact angle, the relation between the volume and radius is:

$$V = \frac{1}{6}\pi[1 - \cos(\alpha)][3 \sin^2(\alpha) + (1 - \cos(\alpha))^2]r_c^3 \quad (3-4)$$

Then the relation between volume and Laplace pressure can be obtained as:

$$\Delta P_m = 2\gamma \sqrt[3]{\frac{\frac{1}{6}\pi[1 - \cos(\alpha)][3 \sin^2(\alpha) + (1 - \cos(\alpha))^2]}{V}} \quad (3-5)$$

The parameters of this volume calculation are shown in Figure 3-13.

The experimental result when provide pressure 3×10^3 Pa is shown in Figure 3-14, and the result when provide pressure 4×10^3 Pa is shown in Figure 3-15. The hydraulic resistance used here is 0.6×10^{14} Pa · s/m³, which is calculated from the volume at 3 s and 4 s when provide 4000 Pa. From the figures, when the Laplace pressure is considered, the model can match the experimental data better. But when provide 4000 Pa, the difference between the model with Laplace pressure and without Laplace pressure is very small. The reason is that when provide 4000 Pa, the Laplace pressure changes from 248 Pa to 135 Pa. The influence of the Laplace pressure is so small. The error of the measured volume increases when volume increases. The reason is that when the volume of liquid increases, the property of the substrate may change and dirty on the substrate also influences the result. Besides that, there is artificial error.

3-2-5 Clipped tip touching the substrate

When the clipped tip touches the substrate, the liquid bridge connects the conical glue and substrate, the shape of the liquid bridge is shown in Figure 3-16. Because the shape of the tip is conical, which is similar with pyramid, model (2-13) can be used. There is just small change of c_2 . From the image of the dispensing process, the chosen angles are $\psi = 65^\circ$, $\theta_1 = 80^\circ$ and $\theta_2 = 45^\circ$. The c_1 in model (2-13) is 0.1224. For simplicity, c_2 is chosen as the largest

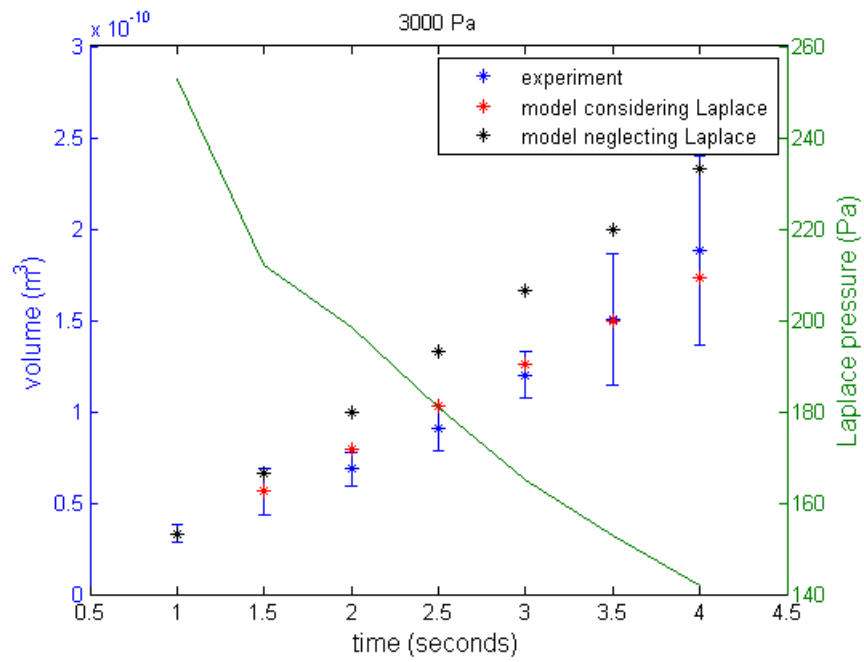


Figure 3-14: Provide 3000 Pa when the precision tip touches the substrate (green line is the Laplace pressure).

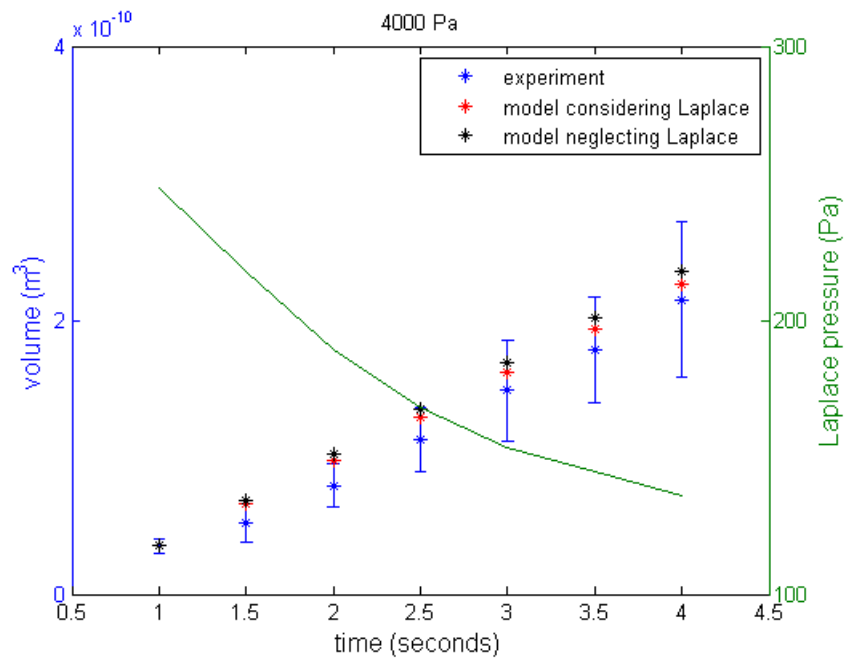


Figure 3-15: Provide 4000 Pa when the precision tip touches the substrate (green line is the Laplace pressure).

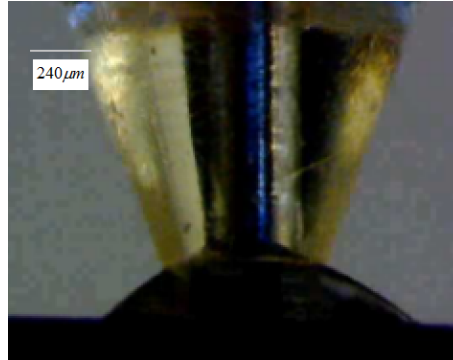


Figure 3-16: The shape of the liquid bridge when conical tip touches the substrate.

value 12. The experimental result when provide 3000 Pa is shown in Figure 3-17. Because the Laplace pressure just changes in the range 50 Pa to 90 Pa, compared to the provided pressure 3000 Pa, it can be neglected. So here just use linear fitting to match the data, which shows good result.

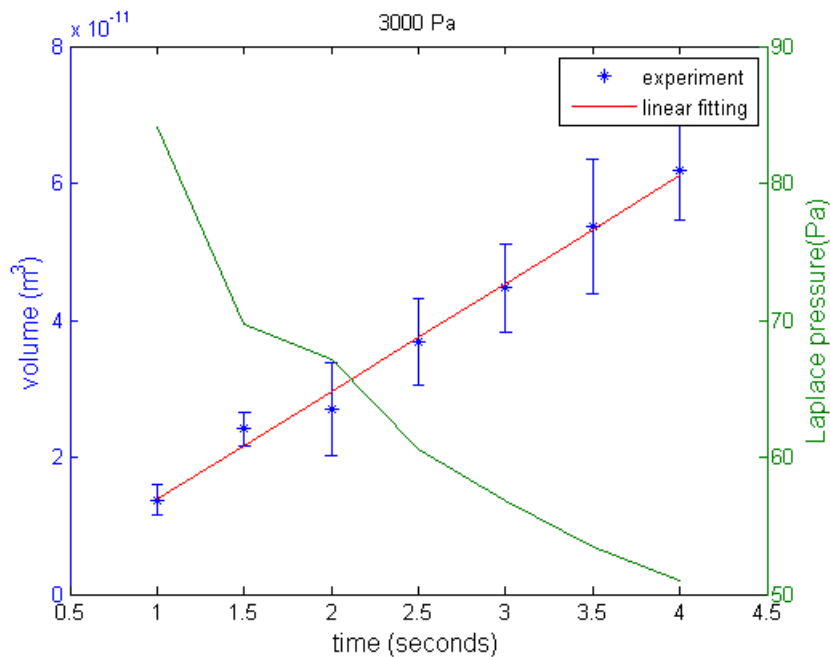


Figure 3-17: Provide 3000 Pa when the conical tip connecting with the substrate (green line is the Laplace pressure).

3-2-6 Rupture ratio

When the substrate is relatively hydrophobic, the liquids come out from the aperture of tip do not totally remain on the substrate, some will go away with the tip, which is shown in Figure 3-18. The liquid bridge breaks at the thinnest part [29]. Here the relation of liquids



Figure 3-18: When the liquid bridge breaks, some liquid goes away with the tip.

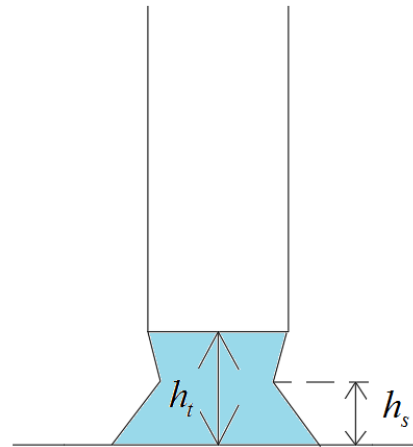


Figure 3-19: Explain of rupture ratio.

remain on the substrate and goes away with tip is described as the rupture ratio. The rupture ratio is explained by Figure 3-19, which is

$$\text{rupture ratio} = \frac{h_s}{h_t}$$

h_s is the rupture length and h_t is the total length. The influence of substrate property and aperture size is discussed in the following.

First the surface property is discussed here. The rupture ratio for three different surfaces whose contact angle are about 40° , 65° and 75° is shown in Figure 3-20, 3-21 and 3-22. When the liquid remains on the substrate has contact angle 40° , the rupture ratio is 1. From the figures, it is shown that when the volume increases the rupture ratio will increase and the rupture ratio is higher for substrates who have smaller contact angle. It means that the substrate is more hydrophilic, less liquid will go away with the tip. This is because the drag force from the substrate is larger. When the volume increases, the area of the liquid bridge connecting with the substrate increases, so the drag force from the substrate becomes large. At the same time, gravity will increase for large liquid volume. So as expected, when the volume increases, more liquids remain on the substrate.

To check the influence of aperture size. Tips with inner radius $100\mu\text{m}$ and $150\mu\text{m}$ have been chosen, the results are shown in Figure 3-23, 3-24. From the two figures, it is shown that when the aperture size is small, the rupture ratio is large for the same volume of liquid. When the aperture size becomes smaller, the connecting area between the liquid bridge and liquid inside the tip becomes smaller, so the drag force from liquid inside the tip becomes smaller. According to the experimental results, rupture ratio is related to the difference between the drag force from the tip and liquid bridge. The drag force from the substrate is larger, more liquid will remain on the substrate, the drag force from the tip is larger, less liquid will remain on the substrate. To make the dispensed liquids remain on the substrate, the tip is

functionalized by octyltrichlorosilane to make it more hydrophobic in the next experiments by using hollow cantilever.

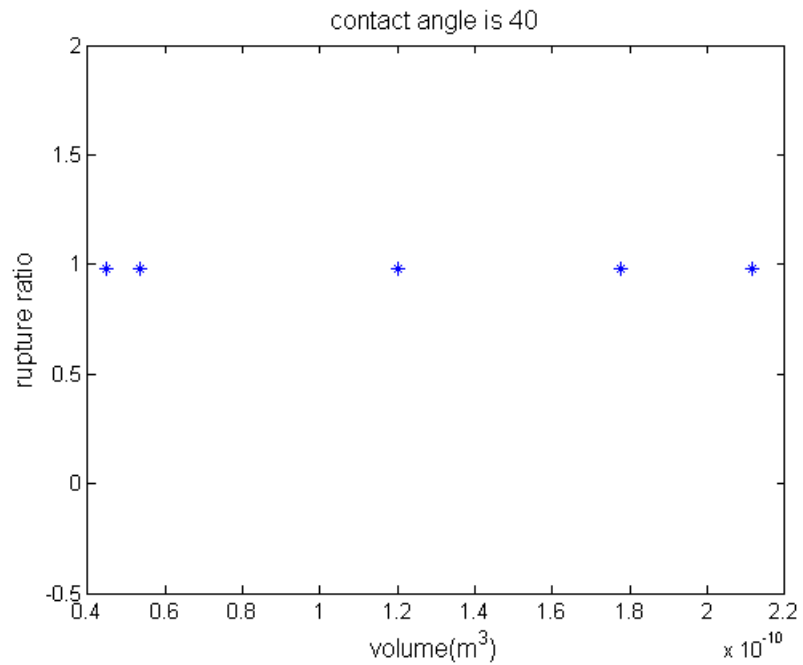


Figure 3-20: Relation between rupture ratio and volume when the contact angle is 40°.

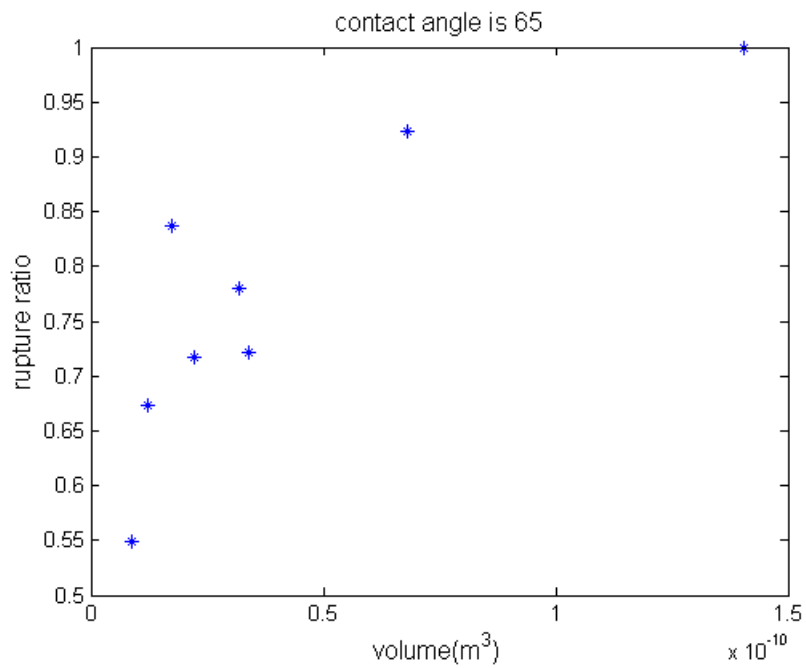


Figure 3-21: Relation between rupture ratio and volume when the contact angle is 65°.

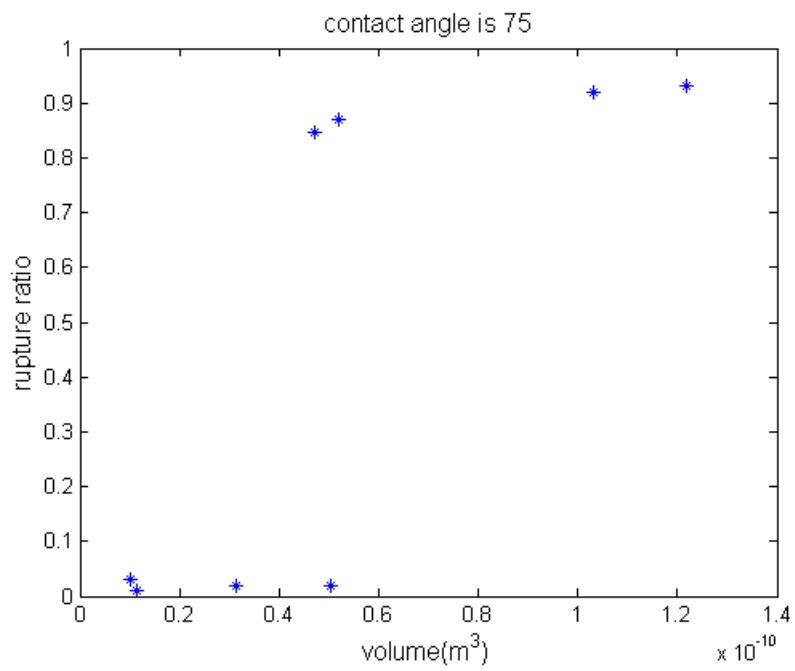


Figure 3-22: Relation between rupture ratio and volume when the contact angle is 75° .

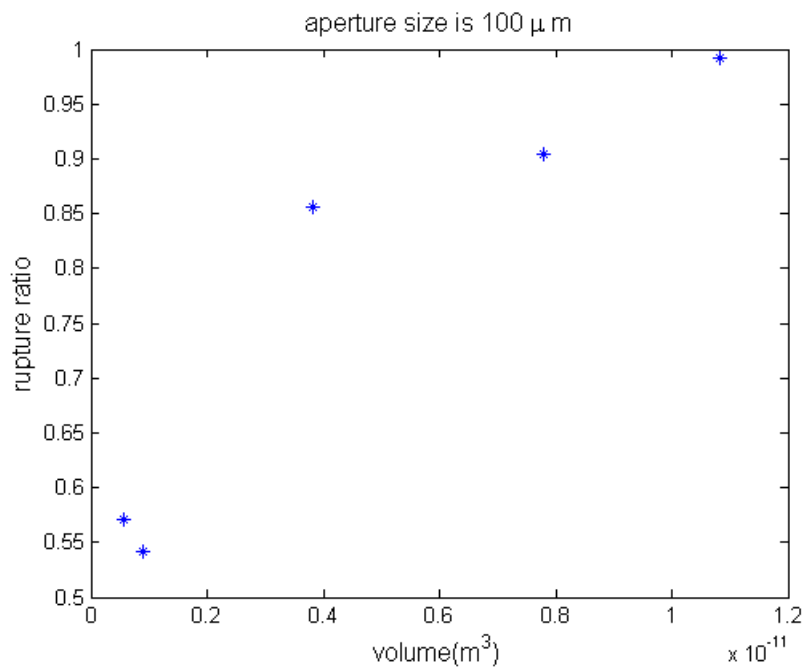


Figure 3-23: Relation between rupture ratio and volume when the diameter of the aperture is $100 \mu m$.

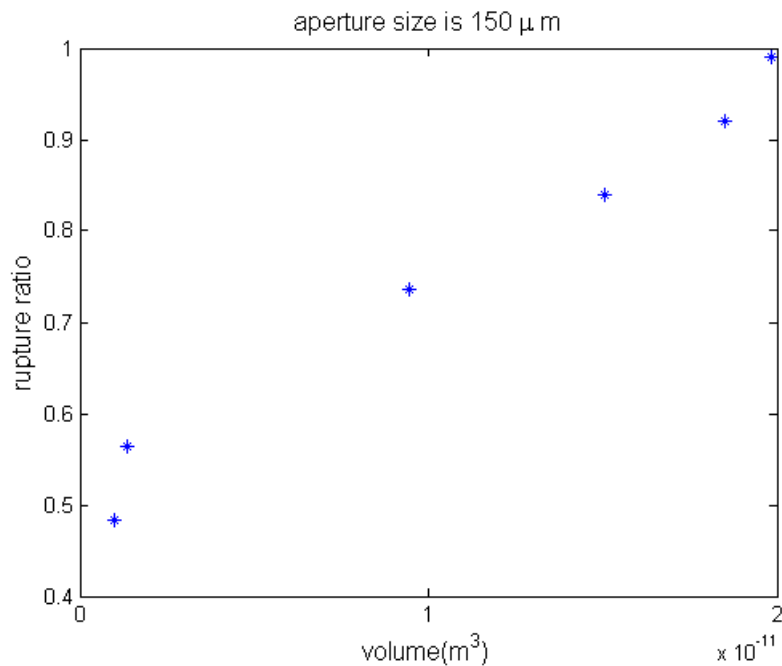


Figure 3-24: Relation between rupture ratio and volume when the diameter of the aperture is $150\mu\text{m}$.

3-3 Experiments with pico-femto-litre droplets (using hollow cantilevers)

In this section, using hollow cantilever to do experiments, the scale of the dosed liquid is from 0.01 fL to 10^4 fL. The liquid used is water with 5% glycerol.

3-3-1 Experimental set up

The various parts of hollow-cantilever constitute a basic AFM measurement system, a microfluidic chip, an automated substrate alignment, a humidity chamber and a microfluidic interface connected to an external pressure control system [30]. The set up is shown in Figure 3-25.

Microfluidic chip

The microfluidic chip consists of a hollow silicon nitride (Si_3N_4) tip and channelled silicon dioxide (SiO_2) cantilever which is connected to a fluidic reservoir located in the handling part of the chip. After filling the reservoir with liquid, a positive or negative pressure relative to the ambient is applied in the reservoir to dispense or aspirate liquids through an aperture located at the apex of the tip [30]. And two different microfluidic chips are shown in Figure 3-26.

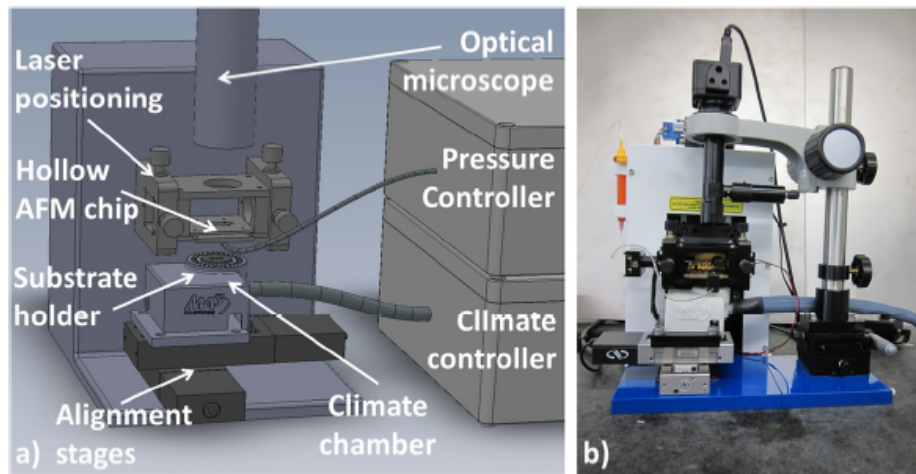


Figure 3-25: (a) Schematic representation of the set up (b) Photo of the set up [30].

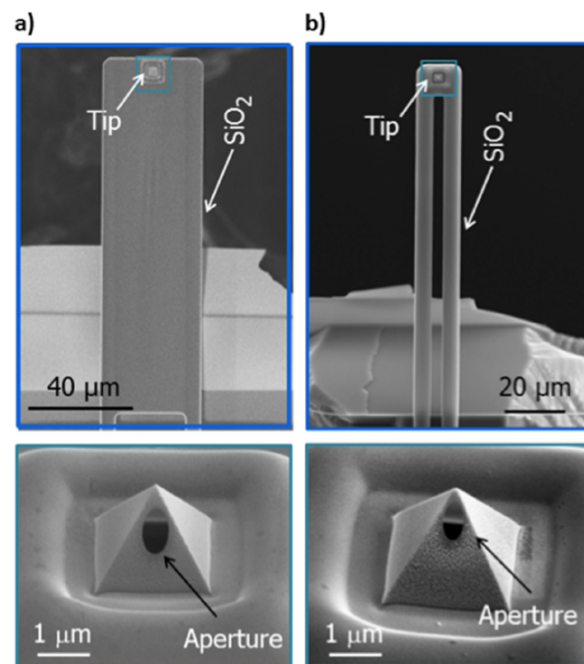


Figure 3-26: The chip contains an on-chip fluidic reservoir on the top side and hollow cantilever located at the back side of the chip. Two different kinds of chips are shown [30].

Interface

In order to connect the hollow cantilever to the pressure control system and avoid leakage during liquid transport, a microfluidic plastic interface is manufactured. Figure 3-27 shows the structure of interface. Before gluing the interface to the chip a stainless steel (SS) tube is inserted from the side into the interface and glued with Norland Optical Adhesive 86H. The cantilever chip is then glued to the resulting plastic interface using the same glue. The tube is further connected to external pressure control system by using Tygon tubing.

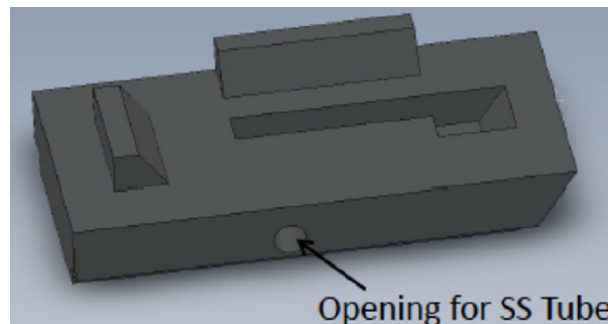


Figure 3-27: Schematic of the fluidic interface [30].

External pressure control system

The schematic of the pressure control system is shown in Figure 3-28. The pressure regulators and the valves control is USB-interfaced via National Instrument NI-6008 interface to the computer. The system includes two MAC valves, type 35A-ACA-DDAA-1BA, which have a switch time of 2-6 ms. Valve-1 switches between pressure and vacuum, while valve-2 switches between regulated and ambient pressure. Both valves have a fast response [30].

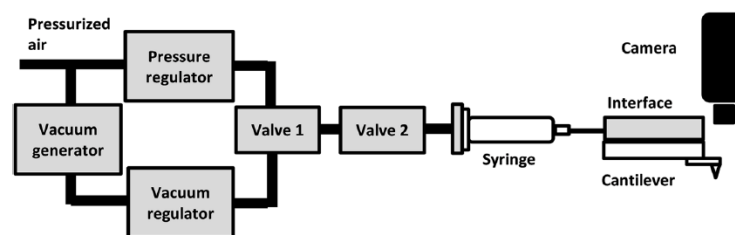


Figure 3-28: The schematic denotes the two different valves that regulate the entire system [30].

Temperature and humidity control

To supply air with a controlled temperature and humidity, compressed air is pushed through a bubbler (water bath) and a heated tube. The function of the bubbler is to humidify the air to its saturation point. The air temperature is controlled by heating or cooling the water, which is done by two peltiers-elements that can add or extract energy. This saturated air, at a controlled temperature, flows through a heated tube to increase the temperature and therefore decrease the relative humidity [30].

3-3-2 Volume Check

The visible experiment shows that it is possible to use the circular approximation method to calculate the volume. To verify using break-up height from deflection curve to calculate volume is still useful, experiments of dispensing diethyl carbonate have been done [2]. The reason of choosing diethyl carbonate is its low evaporation rate. The volume calculated according to break-up height is compared with the volume calculated from the radius of droplet. The substrate where the liquid is dispensed on is silicon. In this experiment no pressure is provided, the step size is 30 nm, the measured receding contact angle is 30.5° and the contact angle is 30° . The result is shown in Figure 3-29.

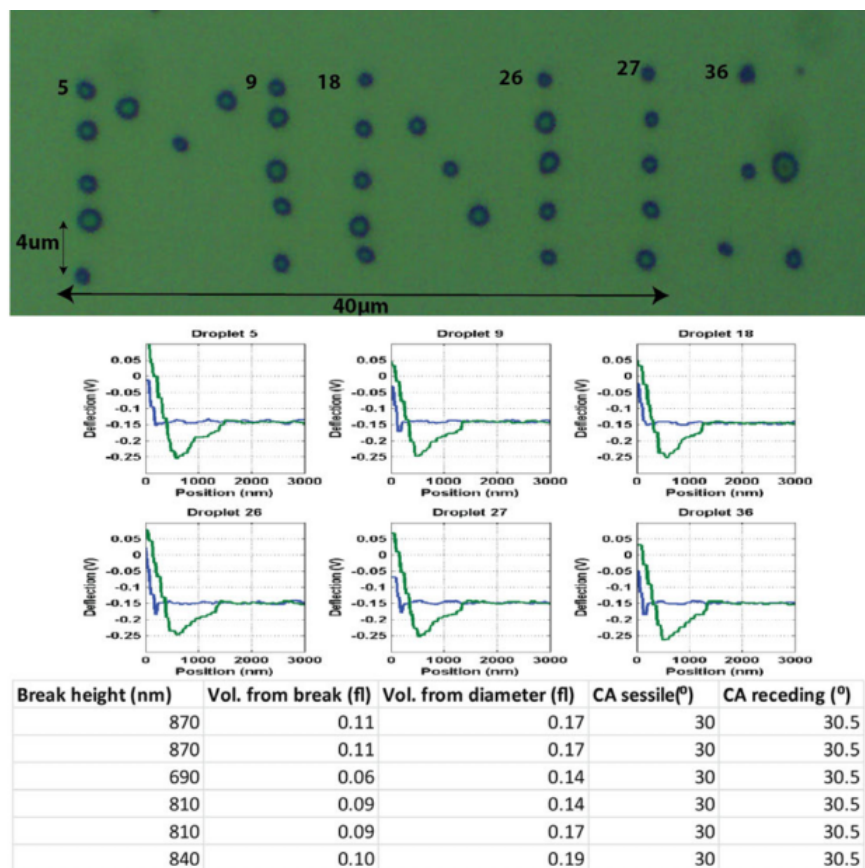


Figure 3-29: Diethyl carbonate droplets. From top to bottom: 1. The result of droplets. 2. Force distance curves of selected droplets. 3. Obtained data from the deflection distance curves and the optical image [2].

The average volume is 0.085 fL with a standard deviation of 0.028 fL when the volume is calculated according to the break-up height. And by using the radius of the droplet remains on the substrate, the average volume is 0.13 fL with a standard deviation of 0.11 fL. Because the volumes obtained by both methods are of the same order, it is concluded that using the break-up height to calculate volume is valid if the resolution required is not too high.

3-3-3 Dispensing on hydrophobic surface

Use the hollow cantilever to dispense water with 5% glycerol on SiO_2 . The contact angle is 92° , the substrate is hydrophobic and the receding angle is 75° . First the pressure provided is 1×10^5 Pa. And the contact time is from 0 s to 1 s. The result is shown in Figure 3-30. From the figure, it shows that even the 1×10^5 Pa pressure is provided for 1 s, there is not any significant increase of volume. So this means no liquid comes out from the aperture of the tip.

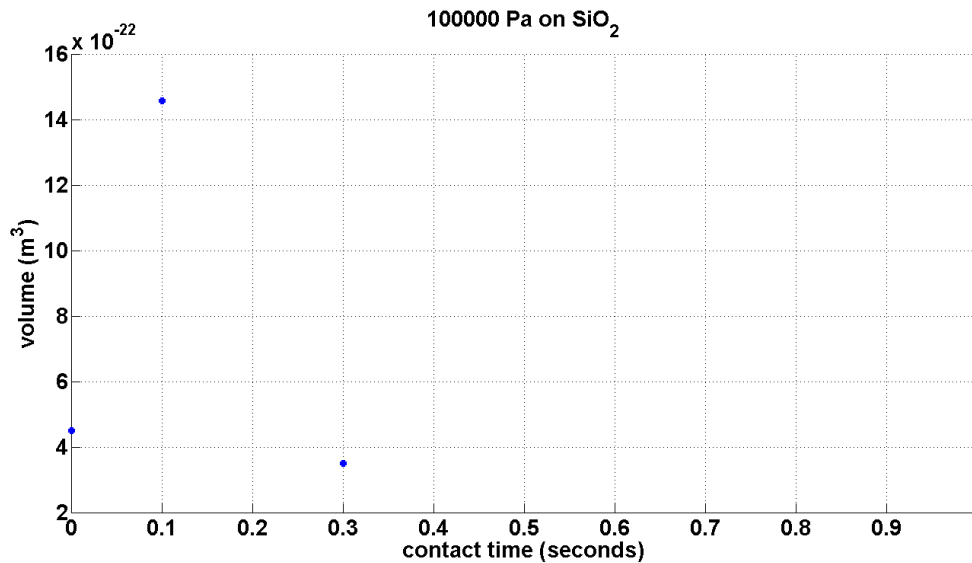


Figure 3-30: Provide pressure 1×10^5 Pa on SiO_2 from 0 s to 1 s.

Then the pressure is increased to 1.5×10^5 Pa, and the result is shown in 3-31. From the figure, it can be seen that the volume first increases and at 0.4 s there is burst of volume. Here the burst means that the volume suddenly increases a lot and the break-up position in the deflection curve graph can not be obtained because of the limitation of the piezoelectric z-stage. The burst of volume is expressed as the purple triangular in the figure. An example of the burst volume is shown in Figure 3-32. Because the maximum of the break-up distance that can be obtained from deflection curve is 9000 nm, the maximum volume can be measured in theory is about 100 fL. The volume of the burst in Figure 3-32 is about 10^4 fl, which is much larger than 100 fL. Decrease the pressure to 1.2×10^5 Pa, the result is shown in Figure 3-33. The volume first increases significantly and then almost keep constant, but at the 0.5 s, burst also happens. Then try 1.2×10^5 Pa on functionalized silicon surface. The functionalized silicon is made by putting silicon in a closed container full with octyltrichlorosilane vapor for 4 min. The contact angle of functionalized silicon is 98° and the receding contact angle is 80° . The result is shown in Figure 3-34. From the three different experiments, burst always happens. In two of the three experiments, the volume increases before the burst. But another first increases and then decreases. The experiment showing decreasing may be caused by dirty on the substrate or liquid remained on the tip. The result how the burst happens can be explained by Figure 3-35. Before the burst happens, because the aperture is at the side of the tip, when the pressure is applied, spherical cap shape liquid hangs at the aperture of the tip,

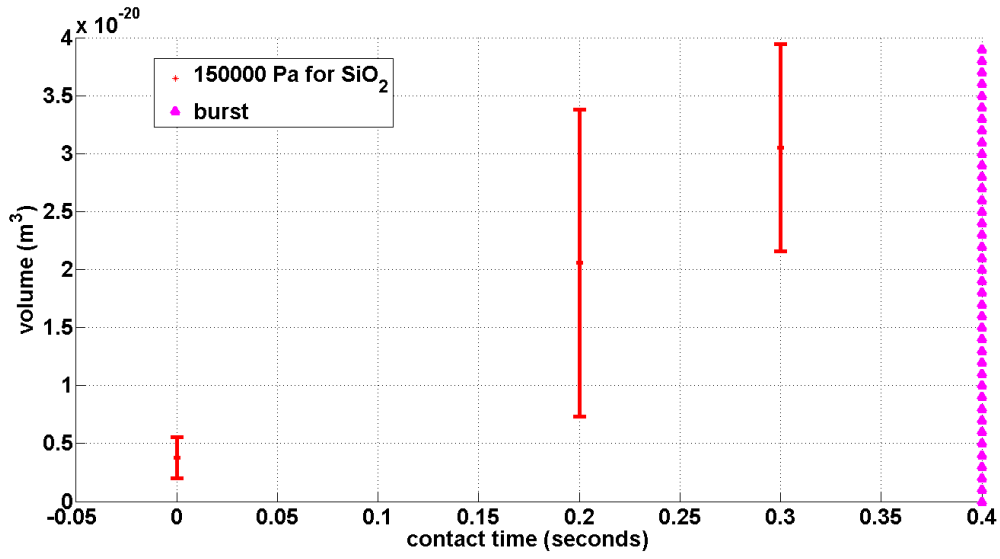


Figure 3-31: Provide pressure 1.5×10^5 Pa on SiO_2 .

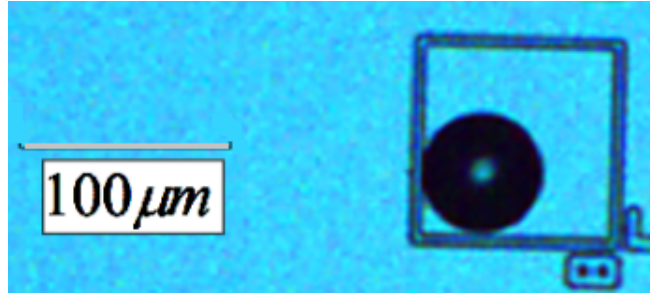


Figure 3-32: Example of burst.

the large positive pressure inside the spherical cap liquid counteracts the pressure provided outside as shown in Figure 3-35(a). This small spherical cap liquid increases the humidity around the area, then increases the vapor condensation. When the tip touches the substrate, the increased humidity forms an increased liquid bridge as shown in Figure 3-35(b). When the liquid bridge is large enough (touch the aperture), the liquid bridge and the spherical cap liquid become an unity, then the large positive pressure from the spherical cap becomes much smaller. The large pressure applied outside make the burst happen as shown in Figure 3-35(c).

According to Kelvin equation, the curvature of the condensed liquid bridge is related to humidity [31]:

$$H = \frac{R_g T}{\gamma v} \ln \frac{P_v}{P_\infty} \quad (3-6)$$

where R_g (J/(mol · K)) is the gas constant, T (K) is the absolute temperature, v (mol/m³) is the molar volume, P_v is the vapor pressure and P_∞ is the saturated vapor pressure. The relative humidity RH is related to vapor pressure as [32]:

$$\frac{RH}{100} = \frac{P_v}{P_\infty} \quad (3-7)$$

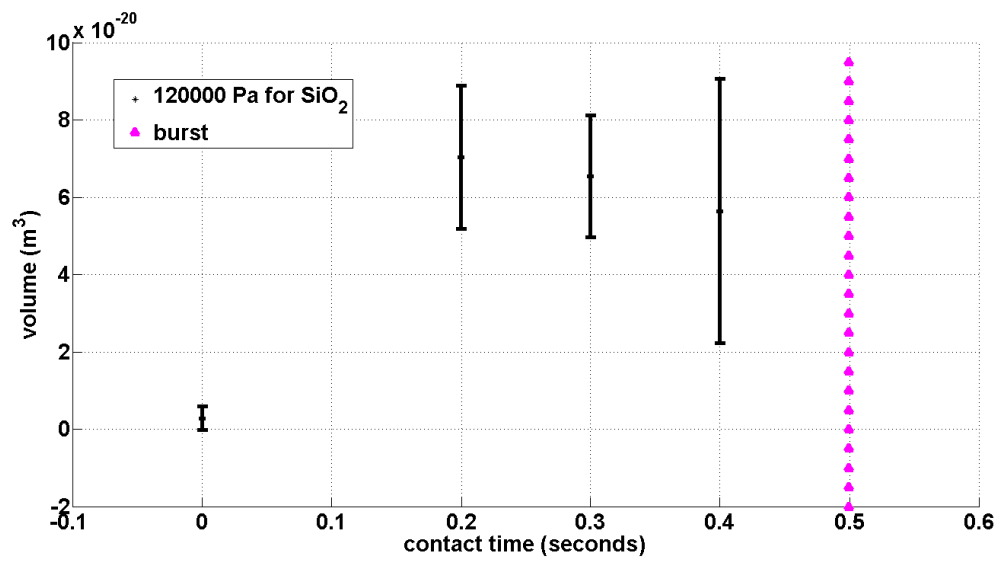


Figure 3-33: Provide pressure $1.2 \times 10^5 \text{ Pa}$ on SiO_2 .

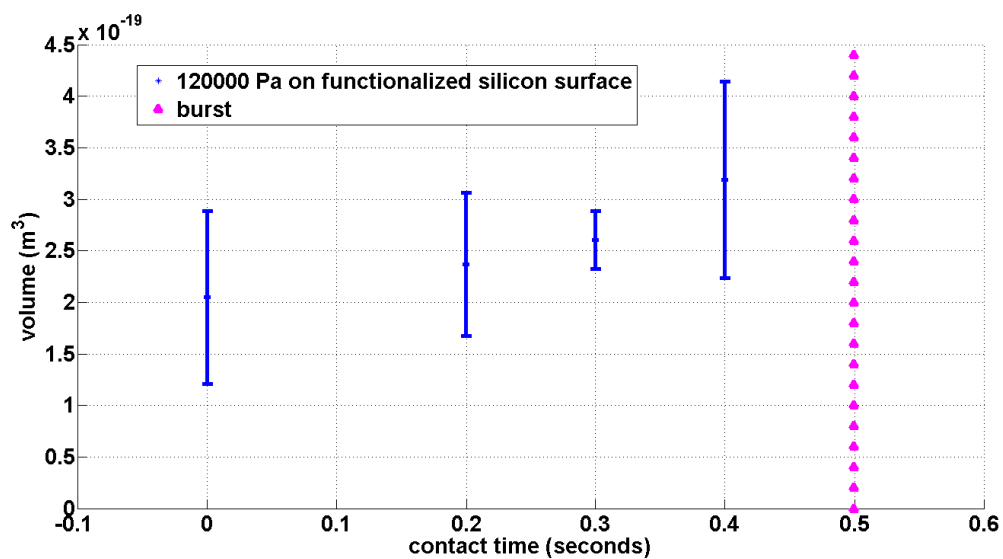


Figure 3-34: Provide pressure $1.2 \times 10^5 \text{ Pa}$ on functionalized silicon surface.

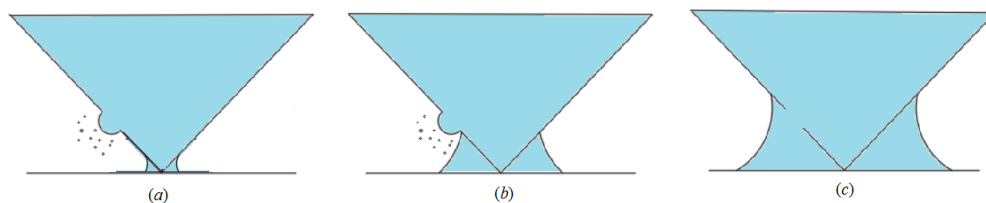


Figure 3-35: Explain how burst happens.

For $\theta_1 = 30^\circ$, $\theta_2 = 25^\circ$ and $\psi = 57^\circ$, the height of the connecting point between the condensed liquid bridge and pyramid tip for different humidity is shown in Table 3-1.

Table 3-1: The height of the liquid bridge for different humidity.

Humidity	10%	20%	30%	40%	50%	60%
Height	39.04nm	55.86nm	74.67nm	98.11nm	129.7nm	176nm

So if the aperture is 150 nm away from the top of the tip, it means when the humidity is between 40% and 50% that the condensed liquid bridge can touch the aperture. From the hydraulic resistance formula, the size of the aperture is $1000 \text{ nm} \times 250 \text{ nm}$, the thickness of the tip is about 600 nm. The hydraulic resistance is $4.86 \cdot 10^{18} \text{ Pa} \cdot \text{s}/\text{m}^3$. The length of hollow cantilever is $170 \mu\text{m}$, width is $30 \mu\text{m}$ and height is $10 \mu\text{m}$. The hydraulic resistance is $6.18 \cdot 10^{17} \text{ Pa} \cdot \text{s}/\text{m}^3$. So if provide $1.2 \times 10^5 \text{ Pa}$ for 0.1s, the volume of liquid goes out from aperture is $2.74 \cdot 10^3 \text{ fL}$, which shows burst. From Figure 3-36, providing no pressure and increasing the contact time from 1 s to 6 s, it shows that because of contamination, some liquid remains on the tip, and the volume keeps constant. After the experiment, provide $1 \times 10^5 \text{ Pa}$ for 0.3s, the burst happens. In the first experiment, even if provide $1 \times 10^5 \text{ Pa}$ for 1 s, there is no burst. It can verify that when the liquid bridge is large enough to touch the aperture, then burst can happen. It can be predicted that when the liquid bridge touches

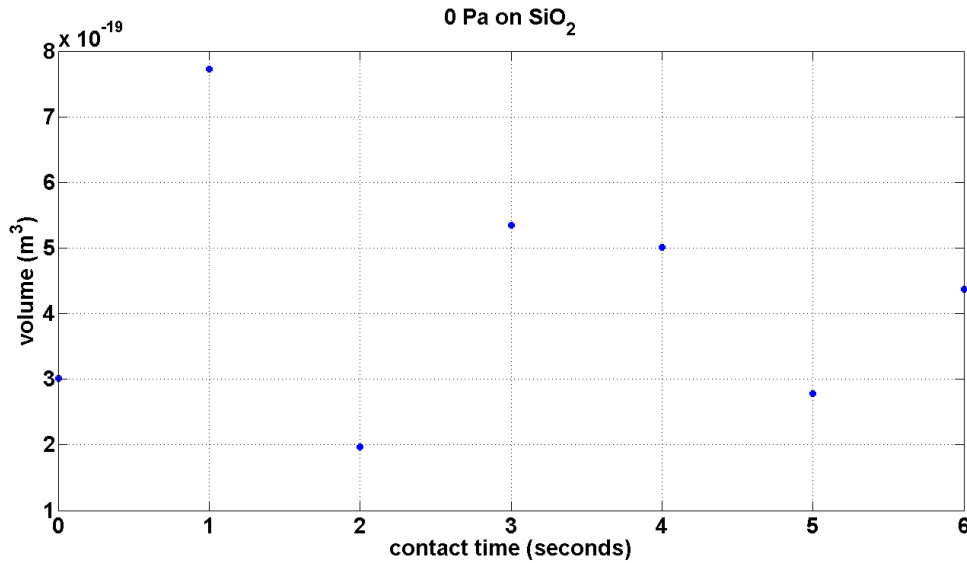


Figure 3-36: Provide no pressure on SiO_2 after several bursts.

the aperture, provide small pressure and use hollow cantilever with small aperture size, the volume could be measured, this is verified in Figure 3-37. It provides small pressure for 0.5s on functionalized silicon surface whose contact angle is 50.5° [2]. The relation between pressure and volume is linear. The VAF of the linear model and experimental data is 90.53%. The R_H obtained from the experiment data is $1.8382 \times 10^{22} \text{ Pa} \cdot \text{s}/\text{m}^3$. It should be noticed that the aperture size of this hollow cantilever is smaller than the hollow cantilever used in the previous experiments, which increases the hydraulic resistance. It can concluded that for

functionalized surface, the influence of Laplace pressure is small, the flow rate is linear with the pressure applied externally.

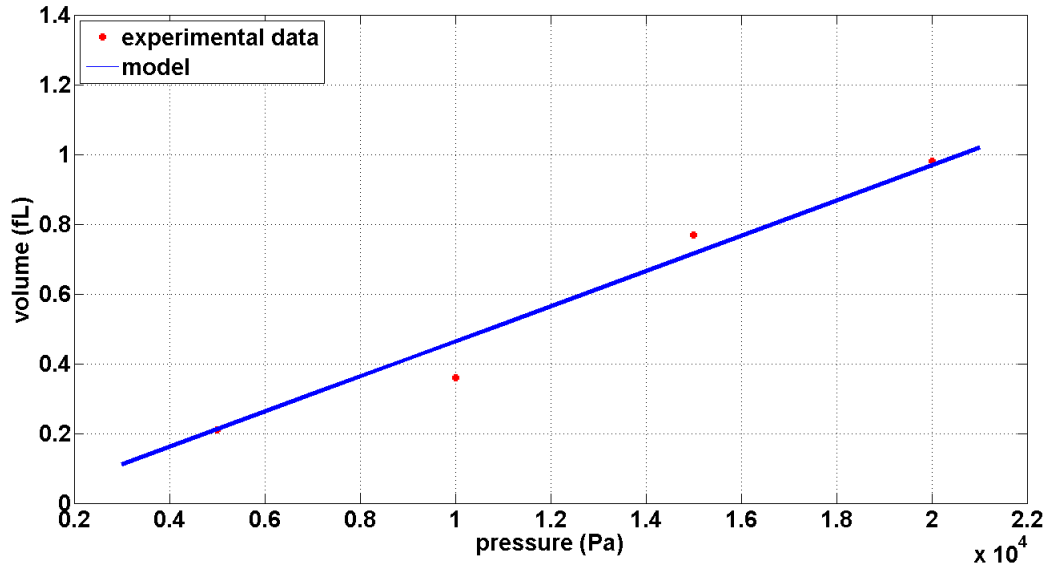


Figure 3-37: Provide different pressure on functionalized silicon surface for 0.5 s.

3-3-4 Dispensing on hydrophilic surface

When dose water with 5% glycerol on bare silicon, whose contact angle is 32°. Because the substrate is more hydrophilic, the absolute value of the negative Laplace pressure is too large, the flow rate is very large even do not provide pressure externally. Therefore, the volume is too large to be measured by using deflection curve. To measure the volume, the video of the volume increase process is recorded. Take the width of the cantilever as reference, and obtain the ratio of the radius between the liquid bridge and cantilever width as ra :

$$ra = \frac{w_2}{w_1} \quad (3-8)$$

where w_2 is the diameter of the liquid bridge and w_1 is the width of cantilever, which is shown in Figure 3-38. The volume of the liquid bridge is proportional to the cubic of radius, so ra^3 can reflect volume changing.

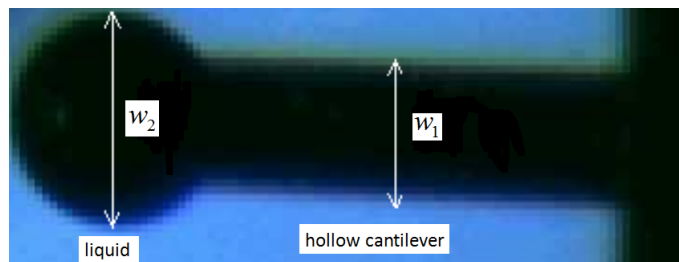


Figure 3-38: The schematic of ratio.

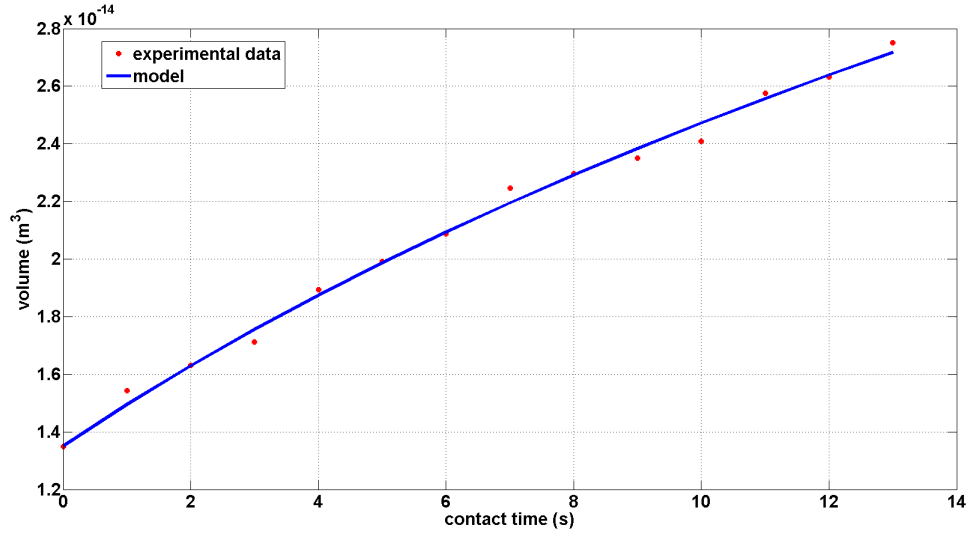


Figure 3-39: The result of dosing liquid on bare silicon for small tip-substrate distance.

In the first experiment, stop the tip after it touches the substrate very fast, which means that the distance between the tip and substrate is small. The contact time is from 1 s to 14 s (the 0 s means the beginning of the video). The droplet after dispensing is shown in Figure 3-41, whose diameter is $78 \mu\text{m}$. So the volume is $2.75 \times 10^{-14} \text{ m}^3$. Because the evaporation rate is proportional to the radius of the liquid bridge [33]. Compared to experiments on functionalized surface when the volume can be measured by deflection curve, the radius is much larger, so evaporation rate can not be neglected here. Then the model (2-13) becomes:

$$\frac{dV}{dt} = \frac{\Delta P_p - \gamma c_1 \sqrt[3]{\frac{c_2}{V}}}{R_H} - c_3 \sqrt[3]{V} \quad (3-9)$$

where c_3 is related to evaporation rate. The result of the experimental data and the simulation result by using model (3-9) to fit the data are shown in Figure 3-39. After tip touches the substrate, the tip retracts from the substrate automatically. Wait for a period then stop the device, which means there is large distance between the tip and substrate. The result is shown in Figure 3-40. The droplet remains on the substrate after breaking is shown in Figure 3-42, the diameter of the droplet is $69 \mu\text{m}$, the volume is $1.9 \times 10^{-14} \text{ m}^3$. From the two figures, it shows that the model (3-9) can match the data very well, and VAF is 98.54% and 97.46% for the two experiments. The value of parameter $\frac{\gamma c_1 \sqrt[3]{c_2}}{R_H}$ obtained in the first experiment is $-0.2647 \times 10^{-18.667} \text{ m}^4/\text{s}$ and c_3 is $0.0806 \times 10^{-9.33} \text{ m}^2/\text{s}$. For the second experiment, $\frac{\gamma c_1 \sqrt[3]{c_2}}{R_H}$ is $-0.2499 \times 10^{-18.667} \text{ m}^4/\text{s}$ and c_3 is $0.1644 \times 10^{-9.33} \text{ m}^2/\text{s}$.

In the second experiment the contact time is much longer than the first one, but the volume is smaller. This is because in Figure 2-15, $c_1 \sqrt[3]{c_2}$ becomes smaller when d increases in equation (2-8), which is related to the separate distance between the tip and substrate. So in model (3-9), the drag force from negative Laplace pressure becomes smaller. And the interface area between liquid and vapor increases at certain liquid volume when the distance between the tip and substrate becomes larger, which increases c_3 .

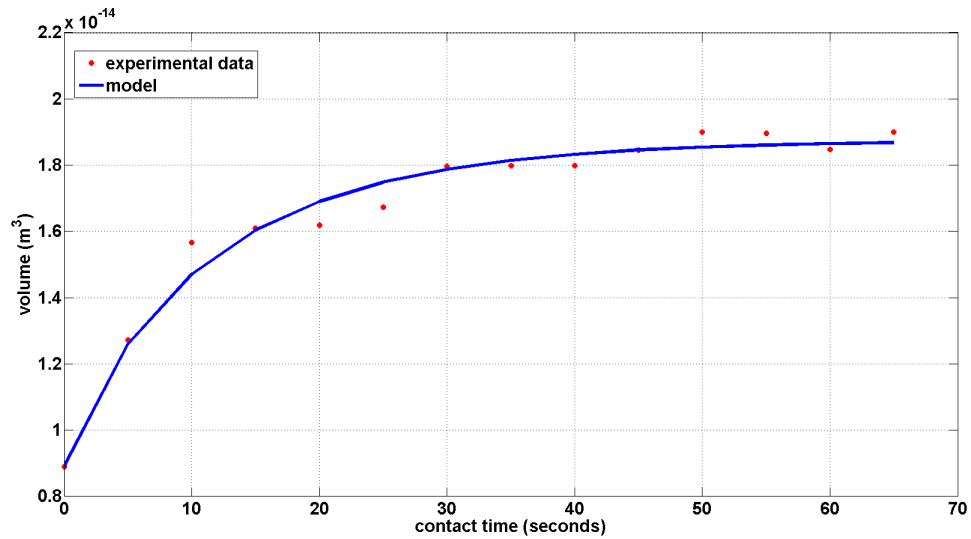


Figure 3-40: The result of dosing liquid on bare silicon for large tip-substrate distance.

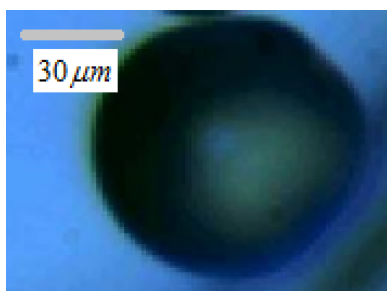


Figure 3-41: The droplet remains on the substrate when the distance between the tip and substrate is small.

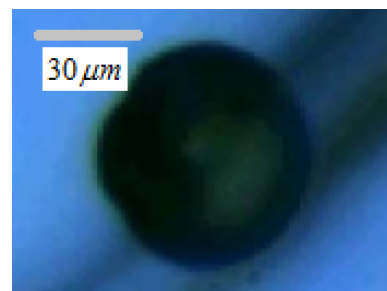


Figure 3-42: The droplet remains on the substrate when the distance between the tip and substrate is large.

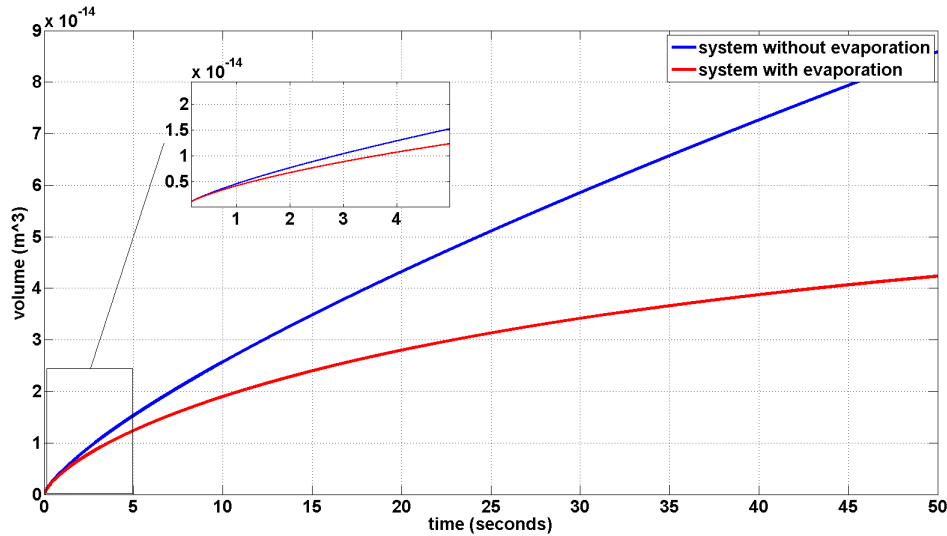


Figure 3-43: Compare the result of the model with evaporation (3-9) and without evaporation (2-13).

Use the parameters obtained in the first experiment, and assume the hydraulic resistance is $1 \times 10^{18} \text{ Pa} \cdot \text{s}/\text{m}^3$, the initial volume is $2 \times 10^{-19} \text{ m}^3$, no pressure is applied externally. The result of the model with evaporation (3-9) and model without evaporation (2-13) is shown in Figure 3-43. The figure shows that by using this small hydraulic resistance, volume will suddenly increase to the large value that can not be measured by AFM deflection curve after the tip touches the substrate. The difference of the models becomes larger when the volume increases. When the volume is very small in the scale 10^{-15} m^3 , the difference between the model with evaporation and the model without evaporation can be neglected. But it should be noticed that when the hydraulic resistance becomes larger, the difference between two models will become larger even in small volume.

3-4 Conclusion

For nano-litre volume experiments, performed by a precision hollow stainless steel tip, the Laplace pressure derived from the liquid bridge shape influences the dispensing process as expected. For pico to femto litre volume experiments—with hollow cantilevers, the resulting model describing the Laplace pressure inside the liquid bridge is given by equation (3-9). The developed model for the dosing process was validated with the experimental data with variance accounted for (VAF) larger than 90%. The model was able to describe the dosing process on different substrates.

Chapter 4

Controllers

4-1 Introduction

In this chapter, controllers have been designed according to the dosing process model of hollow cantilever. If the hydraulic resistance of the hollow cantilever is too small, the volume of the liquid bridge will become too large to be measured by AFM deflection curve even no external pressure is applied. The proper choice of the hydraulic resistance should be larger than $1 \times 10^{20} \text{ Pa} \cdot \text{s}/\text{m}^3$. According to Figure 3-37, when the volume is small, the evaporation rate can be ignored. So the controllers are designed by using the model (2-13). In the section 1, pre-operation before applying and designing controllers is introduced. In the section 2, series PID controller and parallel PI controller are designed by linearizing the system. Because of non-linearity of the model, the phenomenon is not ideal. So a controller by combing feedback-linearization and iterative learning controller is designed to deal with the nonlinear part. Finally model reference adaptive control is designed, which does not need to identify the system. The goal of the controllers is to decrease the settle time (decrease the number of contact) with less overshoot.

4-2 Pre-action before controlling

4-2-1 Humidity Control

We choose model (2-13) to design controllers when the volume of liquid is small. According to the chapter 3, if the liquid bridge does not touch the aperture, burst of the liquids is unavoidable, the process is uncontrollable. So before applying controllers, the liquid bridge should be guaranteed large enough to touch the aperture. With humidity in environment increasing, the liquid bridge will increase. Therefore, before providing pressure to control the volume, a suitable humidity should be obtained. Thanks to the humidity control system, it is possible to change the local humidity around the place where hollow cantilever works. The flow chart of humidity operation is shown in Figure 4-1. First provide low humidity about 10%

and at the same time provide small pressure $2 \times 10^3 \text{ Pa}$ for 0.5 s. If there is significant volume increase, such as when the hydraulic resistance is $1 \times 10^{20} \text{ Pa} \cdot \text{s}/\text{m}^3$, the increase of volume is 10 fL, this means the liquid bridge has already touched the aperture. Keep this humidity to identify the system and implement controllers. If there is not significant volume increase, increase the humidity by 10% and repeat the process until significant volume increase has been detected.

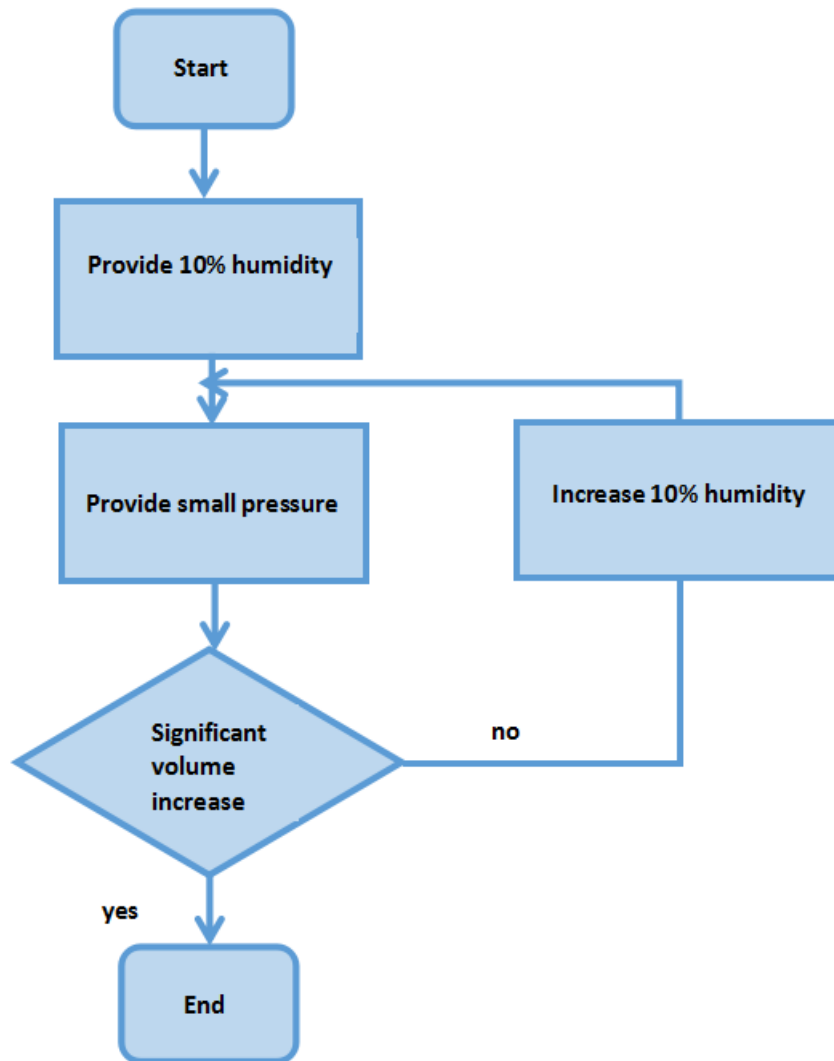


Figure 4-1: Flow chart of humidity control.

4-2-2 System Identification

To design controllers, we need to know the parameters of the model. The identification method here used is least square method, which has good estimation performance and high

modeling efficiency [34]. For a single input-output nonlinear model:

$$\begin{aligned}\dot{X} &= f(X, \theta, u) \\ y &= F(X)\end{aligned}\quad (4-1)$$

where X is the state vector of the model, u is the input of the model, θ is the parameter vector of the model, y is the output of the model. The parameter identification is to make the input-output relation of the model closely to the real system by choosing proper parameters. In the least square method, this is done by minimizing the sum of the squared difference between output of the model and real output by choosing the best θ :

$$\min \sum_{k=1}^n (y_r(k) - y(k))^2 \quad (4-2)$$

where $y_r(k)$ is the actual output of system, $y(k)$ is the output of the model.

Because the existing hollow cantilever has too small hydraulic resistance, the volume of liquids is too large to be measured by AFM deflection force curve. Just use the model whose $R_H = 1 \times 10^{20} \text{ Pa} \cdot \text{s}/\text{m}^3$, $\gamma c_1 \sqrt[3]{c_2} = -40.4622 \times 10^{-3}$ with output variance 0.2 fL as the real system to show the least square method is feasible. When provide -20000 Pa for 1 s with contact time 0.1 s, the result of the system identification is shown in Figure 4-2.

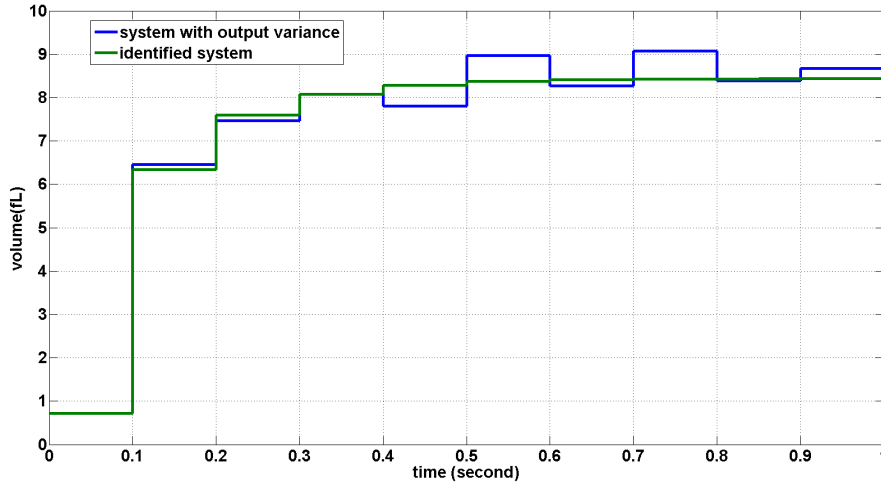


Figure 4-2: The result of system identification.

The estimated parameters are: $R_H = 0.97 \cdot 10^{20} \text{ Pa} \cdot \text{s}/\text{m}^3$, $\gamma c_1 \sqrt[3]{c_2} = -40.78 \cdot 10^{-3}$. The order of the estimated parameters are the same with the actual system. With the variance of the output increasing, the error between the estimated parameters and actual parameters will increase.

4-3 PID controller

In the industry, PID controllers are the most common control methodology to use in real applications [35]. So here first use PID control to control the system. In [36][37], several

methods are introduced to tune PID controller. Because the model of the system is known and the parameters of the system can be identified, here design the PID controller in frequency domain. Because series PID controller is easier to design than parallel PID controller [37] in frequency domain, so the former is selected. An easy-to-tune series PID controller is:

$$C(s) = C_0 \left(1 + \frac{\omega_I}{s}\right) \left(\frac{1 + s/\omega_1}{1 + s/\omega_2}\right)^{N_D} \left(\frac{1}{1 + s/\omega_F}\right) \quad (4-3)$$

Each term of the series PID controller is band-limited and a filter is introduced. The bode plot of $C(s)$ is shown in Figure 4-3. According to the bode plot, it is seen the influence of different parts of the controller in different frequency range:

- an integrator for $\omega \in [0, \omega_I]$
- a proportional gain for $\omega \in [\omega_I, \omega_1]$
- a differentiator for $\omega \in [\omega_1, \omega_2]$
- an amplifier for $\omega \in [\omega_2, \omega_F]$
- a low-pass filter for $\omega \in [\omega_F, \infty]$

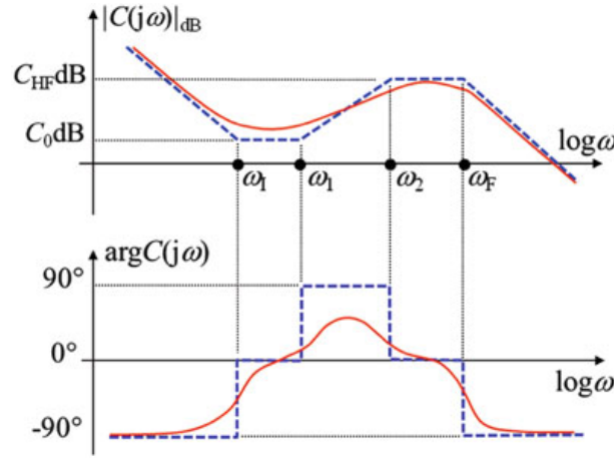


Figure 4-3: Frequency response of a series PID(F) controller when $N_D = 1$ [37].

For a desired phase margin M_ϕ and open loop gain crossover frequency ω_{cg} , there is a straight forward way to tune the parameters of the controller. By make $\frac{\omega_{cg}}{\omega_I} = \frac{\omega_F}{\omega_{cg}}$, the phase of the controller $\arg C(j\omega_{cg})$:

$$\arg C(j\omega_{cg}) = \phi_M - 2 \arctan \frac{\omega_{cg}}{\omega_F} \quad (4-4)$$

where ϕ_M is the lead or lag phase provided by the derivative part of the controller. For the required phase margin M_ϕ , it should be:

$$\phi_M = -\pi + M_\phi - \arg G(j\omega) + 2 \arctan \frac{\omega_{cg}}{\omega_F} \quad (4-5)$$

Where $G(j\omega)$ is the frequency response of the plant. When the ratio between ω_{cg} and ω_I (or between ω_F and ω_{cg}) is chosen close to 1, the influence of integrator and filter will increase.

For $\frac{\omega_{cg}}{\omega_I} = \frac{\omega_2}{\omega_{cg}}$, then we can get:

$$\frac{\omega_2}{\omega_{cg}} = \tan \frac{\frac{\phi_M}{N_D} + \frac{\pi}{2}}{2} \text{ or } \frac{\omega_2}{\omega_{cg}} = \sqrt{\frac{1 + \sin\left(\frac{\phi_M}{N_D}\right)}{1 - \sin\left(\frac{\phi_M}{N_D}\right)}} \quad (4-6)$$

Because at the open loop cross-over frequency we have:

$$|C(j\omega_{cg})| = \frac{1}{|G(j\omega_{cg})|} \quad (4-7)$$

Then the proportional gain C_0 is obtained:

$$C_0 = \frac{1}{\left(\frac{\omega_2}{\omega_{cg}}\right)^{N_D} |G(j\omega_{cg})|} \quad (4-8)$$

To design the series PID controller, the linearized model is required. For model (2-13), an equilibrium point is needed to find to linearize the system [38]. The equilibrium point is the at the point where $\frac{dV}{dt} = 0$, and the point is related to the desired output V_d . The input is the provided pressure, which is ΔP_p . The equilibrium point $(V_e, \Delta P_{pe})$ is $(V_d, \frac{\gamma c_1 \sqrt[3]{c_2}}{\sqrt[3]{V_d}})$, the linearized system can be treated as:

$$\frac{d(\delta V)}{dt} = \frac{1}{R_H} \delta \Delta P_p + \frac{1}{3R_H} \gamma c_1 \sqrt[3]{c_2} \frac{1}{4\sqrt[3]{V_d}} \delta V \quad (4-9)$$

where $\delta V = V - V_e$ and $\delta \Delta P_p = \Delta P_p - \Delta P_{pe}$. Treat δV as y and $\delta \Delta P_p$ as u , so the linearized system is:

$$\frac{dy}{dt} = \frac{1}{R_H} u + \frac{1}{3R_H} \gamma c_1 \sqrt[3]{c_2} \frac{1}{4\sqrt[3]{V_d}} y \quad (4-10)$$

The transfer function of the linearized system is:

$$\frac{Y(s)}{U(s)} = \frac{1}{R_H s - \frac{1}{3} \gamma c_1 \sqrt[3]{c_2} \frac{1}{4\sqrt[3]{V_d}}} \quad (4-11)$$

Here the contact time is chosen as 0.01 s. The parameters of the model is: $R_H = 10^{20} \text{ Pa} \times \text{s/m}^3$ and $\gamma c_1 \sqrt[3]{c_2} = -0.0405 \text{ N/m}$. The controller is designed by choosing $N_D = 1$, $\frac{\omega_{cg}}{\omega_f} = 0.1$, $\omega_{cg} = 80 \text{ rad/s}$ and $M_\phi = 150^\circ$. Because of the contact time, the system has delay 0.01 s. The delay with time T_s in the transfer function is presented as *Padé approximation* [39]:

$$e^{T_s} \approx \frac{1 - \frac{T_s}{2}}{1 + \frac{T_s}{2}} \quad (4-12)$$

The bode plot of the open system is shown in Figure 4-4. The bode plot of the closed system is shown in Figure 4-5, and the step response of the linearized system is shown in Figure 4-6. The simulation result of the nonlinear system is shown in Figure 4-7. From the figures,

compared to the system without delay, the open loop of delayed system has smaller phase margin, the difference is 45° . And because of magnitude of the series PID controller around the crossover frequency increases with frequency increasing, the controlled open loop system has slower magnitude decrease around the cross over frequency (even increase). Comparing to those controlled system that has fast decrease around the cross over frequency, before the crossover frequency, the magnitude of bode plot of the controlled close loop system is smaller, after the crossover frequency, the magnitude of the closed loop bode plot is larger. This leads to good damp (no overshoot), larger settling time and increase fast at the beginning in the step response for the system without delay. And because of the larger decreasing of phase brought in by the delay after the crossover frequency, there is a peak of the magnitude in the closed loop bode plot, this leads to the oscillation in the step response for system with delay. When decrease the phase margin of the open system, the ratio $\frac{\omega_2}{\omega_{cg}}$ becomes smaller, the influence of the magnitude increase of the controller becomes smaller, so the damp becomes smaller, the linear system responds quicker. Because the nonlinearity of the nonlinear system, the overshoot of the simulation result of the nonlinear system becomes larger. Decrease the ratio $\frac{\omega_{cg}}{\omega_f}$, similar with decrease the phase margin, the linear system will respond quicker. But it will be slow to solve the error brought in by the nonlinearity when control the nonlinear system.

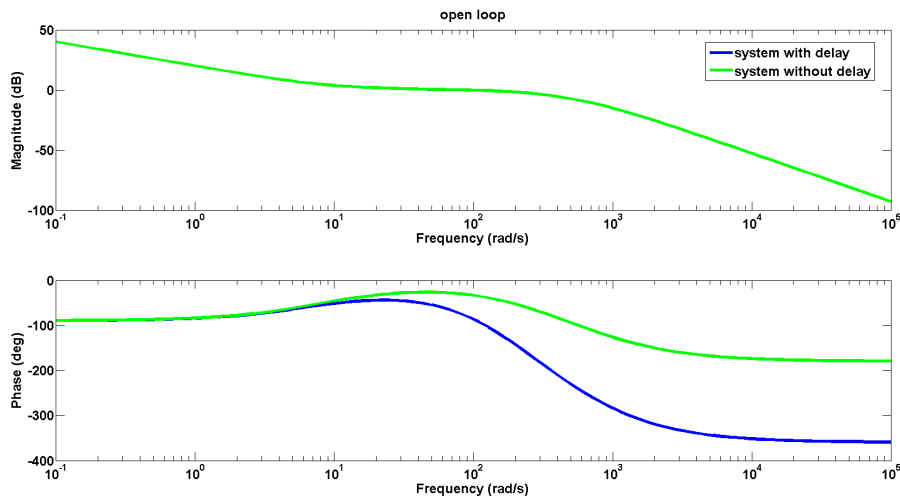


Figure 4-4: Bode plot of the open system by using series PID controller.

Even though the series PID controller can change the crossover frequency and phase margin of the open system as expected, the increase magnitude of the controller around the crossover frequency, which brings in large peak in the magnitude of the closed loop bode plot after crossover frequency and reduce the magnitude before the crossover frequency of the delayed system. This will bring in oscillation and slow response. A more simple controller, parallel PI controller:

$$C(s) = K_p + K_i \frac{1}{s} \quad (4-13)$$

It does not increase magnitude. Because this controller can not tune the phase arbitrarily like series PID controller and the phase of the controller changes from -90 to 0 around

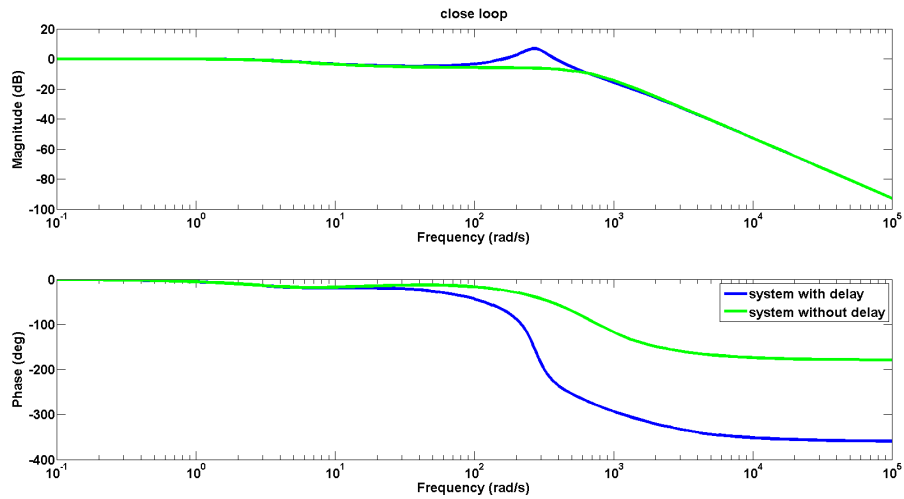


Figure 4-5: Bode plot of the closed system by using series PID controller.

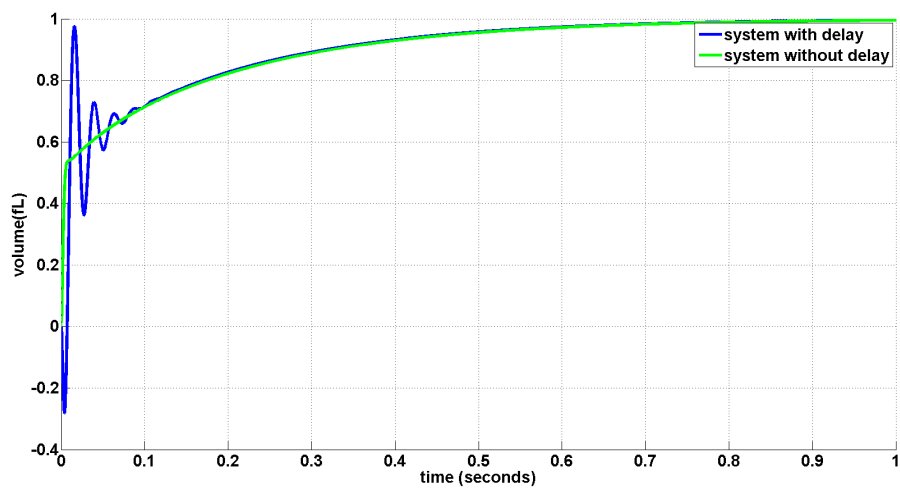


Figure 4-6: The step response of the linearized system with delay and without delay by using series PID controller.

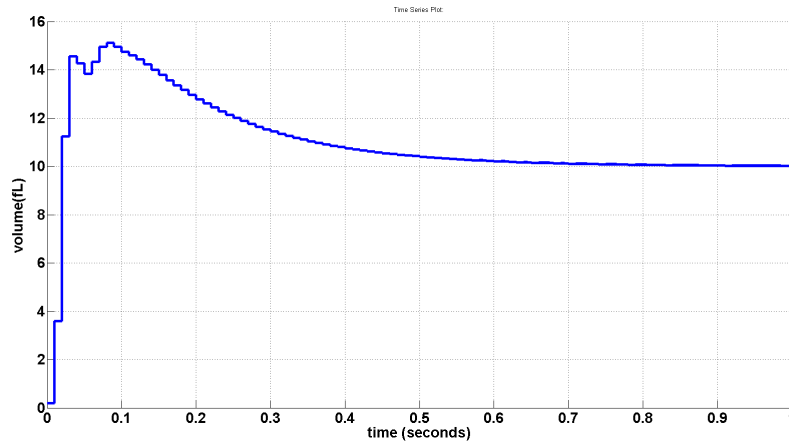


Figure 4-7: Simulation result of the controlled nonlinear system by using series PID controller.

$\omega = \frac{K_i}{K_p}$ rad/s. To make sure the delayed system is stable, $\frac{K_i}{K_p}$ is chosen as 10 (the phase is larger than -180 at the cross over frequency). The crossover frequency chosen is 80 rad/s. The parameters of the controller obtained are $K_p = 8.09 \times 10^3$, $K_i = 8.09 \times 10^4$, the bode plot of the open system with delay is shown in Figure 4-8, the closed system with delay is shown in Figure 4-9. From the figures the problems existing in the series PID controller has been solved, the magnitude before the crossover frequency has increased and the peak of the close system decreases. The simulation result of the PI controlled nonlinear system is shown in Figure 4-10. The overshoot and settling time are both smaller than series PID controller. And from the above analysis, the delay in the system influences a lot to the series PID and parallel PI controller. Also, the nonlinearity of the system makes the two controllers perform worse.

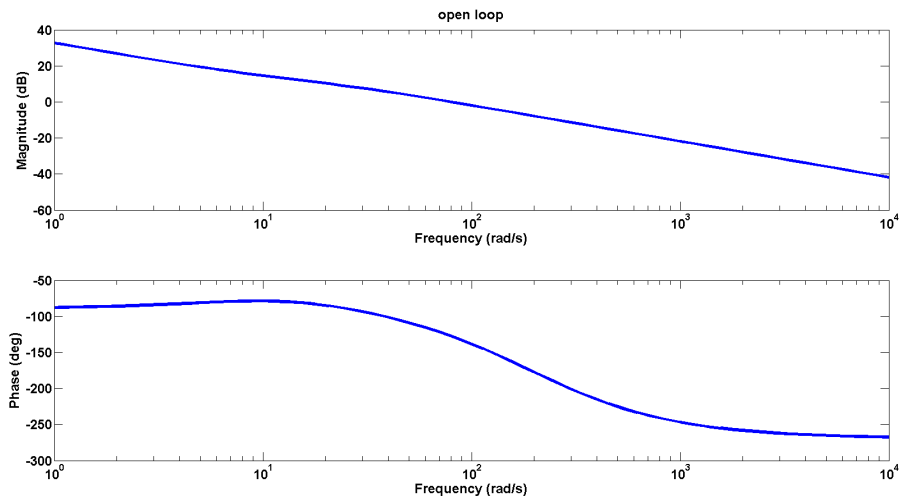


Figure 4-8: Bode plot of the open system by using parallel PI controller.

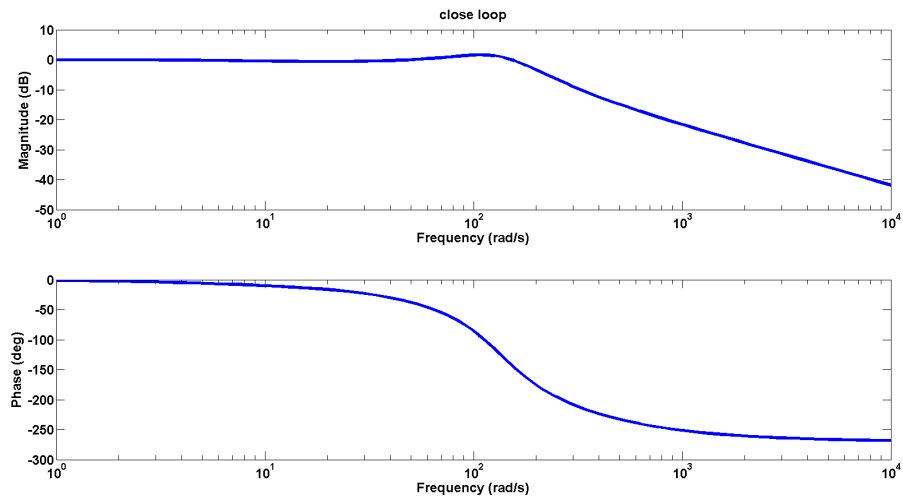


Figure 4-9: Bode plot of the closed system by using parallel PI controller.

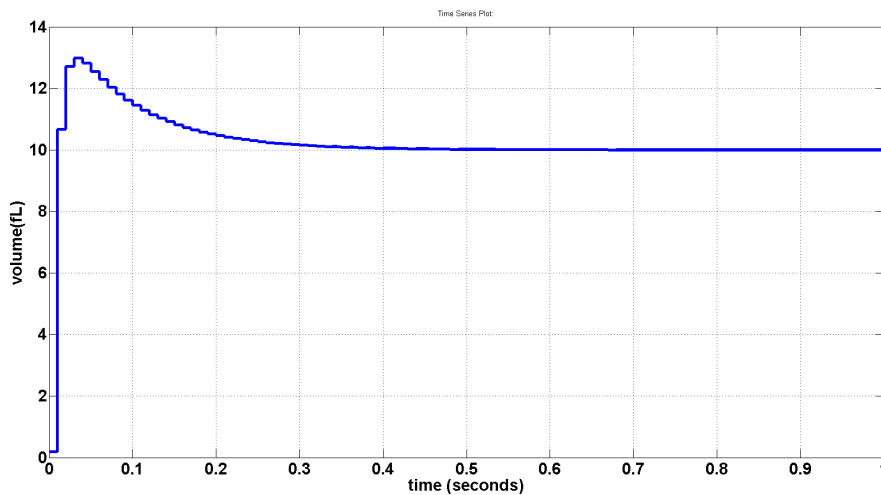


Figure 4-10: Simulation result of the nonlinear system by using parallel PI controller.

4-4 Feedback Linearization and Iterative Learning Control

4-4-1 Feedback Linearization

From last section, the nonlinearity of the model (2-13) influences the response of series PID controller and parallel PI controller. The most convenient way to cancel the nonlinearity of the system is feedback linearization [40]. Because of the simple structure of the model, the nonlinear part is just the Laplace pressure from the liquid bridge $\frac{c_1 \gamma \sqrt[3]{c_2}}{\sqrt[3]{V}}$. For the simplicity of present, the input ΔP_p is presented as u , and the output V is presented as y . So if provide



Figure 4-11: Simulation result of the nonlinear system by using feedback linearization with contact time 0.01 s.

the input pressure:

$$u = -\zeta R_H y + \zeta R_H u_{ref} + \frac{c_1 \gamma \sqrt[3]{c_2}}{\sqrt[3]{y}} \quad (4-14)$$

where u_{ref} (reference) is the desired output. Then the system becomes:

$$\frac{dy}{dt} = -\zeta y + \zeta u_{ref} \quad (4-15)$$

whose transfer function is:

$$f(s) = \frac{\zeta}{s + \zeta} \quad (4-16)$$

When the linearized system has delay, the transfer function becomes:

$$f(s) = \frac{\zeta}{s + \zeta \left(\frac{1 - \frac{T_s}{2}}{1 + \frac{T_s}{2}} \right)} \quad (4-17)$$

To make the system stable, ζT should be smaller than 2. When the reference is step input, the time-domain response of the non-delay system is:

$$y = u_{ref} - C e^{-\zeta t} \quad (4-18)$$

where C is determined by the initial condition.

So if the parameter ζ increases, which means increase the bandwidth of the system, the system will become more fast. Because of the limitation of the sample frequency, the bandwidth can not be too large. When the hydraulic resistance is $R_H = 10^{20} \text{ Pa} \cdot \text{s}/\text{m}^3$, and the contact time is 0.01 s, ζ is chosen as 80. The simulation result of the feedback linearized system is shown in Figure 4-11.

For decreasing the influence of the disturbance caused by response time in the pressure control system. Increase the contact time to 0.1 s, and ζ is reduced to 15. The simulation result of

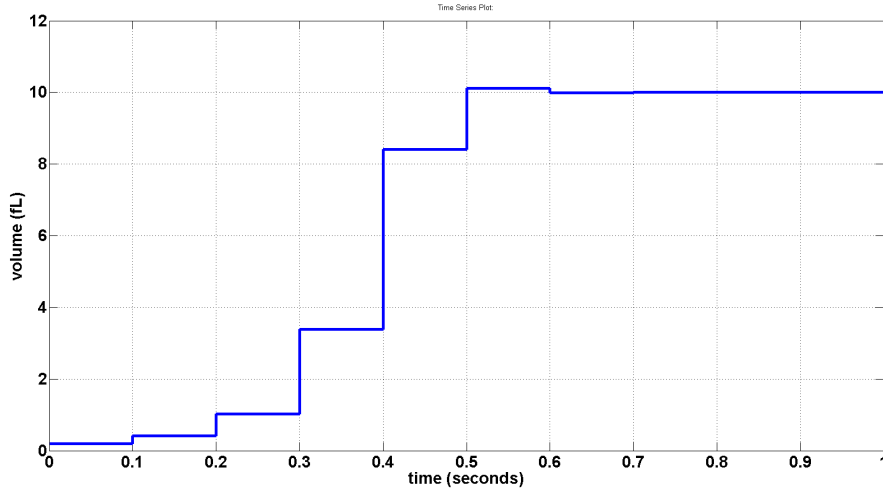


Figure 4-12: Simulation result of the system by using feedback linearization with contact time 0.1 s.

the feedback linearized system is shown in Figure 4-12. According to the figure, the system will be stable after contacting the substrate 6 times, which suits our demand. For feedback linearization, to cancel the nonlinear part of the system, the parameters of the system must be known. The parameters can be obtained by using identification method, but because of disturbance in the system, there must be uncertainty in the parameters. So assume the parameter $c_1\gamma\sqrt[3]{c_2}$ identified is $1/5$ of the real value of the system, the result of the performance of feedback linearization is shown in Figure 4-13. There is steady state error. For the model (2-13), treat $c_1\gamma\sqrt[3]{c_2}$ as a_1 , and the estimated value of it is a_2 , by using feedback linearization and input (4-14), the system becomes:

$$\dot{y} = \frac{-\zeta R_H y + \zeta R_H u_{ref} + (a_2 - a_1) \frac{1}{\sqrt[3]{y}}}{R_H} \quad (4-19)$$

which can be transformed as:

$$\dot{y} + \zeta y + \frac{a_1 - a_2}{R_H} \frac{1}{\sqrt[3]{y}} = \zeta u_{ref} \quad (4-20)$$

Use Taylor series approximation of the nonlinear part $\frac{1}{\sqrt[3]{y}}$ at the position u_{ref} :

$$\frac{1}{\sqrt[3]{y}} = \frac{1}{\sqrt[3]{u_{ref}}} - \frac{1}{3} u_{ref}^{-\frac{4}{3}} (y - u_{ref}) + O(y - u_{ref})^2 \quad (4-21)$$

So the (4-20) becomes:

$$\dot{y} + \zeta y + \frac{a_1 - a_2}{R_H} \left(\frac{1}{\sqrt[3]{u_{ref}}} - \frac{1}{3} u_{ref}^{-\frac{4}{3}} (y - u_{ref}) + O(y - u_{ref})^2 \right) = u_{ref} \quad (4-22)$$

a_1 and a_2 are negative value. If $|a_1| > |a_2|$ and assume $O(y - u_{ref})^2 = 0$, we can obtain:

$$\dot{y} + \zeta y + \frac{a_2 - a_1}{3R_H} u_{ref}^{-\frac{4}{3}} y = \frac{4(a_2 - a_1)}{3R_H} u_{ref}^{-\frac{1}{3}} + \zeta u_{ref} \quad (4-23)$$

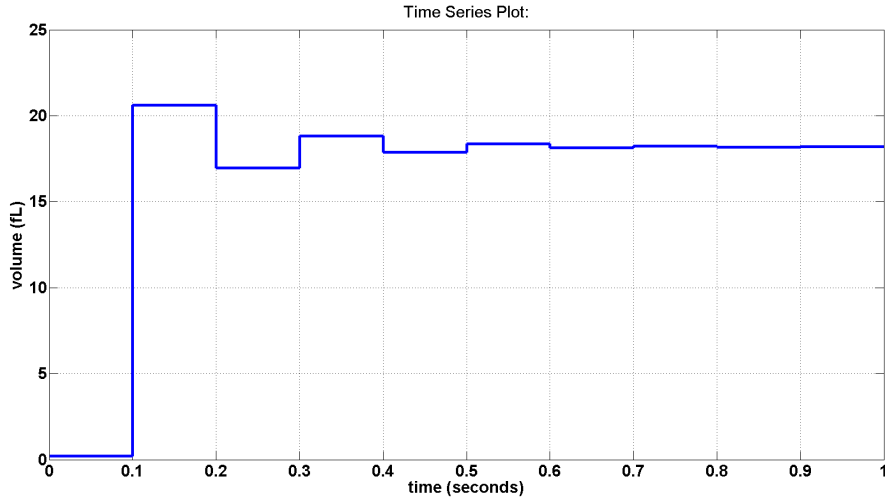


Figure 4-13: Simulation result of the nonlinear system by using feedback linearization with system uncertainty.

Because $a_2 - a_1 > 0$, so (4-23) is stable. And the steady value y_{final} becomes:

$$y_{final} = \frac{\frac{4(a_2 - a_1)}{3R_H} u_{ref}^{-\frac{1}{3}} + \zeta u_{ref}}{\zeta + \frac{a_2 - a_1}{3R_H} u_{ref}^{-\frac{4}{3}}} \quad (4-24)$$

The value is different from u_{ref} .

To deal with the steady state error, the easiest way is to use integrator, but the working principle of integrator is to integrate the error between the output and reference. When the steady state error is positive, there will be overshoot. To solve the steady state error without overshoot, combination of feedback linearization and iterative learning control is designed.

4-4-2 Iterative Learning Control (ILC)

The objective of ILC is to improve performance by incorporating error information into the control for subsequent iterations when the system perform the same operation repeatedly and under the same operating condition. It can achieve good performance despite large model uncertainty [41]. The principle of ILC controller is shown in Figure 4-14. j means the iteration times which is in the subtitle in the following. And k means the time at the k th sample time, which is in the bracket in the following. The control signal comes from the calculation of control signal and error signal in the previous iteration. The error signal is from the difference between the output of the system and desired output. Here combine the iterative learning controller with feedback linearization to deal with the uncertainty of the system. The widely used A-type iterative learning controller is used here:

$$u_{j+1}(k) = q[u_j(k) + l e_j(k+1)] \quad (4-25)$$

It offers wider learning bandwidth than D-type, P-type and PD-type iterative learning controllers [42].

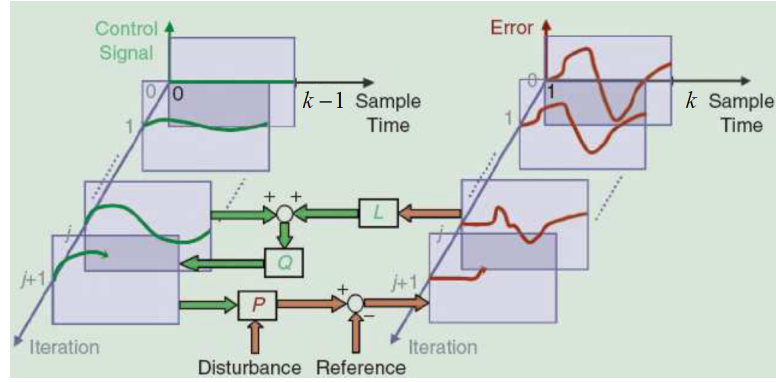


Figure 4-14: The schematic of ILC [41].

For (4-22), define $\zeta + \frac{a_2 - a_1}{3R_H} = p_1$, $\frac{4(a_2 - a_1)}{3R_H} u_{ref}^{-\frac{1}{3}} + \zeta u_{ref} + \frac{a_2 - a_1}{R_H} O(y(k) - u_{ref})^2 = b(k)$, $R_H u(k)$ is the input of the iterative controller, systems becomes:

$$\dot{y} = -p_1 y + b + u \quad (4-26)$$

where $p_1 > 0$ and $b > 0$. When the contact time is h_s , discretize system as:

$$y(k+1) = Ay(k) + Bb(k) + Bu(k), \quad k \text{ is integer} \quad (4-27)$$

where,

$$A = e^{-p_1 h_s}$$

$$B = \int_0^{h_s} e^{-p_1 \epsilon} d\epsilon$$

Then we can obtain:

$$\begin{bmatrix} y(1) \\ y(2) \\ \vdots \\ y(n-1) \\ y(n) \end{bmatrix} = \begin{bmatrix} B & 0 & \dots & \dots & 0 \\ AB & B & 0 & \dots & 0 \\ \vdots & \ddots & \ddots & \ddots & \vdots \\ A^{n-2}B & A^{n-3}B & \dots & B & 0 \\ A^{n-1}B & A^{n-2}B & \dots & AB & B \end{bmatrix} \begin{bmatrix} b(0) \\ b(1) \\ \vdots \\ b(n-2) \\ b(n-1) \end{bmatrix} + \begin{bmatrix} A \\ A^2 \\ \vdots \\ A^{n-1} \\ A^n \end{bmatrix} y(0) + \begin{bmatrix} B & 0 & \dots & \dots & 0 \\ AB & B & 0 & \dots & 0 \\ \vdots & \ddots & \ddots & \ddots & \vdots \\ A^{n-2}B & A^{n-3}B & \dots & B & 0 \\ A^{n-1}B & A^{n-2}B & \dots & AB & B \end{bmatrix} \begin{bmatrix} u(0) \\ u(1) \\ \vdots \\ u(n-2) \\ u(n-1) \end{bmatrix} \quad (4-28)$$

Define

$$\begin{bmatrix} y(1) \\ y(2) \\ \vdots \\ y(n-1) \\ y(n) \end{bmatrix} = Y$$

$$\begin{bmatrix} B & 0 & \dots & \dots & 0 \\ AB & B & 0 & \dots & 0 \\ \vdots & \ddots & \ddots & \ddots & \vdots \\ A^{n-2}B & A^{n-3}B & \dots & B & 0 \\ A^{n-1}B & A^{n-2}B & \dots & AB & B \end{bmatrix} = P$$

$$\begin{bmatrix} A \\ A^2 \\ \vdots \\ A^{n-1} \\ A^n \end{bmatrix} = m$$

$$\begin{bmatrix} u(0) \\ u(1) \\ \vdots \\ u(n-2) \\ u(n-1) \end{bmatrix} = U$$

$$P \begin{bmatrix} b(0) \\ b(1) \\ \vdots \\ b(n-2) \\ b(n-1) \end{bmatrix} + my(0) = D$$

Then (4-28) becomes:

$$Y = PU + D \quad (4-29)$$

By defining:

$$Q = \begin{bmatrix} q & 0 & \dots & \dots & 0 \\ 0 & q & 0 & \dots & 0 \\ \vdots & \ddots & \ddots & \ddots & \vdots \\ 0 & 0 & \dots & q & 0 \\ 0 & 0 & \dots & 0 & q \end{bmatrix} \quad (4-30)$$

$$L = \begin{bmatrix} l & 0 & \dots & \dots & 0 \\ 0 & l & 0 & \dots & 0 \\ \vdots & \ddots & \ddots & \ddots & \vdots \\ 0 & 0 & \dots & l & 0 \\ 0 & 0 & \dots & 0 & l \end{bmatrix} \quad (4-31)$$

$$E = \begin{bmatrix} u_{ref}(1) \\ u_{ref}(2) \\ \vdots \\ u_{ref}(n-1) \\ u_{ref}(n) \end{bmatrix} - \begin{bmatrix} y(1) \\ y(2) \\ \vdots \\ y(n-1) \\ y(n) \end{bmatrix} \quad (4-32)$$

We can obtain:

$$U_{j+1} = P(U_j + LE_j) \quad (4-33)$$

$$U_{j+1} = Q(I - LP)U_j + QL(U_{ref} - D) \quad (4-34)$$

For an asymptotically stable system, $\rho(Q(I - LP))$ is between -1 and 1 . ρ is the eigenvalue of the matrix.

The final error between the real output and desired output is:

$$E_{\infty} = \left(I - P(I - Q(I - LP))^{-1}QL \right) (U_{ref} - D) \quad (4-35)$$

When $Q = I$, the final error is 0. For the same system uncertainty, Q is chosen as 1 to make sure the track error will become 0 and L is chosen 10. The result of the uncertain system after 13 iteration is shown in Figure 4-15.

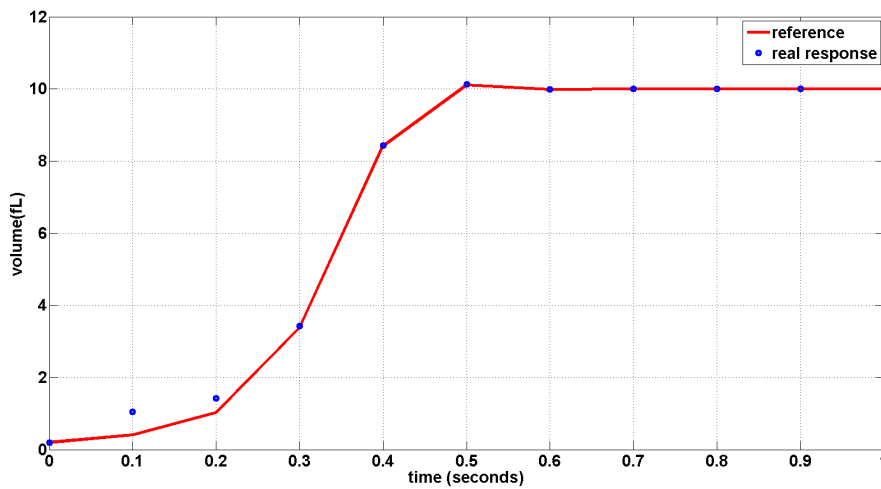


Figure 4-15: Simulation result of combining iterative learning control with feedback linearization.

The RMS of the error between the desired output and real output in each iteration is shown in Figure 4-16. The RMS is defined as:

$$RMS = \sqrt{\frac{\sum_{k=1}^{k=N} (y(k) - u_{ref}(k))^2}{N}} \quad (4-36)$$

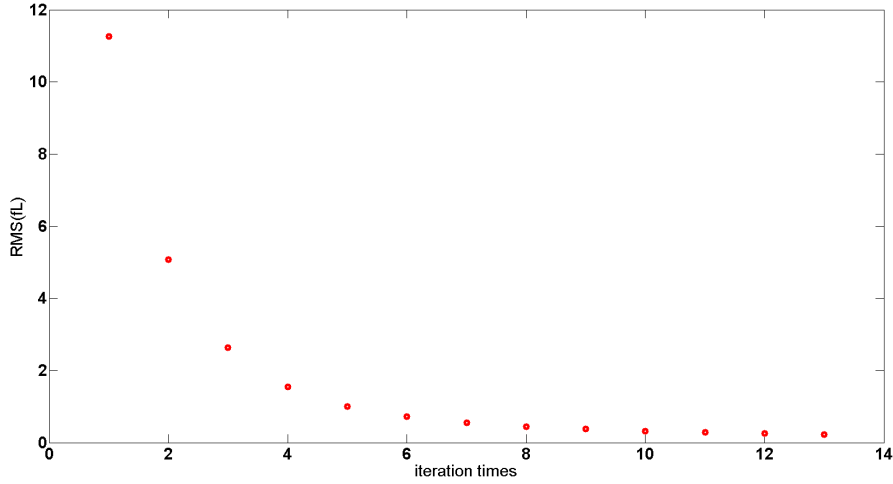


Figure 4-16: The RMS of the error between desired output and real output at each iteration.

It shows after 8 iteration, the error is almost 0.

4-5 Model reference adaptive control (MRAC)

The parameters of the system can be obtained by using system identification, but it needs extra step to obtain useful input and output data of the system. So here use indirect MRAC controller to control the system with unknown parameters. The main idea of indirect MRAC is to use the estimated parameter of the system to control it [43]. The reference is:

$$\dot{y}_m = -a_m y_m + b_m u \quad (4-37)$$

where a_m and b_m are positive.

The model (2-13) could be expressed as:

$$\dot{y} = \frac{a}{y^{1/3}} + bu \quad (4-38)$$

where

$$a = \frac{\gamma c_1 \sqrt[3]{c_2}}{R_H}$$

$$b = \frac{1}{R_H}$$

To make output of the nonlinear system the same as the output of the linear reference model, the input should be:

$$u = -\frac{a}{b} \frac{1}{y^{1/3}} - \frac{a_m}{b} y + \frac{b_m}{b} u_{ref} \quad (4-39)$$

Because a and b are not known, they are assumed as estimation number $a(t)$ and $b(t)$, then the input is:

$$u(t) = -n(t) \frac{1}{x^{1/3}} - l(t)x + q(t)u_{ref} \quad (4-40)$$

where $n(t) = \frac{a(t)}{b(t)}$, $l(t) = \frac{a_m}{b(t)}$ and $q(t) = \frac{b_m}{b(t)}$. So the function for error $e = y - y_m$ can be expressed as:

$$\dot{e}(t) = -a_m e + b(-\tilde{n} \frac{1}{y^{1/3}} - \tilde{l} y + \tilde{q} u_{ref}) \quad (4-41)$$

where $\tilde{n} = \frac{a(t)}{b(t)} - \frac{a}{b}$, $\tilde{l} = \frac{a_m}{b(t)} - \frac{a_m}{b}$ and $\tilde{q} = \frac{b_m}{b(t)} - \frac{b_m}{b}$. For the Lyapunov function:

$$V(e, \tilde{n}, \tilde{l}, \tilde{q}) = \frac{e^2}{2} + \begin{bmatrix} \tilde{n} & \tilde{l} & \tilde{q} \end{bmatrix} \Gamma \begin{bmatrix} \tilde{n} \\ \tilde{l} \\ \tilde{q} \end{bmatrix} \quad (4-42)$$

where Γ is positive matrix:

$$\Gamma = \begin{bmatrix} a_{11} & a_{12} & a_{13} \\ a_{21} & a_{22} & a_{23} \\ a_{31} & a_{32} & a_{33} \end{bmatrix} \quad (4-43)$$

If

$$\begin{bmatrix} \dot{\tilde{n}} \\ \dot{\tilde{l}} \\ \dot{\tilde{q}} \end{bmatrix} = \Gamma^{-1} e \begin{bmatrix} \frac{1}{y^{1/3}} \\ y \\ -u_{ref} \end{bmatrix} \quad (4-44)$$

the following equation can be obtained:

$$\dot{V} = -a_m e^2 \quad (4-45)$$

It shows that the error between the response of the reference system and nonlinear system will become the same as the time going on.

For $a_m = 10$, $b_m = 1$, contact time is 0.01 s, and Γ^{-1} is $\begin{bmatrix} 1 & 1 & -100 \\ 1 & 100 & -5000 \\ 100 & 5000 & 600 \end{bmatrix}$. The result is

shown in Figure 4-17. It shows before the volume becomes stable, the large initial value of the Laplace pressure influences the performance of the controller.

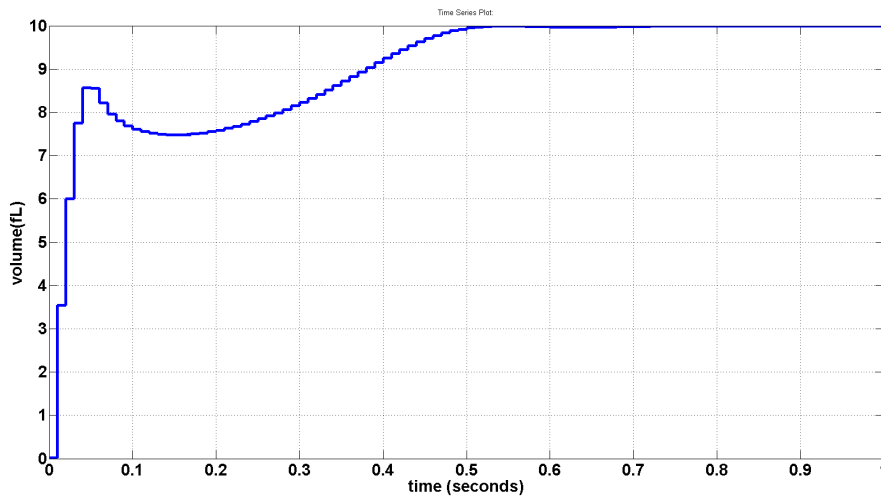


Figure 4-17: The result of adaptive control.

4-6 Conclusion

Before applying the controllers designed in this chapter, it is mandatory to make sure that the aperture is inside the liquid bridge. System identification is needed to design series PID controller, parallel PI controller and combination of feedback linearization and iterative learning control. Because of the time delay and nonlinearity of the system, overshoot can not be solved for series PID controller and parallel PI controller. To solve the influence from system nonlinearity, feedback linearization is used. When there is system uncertainty, iterative learning controller is preferred to be applied to deal with the corresponding steady state error. For the MRAC controller, it is not necessary to identify the parameters of the system, but there are 6 parameters to be tuned, which makes it hard to find the best performance of the system.

Conclusion and Future work

Introduction

The goal of this thesis is to control the dosing process of hollow AFM cantilever. A brief introduction on the working principle of AFM was given. Four types of AFM based liquid manipulation methods were introduced and compared. Hollow cantilever has the advantage of aspirating and dispensing liquids by providing different pressures. Later, the necessary principles to understand the dosing process were discussed in detail, three different ways to get the geometry information of the liquid bridge were introduced. To get the proper model to design controllers, the Young–Laplace equation method was chosen.

Model of the dosing process

Combining the Laplace pressure theory and electrical circuit analogy theory, the dynamic model of the dosing process can be developed. The flow rate depends on the hydraulic resistance of the device, the pressure applied externally and the Laplace pressure inside the liquid bridge. The complexity exists in the pressure inside the liquid bridge, and the pressure can be obtained by using the volume of liquid and contact angles. Because the contact angle is determined by the liquid and the substrate, so for different substrates, the process is not the same. Assuming the dynamic contact angle is constant, the Laplace pressure inside the liquid bridge can be simplified to $\gamma c_1 \sqrt[3]{\frac{c_2}{V}}$, where c_1 and c_2 are constants for the same substrate.

Experiments with nano-litre droplets

For this volume scale, experiments were performed by a precision stainless steel hollow tip with an inner diameter of $100 \mu\text{m}$ and outer diameter of $240 \mu\text{m}$. When the tip was suspended in the air, according to the liquid spherical cap shape and small base radius, the results from the model match well with the experimental data only by considering the influence of Laplace pressure. This means that if the geometry information of liquid is known, the Laplace

pressure calculated according to that can influence the dosing process. When the tip touches the substrate, the Laplace pressure becomes very small according to the large volume of the liquid bridge and liquid geometry. So the volume can show linear relation with contact time when the same pressure is applied.

Experiments with pico-femto-litre droplets (using hollow cantilevers)

For this volume scale, experiments were performed by hollow AFM cantilever. When dispense liquids on hydrophobic substrate, burst of volume can be observed. The reason is that when the condensed liquid bridge touches the aperture, the volume will increase dramatically according to the large pressure applied externally. So to dose measurable volume of liquids after the liquid bridge touches the aperture, small pressure and small aperture size are required. The result shows that if the substrate is hydrophobic the Laplace pressure inside the liquid bridge can be neglected. When dispense liquid on the hydrophilic surface, the volume range is in 10^4 fL. This is caused by the large Laplace pressure of the liquid bridge. The proposed model can demonstrate the dosing process on different substrates with VAF larger than 90%.

Controllers

For the controllers, the input is the pressure provided externally, and the output is the volume. Before applying the designed controller, humidity is needed to be high enough to make sure the liquid bridge touches the aperture of the tip, otherwise the process is not continuous. To design controllers, the parameters of the model are needed to be obtained, least square method was used. First, series PID controller and parallel PI controller have been designed. Because of the nonlinearity and delay, overshoot can not be avoided when apply them to nonlinear model. To solve the nonlinearity, feedback linearization was applied. To overcome system uncertainty without overshoot, feedback linearization was combined with iterative learning control. Model reference adaptive control was designed, because it does not need to identify the parameters of the system. But there are six parameters needed to be tuned, it is hard to find the controller has the best performance.

Future Work

To verify whether the model is valid in the femto-litre range on a hydrophilic surface. Hollow cantilever with small aperture size is recommended to use in the next experiments. A small aperture size means large hydraulic resistance and it will help to obtain small volume that can be measured by AFM deflection curves even on hydrophilic surfaces. The hollow cantilever with aperture at the top of the tip is recommended to do experiments, because the condensed liquid bridge can directly touch the aperture. The increase of volume is always continuous. In the deflection graphs, the approaching curve and retracting curve can not match very well, which will lead in error of the measured break-up height. So the closed loop control of the piezoelectric z-stage position should be added. For designing controllers, easy tunable model-free control methods are recommended for improving convenience of applying controllers into practice.

Appendix A

The derivation of the formulas

A-1 Young–Laplace equation

According to the Figure 2-4, when $\epsilon < 90^\circ$, the mean H_{mean} curvature of the liquid bridge is:

$$2H_{mean} = \frac{\frac{d^2z}{dr^2}}{\left[1 + \left(\frac{dz}{dr}\right)^2\right]^{\frac{3}{2}}} + \frac{\frac{dz}{dr}}{r\left[1 + \left(\frac{dz}{dr}\right)^2\right]^{\frac{1}{2}}} \quad (\text{A-1})$$

When $\epsilon > 90^\circ$, the curvature of the liquid brige is:

$$2H_{mean} = -\frac{\frac{d^2z}{dr^2}}{\left[1 + \left(\frac{dz}{dr}\right)^2\right]^{\frac{3}{2}}} - \frac{\frac{dz}{dr}}{r\left[1 + \left(\frac{dz}{dr}\right)^2\right]^{\frac{1}{2}}} \quad (\text{A-2})$$

Define $u = -\sin(\epsilon)$, $y = \frac{z}{R}$ and $x = \frac{r}{R}$. When $\epsilon < 90^\circ$, we obtain:

$$\frac{dz}{dr} = \frac{dy}{dx} = -\frac{u}{\sqrt{1-u^2}} \quad (\text{A-3})$$

$$\frac{d^2z}{dr^2} = \frac{d^2y}{dx^2} = -\frac{1}{(1-u^2)^{\frac{3}{2}}} \frac{du}{dr} \quad (\text{A-4})$$

$$1 + \left(\frac{dz}{dr}\right)^2 = \frac{1}{1-u^2} \quad (\text{A-5})$$

So (A-1) becomes:

$$2H_{mean} = -\frac{du}{dr} - \frac{u}{r} \quad (\text{A-6})$$

Because $r = \frac{x}{R}$, we obtain:

$$2H_{mean}R = -\frac{du}{dx} - \frac{u}{x} \quad (\text{A-7})$$

At the same way, when $\epsilon > 90^\circ$, we obtain:

$$\frac{dz}{dr} = \frac{dy}{dx} = \frac{u}{\sqrt{1-u^2}} \quad (\text{A-8})$$

$$\frac{d^2z}{dr^2} = \frac{d^2y}{dx^2} = \frac{1}{(1-u^2)^{\frac{3}{2}}} \frac{du}{dx} \quad (\text{A-9})$$

(A-2) becomes:

$$2H_{mean}R = -\frac{du}{dx} - \frac{u}{x} \quad (\text{A-10})$$

It is the same when $\epsilon < 90^\circ$. To solve (A-7), the steps are:

$$\frac{2H_{mean}R + u}{x} = \frac{-du}{dx} \rightarrow \frac{x}{2H_{mean}Rx + u} = \frac{-dx}{du} \quad (\text{A-11})$$

When $\frac{x}{u} = v$, then:

$$\begin{aligned} \frac{v}{2H_{mean}Rv + 1} &= -v - u \frac{dv}{du} \rightarrow \frac{2v + 2H_{mean}Rv^2}{1 + 2HRv} = -u \frac{dv}{du} \rightarrow \frac{1}{2} \ln(v + H_{mean}Rv^2) = -\ln u + c_1 \\ &\rightarrow \frac{x}{u} + H_{mean}R\left(\frac{x}{u}\right)^2 = \frac{c_2}{u^2} \rightarrow ux + H_{mean}Rx^2 = c_2 \end{aligned} \quad (\text{A-12})$$

Therefore, we obtain:

$$x = \frac{-u \pm \sqrt{u^2 + 4H_{mean}Rc_2}}{2H_{mean}R} \quad (\text{A-13})$$

For the boundary conditions we have:

$$u_1 = -\sin(\theta_1 + \psi) \quad (\text{A-14})$$

$$x_1 = \sin(\psi) \quad (\text{A-15})$$

$$y_1 = d + z - \cos(\psi) \quad (\text{A-16})$$

$$u_2 = -\sin(\pi - \theta_2) \quad (\text{A-17})$$

$$y_2 = 0 \quad (\text{A-18})$$

Assume $c = 4H_{mean}Rc_2$, we obtain:

$$c = 4H_{mean}^2R^2 \sin^2 \psi - 4H_{mean}R \sin(\psi) \sin(\theta_1 + \psi) \quad (\text{A-19})$$

When $\eta < 90^\circ$, from (A-3), we obtain:

$$dy = \frac{-u}{\sqrt{1-u^2}} \frac{dx}{du} du \quad (\text{A-20})$$

So from (A-13), we can obtain:

$$y_1 - y_* = \int_{u_*}^{u_1} \frac{-u}{\sqrt{1-u^2}} \frac{-1 \pm \frac{u}{\sqrt{u^2+c}}}{2H_{mean}R} du \quad (\text{A-21})$$

Because $x > 0$, $H_{mean} < 0$, $y_1 - y_* > 0$, $du > 0$, $\frac{-u}{\sqrt{1-u^2}} > 0$, the sign of \pm should be $-$, otherwise x will become negative. Therefore, we obtain:

$$\begin{aligned} y_1 - y_* &= \int_{-\sin(90^\circ)}^{-\sin(\theta_1+\psi)} \frac{-u}{\sqrt{1-u^2}} \frac{-\sqrt{u^2+c} - u}{2H_{mean}R\sqrt{u^2+c}} du \\ &= \int_{-\sin(90^\circ)}^{-\sin(\theta_1+\psi)} \left(\frac{u}{2H_{mean}R\sqrt{1-u^2}} + \frac{u^2}{2H_{mean}R\sqrt{u^2+c}\sqrt{1-u^2}} \right) du \end{aligned} \quad (\text{A-22})$$

$$\int_{-\sin(90^\circ)}^{-\sin(\theta_1+\psi)} \left(\frac{u}{2H_{mean}R\sqrt{1-u^2}} \right) du = \frac{-\cos(\theta_1+\psi)}{2H_{mean}R} \quad (\text{A-23})$$

$$\int_{-\sin(90^\circ)}^{-\sin(\theta_1+\psi)} \left(\frac{u^2}{2H_{mean}R\sqrt{u^2+c\sqrt{1-u^2}}} \right) du = \frac{1}{2HR} \left(-\frac{c}{\sqrt{1+c}} F(\pi/2 - (\psi + \theta_1), k) + \sqrt{1+c} E(\pi/2 - (\psi + \theta_1), k) \right) \quad (\text{A-24})$$

where, $k = \sqrt{\frac{1}{1+c}}$. Similarly, when $\epsilon > 90^\circ$, we obtain

$$y_* - y_2 = \int_{-\sin(\pi-\theta_2)}^{-\sin \pi/2} \frac{u}{\sqrt{1-u^2}} \frac{dx}{du} du = \int_{-\sin(\pi-\theta_2)}^{-\sin \pi/2} \left(-\frac{u}{2H_{mean}R\sqrt{1-u^2}} - \frac{u^2}{2H_{mean}R\sqrt{u^2+c\sqrt{1-u^2}}} \right) du \quad (\text{A-25})$$

$$\int_{-\sin(\pi-\theta_2)}^{-\sin \pi/2} \left(-\frac{u}{2H_{mean}R\sqrt{1-u^2}} \right) du = -\cos(\theta_2) \frac{1}{2H_{mean}R} \quad (\text{A-26})$$

$$\int_{-\sin(\pi-\theta_2)}^{-\sin \pi/2} \left(-\frac{u^2}{2H_{mean}R\sqrt{u^2+c\sqrt{1-u^2}}} \right) du = \left(\frac{c}{\sqrt{1+c}} F(\theta_2 - \pi/2, k) - \sqrt{1+c} E(\theta_2 - \pi/2, k) \right) \quad (\text{A-27})$$

So we can obtain:

$$y_1 - y_2 = \frac{1}{2H_{mean}R} \left\{ -\cos(\theta_1 + \psi) - \cos \theta_2 + \sqrt{1+c} [E(\theta_2 - \pi/2, k) - E(\pi/2 - (\psi + \theta_1), k)] + \frac{c}{\sqrt{1+c}} [F(\theta_2 - \pi/2, k) - F(\pi/2 - (\psi + \theta_1), k)] \right\} \quad (\text{A-28})$$

Because $y_2 = 0$, we can obtain:

$$2H_{mean}R = \frac{1}{y_1} \left\{ -\cos(\theta_1 + \psi) - \cos \theta_2 + \sqrt{1+c} [E(\theta_2 - \pi/2, k) - E(\pi/2 - (\psi + \theta_1), k)] + \frac{c}{\sqrt{1+c}} [F(\theta_2 - \pi/2, k) - F(\pi/2 - (\psi + \theta_1), k)] \right\} \quad (\text{A-29})$$

According to (A-13), we obtain:

$$x(\epsilon) = \frac{1}{2H_{mean}R} (\sin \epsilon - \sqrt{\sin^2 \epsilon + c}) \quad (\text{A-30})$$

According to (A-22) and (A-25), we obtain:

$$y = \frac{1}{2H_{mean}R} \left\{ -\cos \epsilon - \sqrt{1+c} [E(\theta_2 - \pi/2, k) - E(\pi/2 - \epsilon, k)] + \frac{c}{\sqrt{1+c}} [F(\theta_2 - \pi/2, k) - F(\pi/2 - \epsilon, k)] \right\} \quad (\text{A-31})$$

A-2 Volume of the liquid bridge with tip touching the substrate

According to (A-30), (A-31), $r(\epsilon) = x(\epsilon)R$ and $z(\epsilon) = y(\epsilon)R$ we obtain:

$$\begin{aligned} dy(\epsilon) &= d \frac{1}{2H_{mean}R} \left\{ -\cos \epsilon - \sqrt{1+c} [E(\theta_2 - \pi/2, k) - E(\pi/2 - \epsilon, k)] + \frac{c}{\sqrt{1+c}} [F(\theta_2 - \pi/2, k) \right. \\ &\quad \left. - F(\pi/2 - \epsilon, k)] \right\} \\ &= \frac{1}{2H_{mean}R} d \left\{ -\cos \epsilon + \int_{\pi-\theta_2}^{\epsilon} \frac{\sin^2 x}{\cos x \sqrt{\sin^2 x + c}} d(-\sin x) \right\} = \frac{1}{2H_{mean}R} \left(\sin \epsilon + \frac{-\sin^2 \epsilon}{\sqrt{\sin^2 \epsilon + c}} d\epsilon \right) \end{aligned} \quad (\text{A-32})$$

The volume of liquid bridge is:

$$\begin{aligned} V &= R^3 \int_{\pi-\theta_2}^{\theta_1+\psi} \pi x^2(\epsilon) dy(\epsilon) \\ &= R^3 \int_{\pi-\theta_2}^{\theta_1+\psi} \frac{\pi}{(2H_{mean}R)^3} \left(\sin^2(x) - 2 \sin(x)(\sin^2(x) + c)^{1/2} + \sin^2(x) + c \right) \left(\sin(x) - \frac{\sin^2(x)}{\sqrt{(\sin^2(x) + c)}} \right) dx \end{aligned} \quad (\text{A-33})$$

A-3 Volume of the liquid bridge from the break-up height

Figure 2-8 shows the break-up instant. The horizontal coordinate is y , the coordinate of the right half of the liquid bridge is $x(y)$. The radius of the liquid bridge r is:

$$r = \frac{h}{\cos \theta} \quad (\text{A-34})$$

The horizontal radius of the liquid bridge $x(y)$ is:

$$x(y) = \frac{h}{\cos \theta} - \sqrt{\left(\frac{h}{\cos \theta}\right)^2 - (h-y)^2} \quad (\text{A-35})$$

The volume of the liquid bridge by using the break-up height h is:

$$\begin{aligned} V &= \pi \int_0^h x^2(y) dy = \pi \int_0^h \left(\frac{h}{\cos \theta} - \sqrt{\left(\frac{h}{\cos \theta}\right)^2 - (h-y)^2} \right)^2 dy \\ &= \pi \left\{ \frac{2h^3}{\cos^2 \theta} - \frac{h^3}{3} - 2 \frac{h^3}{\cos^3 \theta} \left(\frac{1}{2} \cos \theta \sqrt{1 - \cos^2 \theta} + \frac{1}{2} \sin^{-1}(\cos \theta) \right) \right\} \end{aligned} \quad (\text{A-36})$$

Appendix B

Experimental data

B-1 Deflection graphs of dispensing on the hydrophobic surface

In the section 3-6-2, different pressure with different contact time has been applied. The deflection graphs of different experiments are shown here. When provide 1×10^5 Pa on SiO_2 substrate with contact time 0s, 0.1s, 0.3s and 1s. The deflection graphs are shown in the Figure B-1.

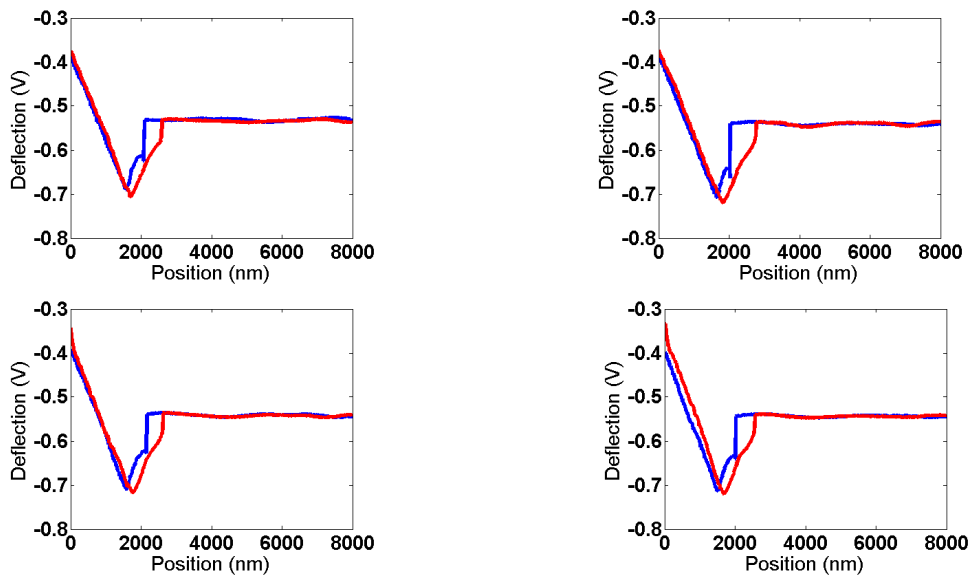


Figure B-1: Deflection graphs when provide 1×10^5 Pa on SiO_2 .

Because there is not significant increase of volume, so increase the provided pressure to 1.5×10^5 Pa, and at different contact time, the same experiment is done three times. The deflection curves with different contact time are shown in Figure B-2, Figure B-3 and Figure B-4.

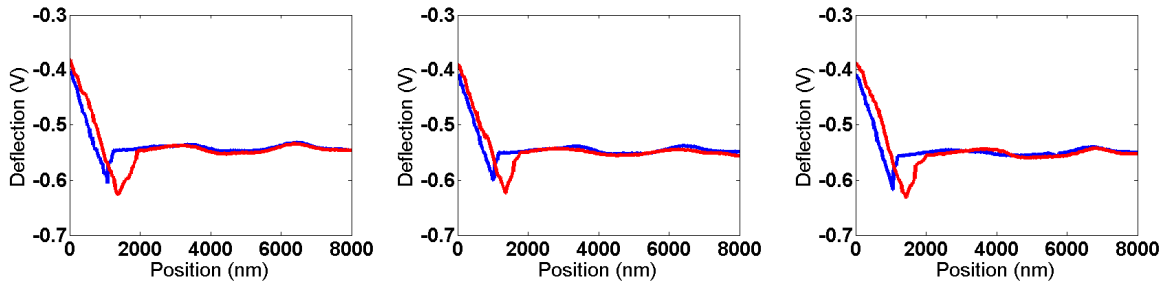


Figure B-2: Deflection graphs when provide 1.5×10^5 Pa on SiO_2 with 0s contact time.

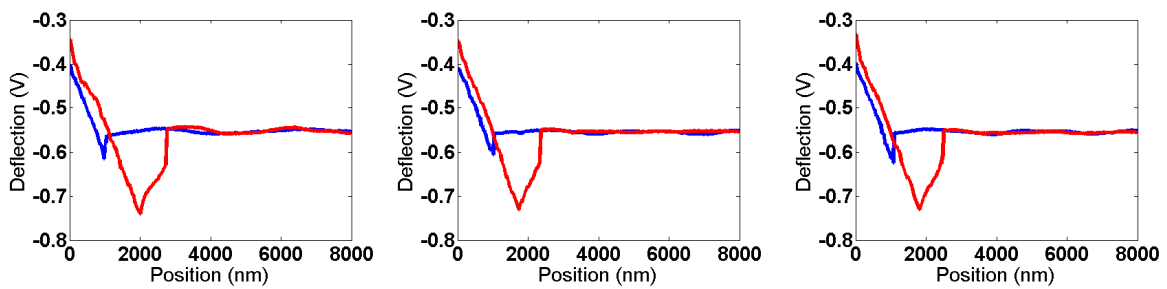


Figure B-3: Deflection graphs when provide 1.5×10^5 Pa on SiO_2 with 0.2s contact time.

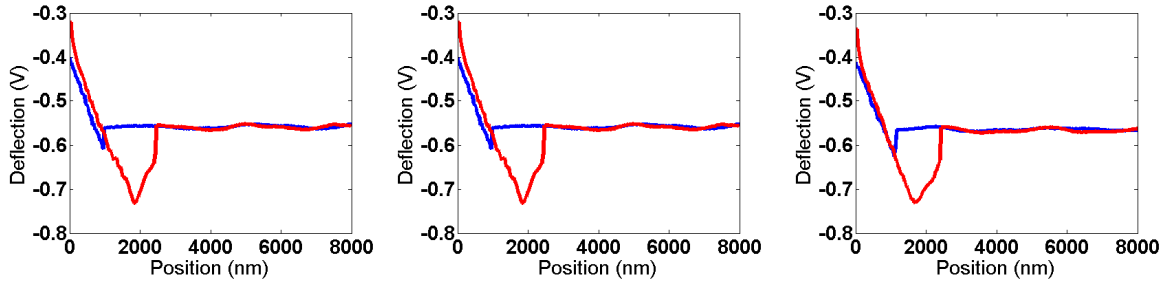


Figure B-4: Deflection graphs when provide 1.5×10^5 Pa on SiO_2 with 0.3s contact time.

Because there is burst, so decrease the provided pressure to 1.2×10^5 Pa. The deflection graphs are shown in Figure B-5, B-6, B-7 and B-8.

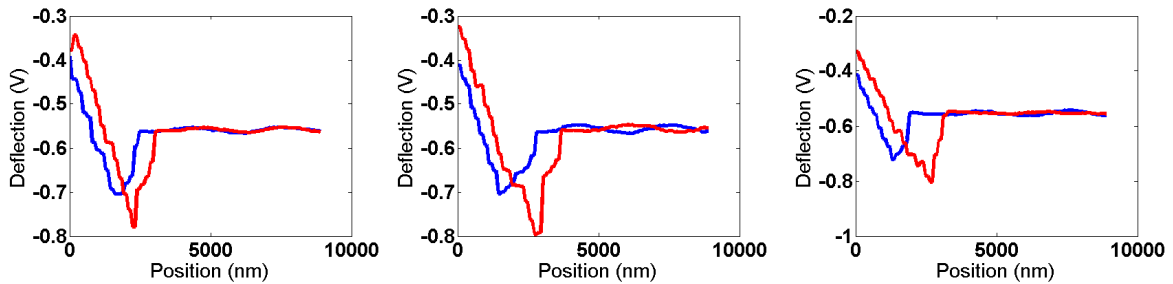


Figure B-5: Deflection graphs when provide 1.2×10^5 Pa on SiO_2 with 0s contact time.

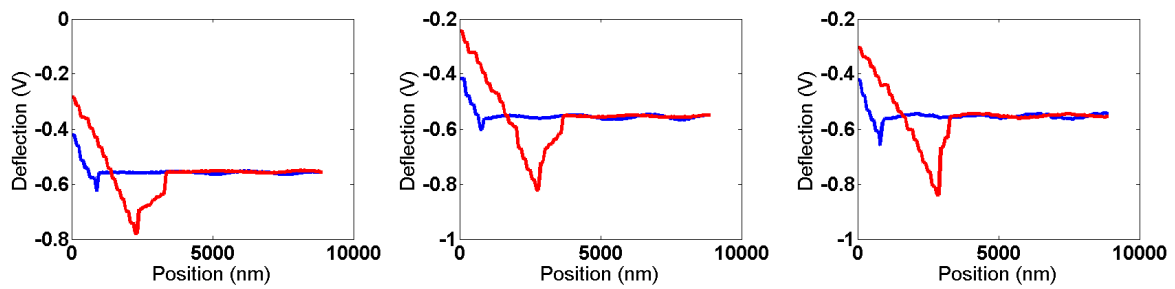


Figure B-6: Deflection graphs when provide 1.2×10^5 Pa on SiO_2 with 0.2s contact time.

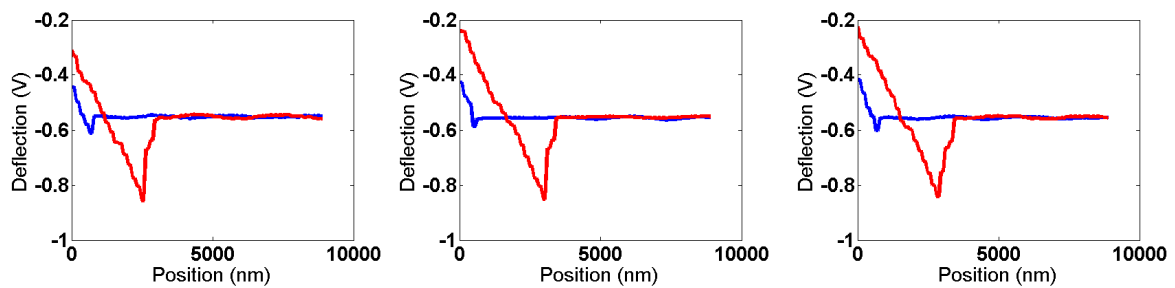


Figure B-7: Deflection graphs when provide 1.2×10^5 Pa on SiO_2 with 0.3s contact time.

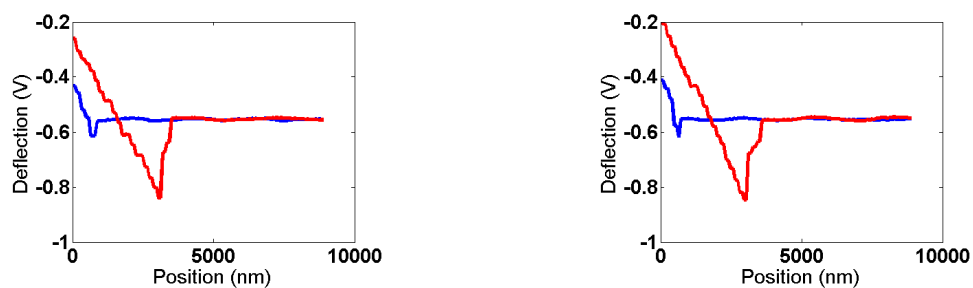


Figure B-8: Deflection graphs when provide 1.2×10^5 Pa on SiO_2 with 0.4s contact time.

Change the substrate to functionalized silicon, and provide pressure 1.2×10^5 Pa with different contact time. The deflection graphs are shown in Figure B-9, Figure B-10, Figure B-11 and Figure B-12.

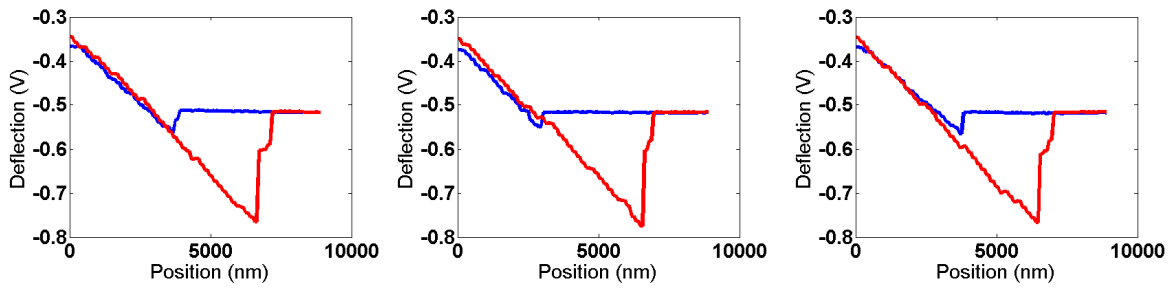


Figure B-9: Deflection graphs when provide 1.2×10^5 Pa on functionalized silicon with 0 s contact time.

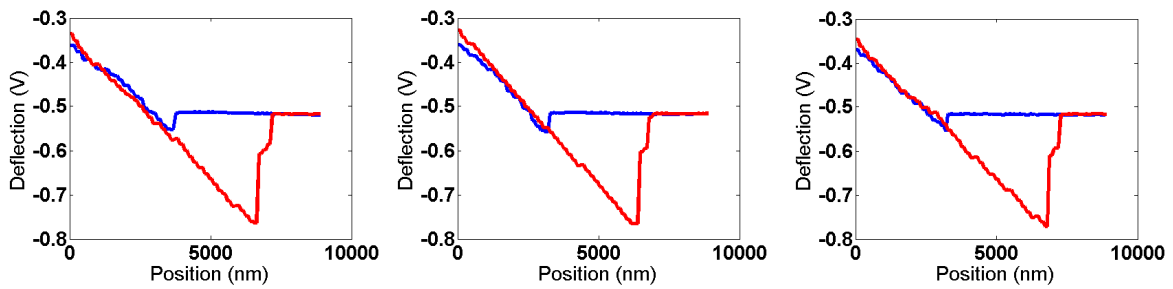


Figure B-10: Deflection graphs when provide 1.2×10^5 Pa on functionalized silicon with 0.2 s contact time.

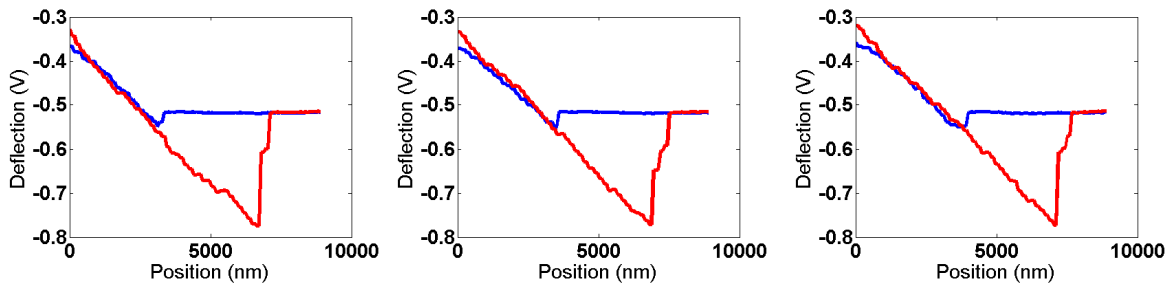


Figure B-11: Deflection graphs when provide 1.2×10^5 Pa on functionalized silicon with 0.3 s contact time.

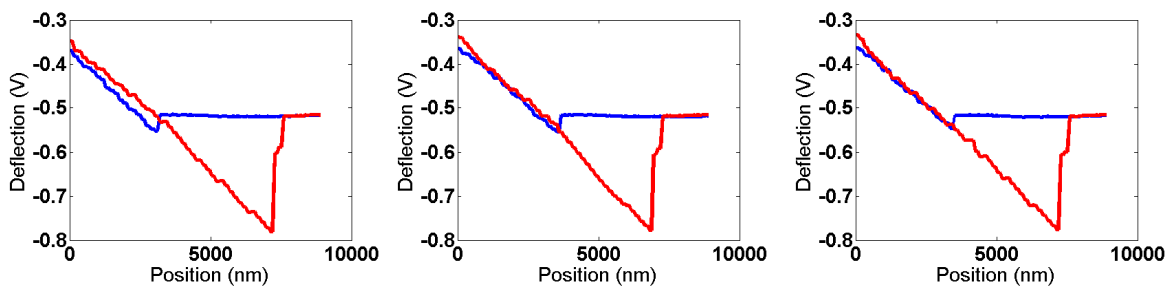


Figure B-12: Deflection graphs when provide 1.2×10^5 Pa on functionalized silicon with 0.4 s contact time.

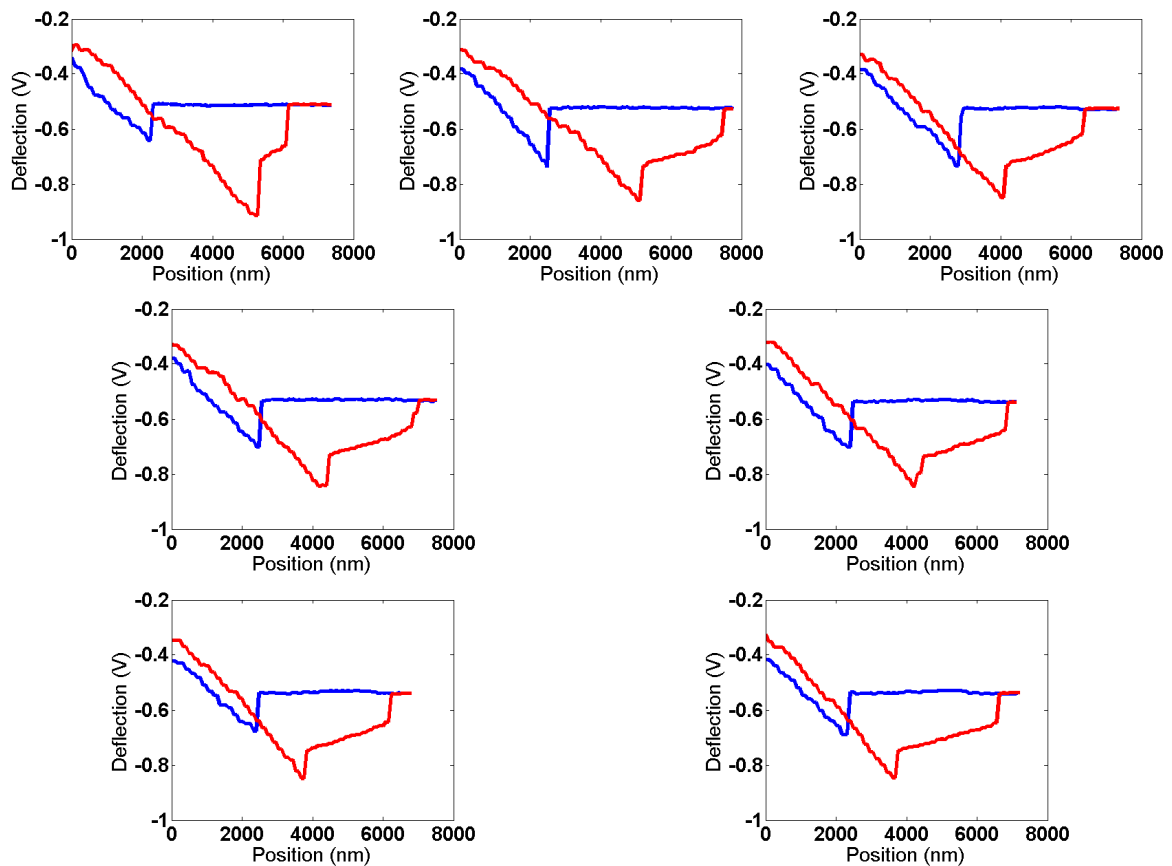


Figure B-13: Deflection graphs when provide 0 Pa on SiO_2 with 0 s contact time.

After several burst happened, provide 0 Pa, the deflection graphs are shown in Figure B-13.

B-2 Captured frames of the dispensing process on the hydrophilic surface

When dispensing on hydrophilic surface, the Laplace pressure in the liquid bridge is too large, no deflection graphs can be obtained. So the volume is calculated according to the captured frames in the recorded video. The frames are shown in Figure B-14 and B-15.

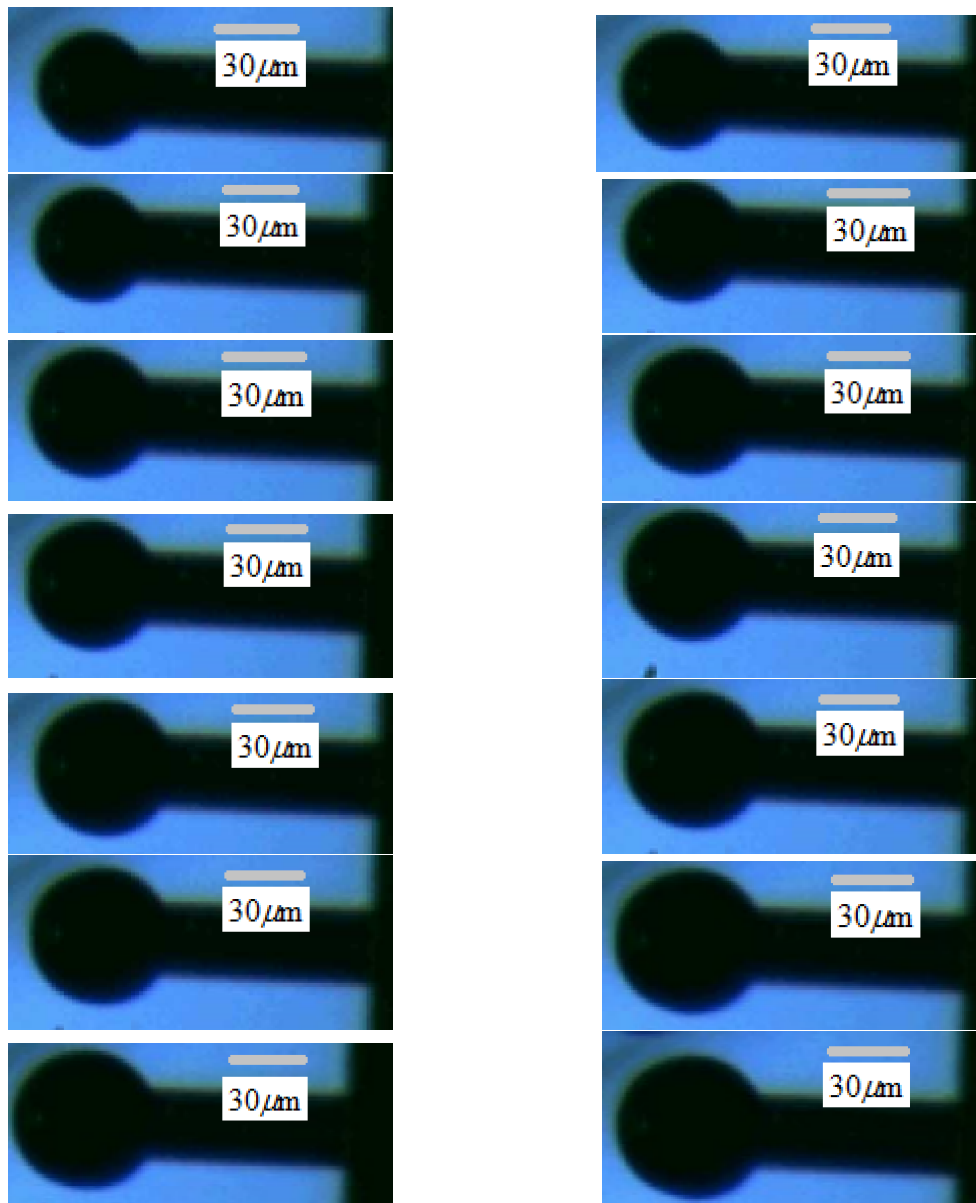


Figure B-14: The captured frames of the video of dispensing process, when the distance between the tip and substrate is small.

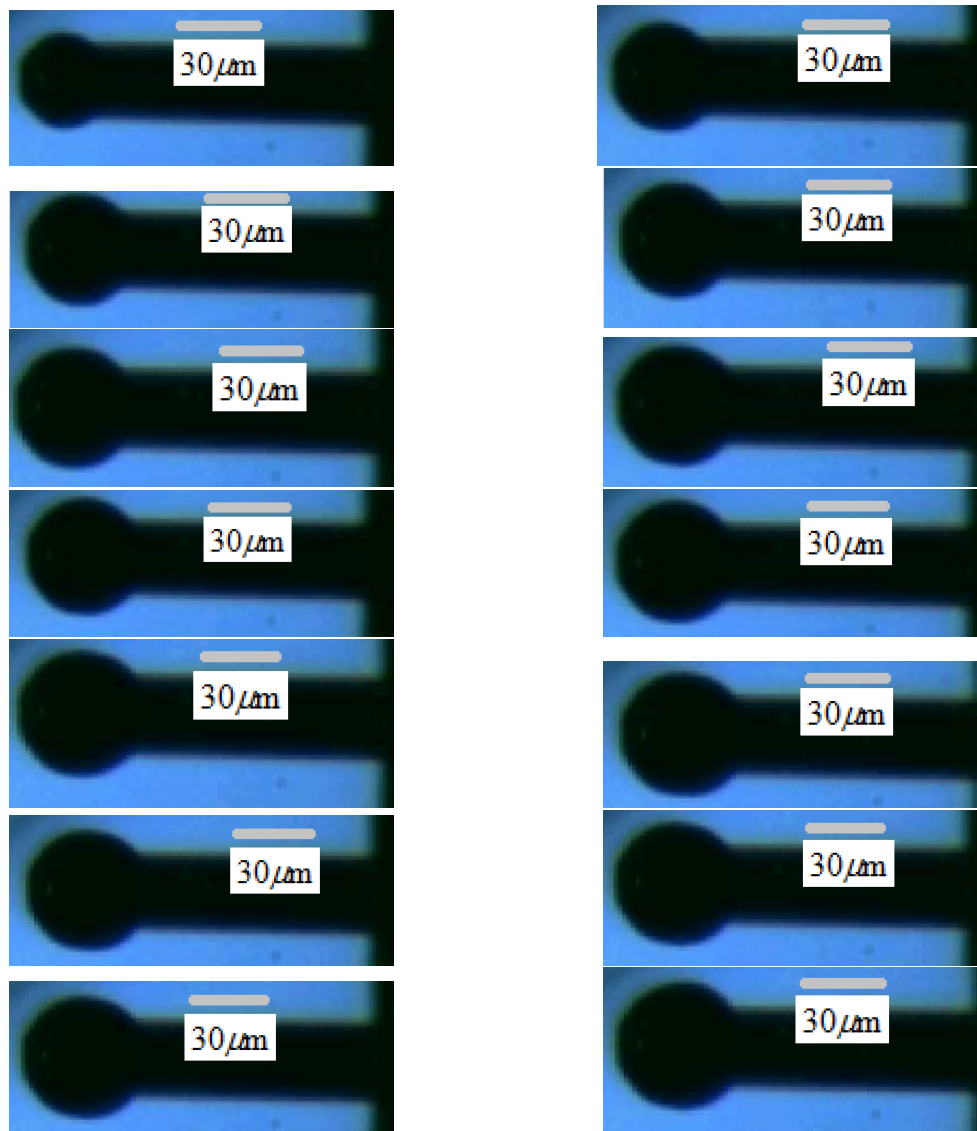


Figure B-15: The captured frames of the video of dispensing process, when the distance between the tip and substrate is large.

Bibliography

- [1] K. E. Drexler and M. Minsky, *Engines of creation*. Fourth Estate London, 1990.
- [2] R. B. T. De Gruiter, *Dosing of femto liter volumes using hollow cantilever AFM*. PhD thesis, TU Delft, Delft University of Technology, 2015.
- [3] N. Almeida, E. Batista, and E. Filipe, “Performance studies in micropipette calibration,” in *16th International Congress of Metrology*, p. 06010, EDP Sciences, 2013.
- [4] M. K. Ghatkesar, H. H. P. Garza, F. Heuck, and U. Staufer, “Scanning probe microscope-based fluid dispensing,” *Micromachines*, vol. 5, no. 4, pp. 954–1001, 2014.
- [5] S. J. Gaskell, “Electrospray: principles and practice,” *Journal of mass spectrometry*, vol. 32, no. 7, pp. 677–688, 1997.
- [6] P. Eaton and P. West, *Atomic force microscopy*. Oxford University Press, 2010.
- [7] A. Schirmeisen, B. Anczykowski, H. Hölscher, and H. Fuchs, “Dynamic modes of atomic force microscopy,” in *Nanotribology and Nanomechanics I*, pp. 307–353, Springer, 2011.
- [8] M. Jaschke and H.-J. Butt, “Deposition of organic material by the tip of a scanning force microscope,” *Langmuir*, vol. 11, no. 4, pp. 1061–1064, 1995.
- [9] J. Jang, S. Hong, G. C. Schatz, and M. A. Ratner, “Self-assembly of ink molecules in dip-pen nanolithography: A diffusion model,” *The Journal of Chemical Physics*, vol. 115, no. 6, pp. 2721–2729, 2001.
- [10] A. Meister, S. Jeney, M. Liley, T. Akiyama, U. Staufer, N. De Rooij, and H. Heinzelmann, “Nanoscale dispensing of liquids through cantilevered probes,” *Microelectronic engineering*, vol. 67, pp. 644–650, 2003.
- [11] K.-H. Kim, N. Moldovan, C. Ke, and H. D. Espinosa, “A novel afm chip for fountain pen nanolithography-design and microfabrication,” in *MRS Proceedings*, vol. 782, pp. A5–56, Cambridge Univ Press, 2003.

- [12] P.-G. De Gennes, F. Brochard-Wyart, and D. Quéré, *Capillarity and wetting phenomena: drops, bubbles, pearls, waves*. Springer Science & Business Media, 2013.
- [13] B. J. Kirby, *Micro-and nanoscale fluid mechanics: transport in microfluidic devices*. Cambridge University Press, 2010.
- [14] K. W. Oh, K. Lee, B. Ahn, and E. P. Furlani, “Design of pressure-driven microfluidic networks using electric circuit analogy,” *Lab on a Chip*, vol. 12, no. 3, pp. 515–545, 2012.
- [15] D. Di Carlo, “Inertial microfluidics,” *Lab on a Chip*, vol. 9, no. 21, pp. 3038–3046, 2009.
- [16] J. T. Korhonen, T. Huhtamaki, O. Ikkala, and R. H. Ras, “Reliable measurement of the receding contact angle,” *Langmuir*, vol. 29, no. 12, pp. 3858–3863, 2013.
- [17] M. F. Amir Farrokh Payam, Mehran jalalifar, “Modeling and analysis of capillary force interaction for common afm tip shapes,” *World Applied Sciences*, vol. 16, no. 12, 2012.
- [18] C. D. Willett, M. J. Adams, S. A. Johnson, and J. P. Seville, “Capillary bridges between two spherical bodies,” *Langmuir*, vol. 16, no. 24, pp. 9396–9405, 2000.
- [19] F. Orr, L. Scriven, and A. P. Rivas, “Pendular rings between solids: meniscus properties and capillary force,” *Journal of Fluid Mechanics*, vol. 67, no. 04, pp. 723–742, 1975.
- [20] J. C. Melrose, “Model calculations for capillary condensation,” *AIChE Journal*, vol. 12, no. 5, pp. 986–994, 1966.
- [21] L. Fabié, H. Durou, and T. Ondarc̃ıghu, “Capillary forces during liquid nanodispensing,” *Langmuir*, vol. 26, no. 3, pp. 1870–1878, 2009.
- [22] C. D. O’Connell, M. J. Higgins, D. Marusic, S. E. Moulton, and G. G. Wallace, “Liquid ink deposition from an atomic force microscope tip: deposition monitoring and control of feature size,” *Langmuir*, vol. 30, no. 10, pp. 2712–2721, 2014.
- [23] R. Cornish, “Flow in a pipe of rectangular cross-section,” *Proceedings of the Royal Society of London. Series A, Containing Papers of a Mathematical and Physical Character*, vol. 120, no. 786, pp. 691–700, 1928.
- [24] H.-J. Butt, K. Graf, and M. Kappl, “Liquid surfaces,” *Physics and Chemistry of Interfaces*, pp. 4–25, 2006.
- [25] D. Asay, M. De Boer, and S. Kim, “Equilibrium vapor adsorption and capillary force: Exact laplace–young equation solution and circular approximation approaches,” *Journal of Adhesion Science and Technology*, vol. 24, no. 15-16, pp. 2363–2382, 2010.
- [26] D. Y. Kwok and A. W. Neumann, “Contact angle measurement and contact angle interpretation,” *Advances in colloid and interface science*, vol. 81, no. 3, pp. 167–249, 1999.
- [27] C. Lam, R. Wu, D. Li, M. Hair, and A. Neumann, “Study of the advancing and receding contact angles: liquid sorption as a cause of contact angle hysteresis,” *Advances in colloid and interface science*, vol. 96, no. 1, pp. 169–191, 2002.

-
- [28] P. Lambert and A. Delchambre, "Parameters ruling capillary forces at the submillimetric scale," *Langmuir*, vol. 21, no. 21, pp. 9537–9543, 2005.
- [29] L. Yang, Y. Tu, and H. Fang, "Modeling the rupture of a capillary liquid bridge between a sphere and plane," *Soft Matter*, vol. 6, no. 24, pp. 6178–6182, 2010.
- [30] R. van Oorschot, H. H. P. Garza, R. J. Derks, U. Staufer, and M. K. Ghatkesar, "A microfluidic afm cantilever based dispensing and aspiration platform," *EPJ Techniques and Instrumentation*, vol. 2, no. 1, p. 1, 2015.
- [31] R. Digilov, "Kelvin equation for menisci of nanosize dimensions," *Langmuir*, vol. 16, no. 3, pp. 1424–1427, 2000.
- [32] W. Abtew and A. Melesse, "Vapor pressure calculation methods," in *Evaporation and Evapotranspiration*, pp. 53–62, Springer, 2013.
- [33] K. Birdi, D. Vu, and A. Winter, "A study of the evaporation rates of small water drops placed on a solid surface," *The Journal of physical chemistry*, vol. 93, no. 9, pp. 3702–3703, 1989.
- [34] F. Peiti, "System identification [m]," 1999.
- [35] O. Montiel, R. Sepulveda, P. Melin, O. Castillo, M. A. Porta, and I. M. Meza, "Performance of a simple tuned fuzzy controller and a pid controller on a dc motor," in *Foundations of Computational Intelligence, 2007. FOCI 2007. IEEE Symposium on*, pp. 531–537, IEEE, 2007.
- [36] P. Cominos and N. Munro, "Pid controllers: recent tuning methods and design to specification," *IEE Proceedings-Control Theory and Applications*, vol. 149, no. 1, pp. 46–53, 2002.
- [37] P. Lanusse, J. Sabatier, and A. Oustaloup, "fractional order pid and first generation crone control system design," in *Fractional Order Differentiation and Robust Control Design*, pp. 63–105, Springer, 2015.
- [38] R. W. Brockett *et al.*, "Asymptotic stability and feedback stabilization," *Differential geometric control theory*, vol. 27, no. 1, pp. 181–191, 1983.
- [39] V. Hanta and A. Prochazka, "Rational approximation of time delay," *Institute of Chemical Technology in Prague. Department of computing and control engineering. Technická*, vol. 5, no. 166, p. 28, 2009.
- [40] H. K. Khalil and J. Grizzle, *Nonlinear systems*, vol. 3. Prentice hall New Jersey, 1996.
- [41] D. A. Bristow, M. Tharayil, and A. G. Alleyne, "A survey of iterative learning control," *IEEE Control Systems*, vol. 26, no. 3, pp. 96–114, 2006.
- [42] D. Wang, Y. Ye, and B. Zhang, *Practical Iterative Learning Control with Frequency Domain Design and Sampled Data Implementation*. Springer, 2014.
- [43] R. C. Smith, *Adaptive Control Tutorial*. Society for Industrial and Applied Mathematics, 2006.

